INFORMATION TO USERS

This manuscript has been reproduced from the microfilm master. UMI films the text directly from the original or copy submitted. Thus, some thesis and dissertation copies are in typewriter face, while others may be from any type of computer printer.

The quality of this reproduction is dependent upon the quality of the copy submitted. Broken or indistinct print, colored or poor quality illustrations and photographs, print bleedthrough, substandard margins, and improper alignment can adversely affect reproduction.

In the unlikely event that the author did not send UMI a complete manuscript and there are missing pages, these will be noted. Also, if unauthorized copyright material had to be removed, a note will indicate the deletion.

Oversize materials (e.g., maps, drawings, charts) are reproduced by sectioning the original, beginning at the upper left-hand corner and continuing from left to right in equal sections with small overlaps.

Photographs included in the original manuscript have been reproduced xerographically in this copy. Higher quality 6" x 9" black and white photographic prints are available for any photographs or illustrations appearing in this copy for an additional charge. Contact UMI directly to order.

Bell & Howell Information and Learning
300 North Zeeb Road, Ann Arbor, MI 48106-1346 USA
800-521-0600

NUMERICAL ANALYSIS AND APPLICATION OF FERROMAGNETIC MATERIALS FOR MICROSTRIP ANTENNA APPLICATIONS

by

Arik Darnell Brown

A dissertation submitted in partial fulfillment
of the requirements for the degree of
Doctor of Philosophy
(Electrical Engineering)
in The University of Michigan
2000

Doctoral Committee:

Professor John L. Volakis, Chairperson
Professor Anthony W. England
Assistant Professor Leo C. Kempel, Michigan State University
Professor Noboru Kikuchi

UMI Number: 9990852

Bell & Howell Information and Learning Company
300 North Zeeb Road
P.O. Box 1346
Ann Arbor, MI 48106-1346

I will praise thee with my whole heart: before the gods will I sing praise unto thee.

In the day when I cried thou answeredst me, and strengthenedst me with strength in my soul.

All the kings of the earth shall praise thee, O Lord, when they hear the words of thy mouth.

Yea, they shall sing in the ways of the Lord: for great is the glory of the Lord.

Though the Lord be high, yet hath he respect unto the lowly: but the proud he knoweth afar off.

Though I walk in the midst of trouble, thou wilt revive me: thou shalt stretch forth thine hand against the wrath of mine enemies, and thy right hand shall save me.

The Lord will perfect that which concerneth me: thy mercy, O Lord, endureth for ever: forsake not the works of thine own hands.

-Psalms 138

I dedicate this thesis to the love of my life, Nadine Simone Stuart, to the earthly sources of my strength and inspiration, my parents Rudy and Meredith Dorothea Brown, and to the loving memories of my grandmother Lillie Bell Brown and my godmother Ruth Cole.

ACKNOWLEDGEMENTS

I would first like to give all praise and honor to the almighty God. Without my heavenly Father I would never have been able to complete this dissertation. Through all the tough times and the late nights the Lord was always with me.

I would like to thank Dr. Anthony W. England and Dr. Noboru Kikuchi for participating on my thesis committee. I also want to recognize Dr. Leo C. Kempel for his continued support while as a sponsor for my research and as my committee member. Dr. Kempel is a wonderful person whose keen insight was always helpful. I especially would like to recognize my committee chairperson and research advisor Dr. John L. Volakis for his support during my tenure here at the University of Michigan. I learned a great deal from him and many of his suggestions proved invaluable for my thesis.

I would also like to thank the school of Rackham for my financial support as a Rackham Masters and Ph.D. fellow. Mr. Roger Doster also deserves a great deal of praise. His help in procuring me additional terms of funding was a tremendous blessing. In addition, I would like to thank the Graduate Engineering Minority Consortium (GEM), Xerox, and GTE for their financial support.

While at the University of Michigan, I had the good fortune of meeting my soul mate, Ms. Nadine S. Stuart. You are the only person who can truly understand the emotional turmoil I went through while obtaining my Ph.D. You have supported me throughout all the ups and downs encountered on the roller coaster ride of my doctoral process. You are and will always be my best friend, and I cannot thank you enough for all that you've done for me. I love you with all my heart and I look

forward to our many years of happiness together.

Perhaps no one deserves more praise than my forever-supportive parents Mr. and Mrs. Rudy and Meredith D. Brown. Without their sacrifice I would never have been in a position to obtain my doctoral degree. They are the epitome of nurturing and caring parents. To my father who is one of my closest friends and fraternity brother. I want to thank you for always making me feel like I could achieve anything I put my mind to. You believed in me before I believed in myself and for that I will be forever grateful. To my mother, who is also one of my closest friends. I thank you for being there for a young black man trying to make his way in the world. The times when you simply just listened to me have helped me so much. I could never ask for a better mother.

In addition to my parents, I have to thank my grandparents Mr. and Mrs. James and Ethel Mae Gibby, Sr. Your support over the years has been nothing short of remarkable. You two will always be near and dear to my heart. From little league games to care packages during my undergraduate years at the Massachusetts Institute of Technology you have always 'looked out' for me.

Special thanks are also in order for my paternal grandfather Mr. Wesley Brown, Sr. whose company I always enjoy, my aunt Ms. Deborah English who has always supported my academic and personal endeavors, and my paternal grandmother Mrs. Lillie Bell Brown and my godmother Mrs. Ruth Cole who have both gone to be with the Lord. I know you are both in heaven smiling with pride and joy in your hearts. I will never forget you. I also must thank the Stuart family: Mr. and Mrs. Raymond and Kathleen Stuart, Mr. and Mrs. Michael and Angela Stuart, and my main little man Master Trevor M. Stuart. Your support, prayers, and encouragement were definitely appreciated and will not be forgotten.

During my academic pursuits I have had the pleasure of befriending two very dynamic women who are near and dear to my heart Dr. Rashaunda M. Henderson

and Dr. Valarie D. Foster. Rashaunda you are the big sister I never had. If it had not been for you, I would have left Michigan with my Master's degree and not reaped the awards of the Ph.D. Although it was God working through you, I am still indebted to you. You are my dear friend and I can't imagine life without your friendship. Valarie, you have always been dear to my heart also. I will never forget the late nights we would spend in your office conversing over topics from Fourier series boundary-value problems to general life issues. You are truly one of the brightest people I've come across in my now 28 years of existence, and I thank you simply for being my friend.

I would also like to acknowledge Dr. Tyrone E. Benson and Dr. Rodney A. Bryant. They are two men who took me under their wing as a little brother. You both have been excellent role models, and I am blessed to have had the pleasure of befriending you both.

I have met many wonderful people while at Michigan and unfortunately I can't list everyone. I would though like to recognize Mr. John M. Baker, Mr. Alranzo B. Ruffin, Mr. Morris White, Mr. Nigel K. Hyatt, R. Kerry Bowie, Mr. Charles E. Hoffler III, Mrs. Yakeitha D. Fitch, Dr. Stephanie P. Bush-Goddard and Ms. Monique L. Glover. You all in your own special way made my Michigan experience unique and enjoyable.

I also would like to recognize some of my Radiation Laboratory colleagues, Mr. Stephané R. Legault, Mr. Mark D. Casciato, Mr. Michael W. Nurnberger, Mr. Dejan S. Filipovic, Dr. Sunil S. Bindiganavale, Dr. Youssry Y. Botros, Dr. Jian Gong, Dr. Katherine J. Muldavin, Dr. Lars S. Anderson and Mr. Johnathan D. Shumpert who have all assisted me and made my graduate student experience more enjoyable. I wish you all the best in your future pursuits.

Finally, I would like to recognize the distinguished brothers of the Sigma Chapter of Kappa Alpha Psi Fraternity Inc. The bond I share with these men is truly remarkable and I am proud to be a part of such a noble organization. I especially want

to thank my line brothers of Krimson Tide for adding spice to my extracurricular life while at Michigan. You definitely made my graduate experience truly unique.

TABLE OF CONTENTS

LIST OF FIGURES

LIST OF TABLES

LIST OF APPENDICES

Appendix

CHAPTER I

INTRODUCTION

This chapter gives the motivation of the work, summarizes the key contributions and provides the organization of the chapters to follow.

1.1 Motivation

The theory and method of operation of ferromagnetic materials has been known for many years. Quantitative studies were conducted, as early as 1910, on the use of ferrites for reducing eddy current losses in inductors and transformers [14]. However, microwave ferrite devices did not appear until 1949, and only after several more years of research were they reliable enough for electromagnetic applications [14]. Since then, a great deal of work has been done on characterizing the modes that exist within ferrite materials [16, 17, 23, 40, 45, 63, 73, 76, 77, 81], and how these modes can be effectively used for electromagnetic applications [34, 35, 36, 44, 85].

Initially, ferrites were used primarily for microwave circuit devices. Certain features make these materials attractive for microwave circuit applications [1]. One of these features is directly related to the ferrite permeability which has a tensor form. The components of this tensor can be controlled by a direct current (DC) magnetic bias field (H_o) [58], and this property is of particular interest to antenna

and microwave component applications. An example of this property was demonstrated by Fay, in which ferrites were used as microwave switches [22]. For this application, the switch is turned on and off by changing the applied bias field. In addition to their use in switching applications, ferrites have also been used as phase shifters [8, 12, 21, 26, 27, 28, 30, 31, 38, 47, 51, 61, 65, 68, 69, 74, 79, 87].

Ferrite materials are inherently anisotropic and exhibit nonreciprocal behavior. This nonreciprocal characteristic creates an edge-guided mode that exists for stripline and microwave devices utilizing ferrite substrates [7, 28]. Naito and Yamanaka verified that this mode also exists for ferrite coplanar waveguides [48]. Because of their nonreciprocal behavior, ferrites have been used in many microwave components such as circulators and isolators [2, 27, 28, 58].

The successful application of ferromagnetic materials in the area of microwave circuits led to their application to antennas as well. Ferrites have been used to control the radiation properties of antennas, in particular, microstrip patch antennas residing on ferromagnetic substrates. Ferrite materials tend to have high effective permittivities, thus allowing for smaller antenna sizes at lower frequencies. Das has shown that this miniaturization produces antennas with better bandwidth and efficiency than antennas on dielectrics [18, 19].

Ferrites enhance antenna performance in their unbiased state, but have a greater impact on antenna characteristics when a DC bias field is applied to the ferrite material. The interaction between the DC and radio frequency (RF) fields greatly improves antenna functionality. By changing H_o, it is possible for the patch to radiate at more than one frequency. Because normal patch antennas demonstrate narrow bandwidth, this feature of the ferrite patch antenna is advantageous because it increases functionality. Specifically, it has been shown experimentally that a 40% tuning range is achievable [59]. Several other examples in the literature also demonstrate this unique feature both experimentally and theoretically [41, 42, 46, 55, 71, 86].

In addition to frequency control, ferrite antennas are also capable of radar cross section (RCS) reduction. By varying H_o, it is possible to reduce the RCS at desired frequencies [84]. It has been shown theoretically by Pozar, that for values of $\mu_{eff} < 0$ it is possible to reduce the RCS at resonant frequencies for a ferrite substrate by 20 - 40 dB [56, 57]. When the antenna is 'switched' into an off state, at a certain frequency range, the RCS is drastically reduced [54]. The same phenomenon can be achieved by placing a thin ferrite layer over a patch on a dielectric [82]. Thus, by changing H_o, the antenna can be switched between both an 'on' and 'off' state.

Another advantage of ferrite patch antennas, is that circular polarization can be achieved over a large bandwidth. Using either a circular patch [62, 71], or a rectangular patch [56, 60], circular polarization is achievable over a wide range of frequencies using a single probe feed. To obtain either left hand circular polarization (LHCP) or right hand circular polarization (RHCP) it is necessary to only reverse the polarity of the bias field.

Perhaps the most attractive property of ferrite antennas is their beam scanning capability in antenna applications. Scanning using single element antennas was initially accomplished using ferrites as phase shifters. Stern *et. al* demonstrated a scan angle of 15° using this approach [67]. The actual antenna used by Stern *et. al* used a dielectric material and the ferrite was not part of the actual antenna. Maheri *et. al.* though, designed a leaky-wave antenna which was built on top of a ferrite substrate [43] and a maximum scan angle of 40° was observed. Yang and Castaneda then analytically investigated beam scanning using a microstrip patch on a ferrite substrate [84].

Ferrites are most attractive for antenna array applications. Similar to RCS control, by changing H_o, the scan angle of the array can be changed. This is more desirable than mechanically steering the array where damage and repair-ability can become problematic factors [25]. Experimental studies have been performed [49],

demonstrating the effectiveness of ferrites for antenna arrays. The steering properties of ferrite arrays has been verified theoretically as well [32, 83].

In conclusion, ferromagnetic materials have a wide array of uses in electromagnetic applications. Their frequency agility and anisotropic nature make them attractive choices for microwave circuits and antennas, specifically microstrip antennas. The goals of this thesis are to show the effectiveness of using the Finite Element Method (FEM) to model ferrite microstrip antennas, and to provide practical insight on numerical and experimental issues when designing and analyzing these radiating structures.

1.2 Purpose

Analysis of ferrite microstrip antennas has primarily been accomplished using the Moment Method (MoM) [56, 86], with the exception of Kokotoff [41] and Polycarpou [52, 53]. Although the MoM is a rigorous full-wave solution approach, it is incapable of handling inhomogeneous materials. In comparison, the FEM easily handles material inhomogeneities. Kokotoff has also shown experimentally that, in certain instances, the internal DC magnetic field within the ferrite substrate is nonuniform [41]. Thus, for applications where this situation arises, the FEM would be a viable numerical approach. For a portion of this thesis, it is assumed that the ferrite substrate size, in relation to the biasing structure, is small resulting in a uniform magnetic field throughout the ferrite. However, nonuniform magnetic bias fields occur due to the inherent field structure associated with the permanent magnets used for biasing. Simulations and measurements are carried out to demonstrate effects associated with a nonuniform field bias.

A related issue which is of more practical interest, is a substrate composed of both ferrite and dielectric regions. This inhomogeneous situation arises when using

a ferrite microstrip feed line for an antenna/array. Using the FEM, it is possible to determine optimum applied bias field values for beam steering. In order to determine these optimum values, an analysis of the field propagation within the ferrite microstrip substrate must be performed. Yang has numerically studied field propagation, for a open-ended microstrip line on a ferrite substrate [80], while Batchelor and Langley experimentally demonstrated beam steering for 2 x 1 array of circular patches with ferrite microstrip feed lines [5]. However, no numerical work has been done for beam steering of antennas/arrays on dielectric substrate using ferrite microstrip feed lines.

In this dissertation, the FEM is used to model ferrite patch antennas. A method for overcoming numerical difficulties encountered using the FEM is shown. Also, an approach is given for determining optimum biasing magnetic field values for beam steering. Numerical and experimental data are shown which validate this approach. Lastly, temperature effects are taken into consideration when modeling ferrite microstrip antennas.

1.3 Dissertation Organization

Chapter 2 briefly describes the mathematical formulation for modeling a ferromagnetic material placed in a DC magnetic bias field. In addition, background information on using the FEM for electromagnetic applications is provided.

Chapter 3 contains RCS and input impedance validations for ferrite multi-layer open cavities and a rectangular microstrip patch on a ferrite substrate. Excellent agreement is shown using the FEM. Propagation modes possible for ferrites are also introduced in addition to their effects on the numerical calculations. It is discovered that a certain mode can predict regions of poor convergence for iterative solvers. A Generalized Minimal Residual (GMRES) iterative solver is shown to overcome the

frequency regions of poor convergence. This chapter concludes with a brief analysis of the effects of a nonuniform bias field on the radiation characteristics of a ferrite antenna.

In Chapter 4, a coplanar waveguide (CPW), which was built and measured, was used to determine the propagation constant (β) of a ferrite rectangular substrate. This chapter is intimately related to Chapter 5, because the experimental values for the ferrite material are compared to numerical data computed using the FEM. The comparisons serve to justify the FEM for the analysis conducted in Chapter 5.

This chapter also contains a static analysis of the internal DC magnetic field of a rectangular ferrite substrate, biased by permanent magnets. These magnets do not necessarily generate a uniform magnetic field bias as was assumed. The bias field was actually nonuniform, and fringing effects degraded the quality of the measurements. A static analysis provided the correct bias field distribution to be used in the FEM model, and to better simulate the actual measurement set-up.

Chapter 5 investigates microstrip ferrite phase shifters for antenna array beam steering. A method is shown which determines optimum bias field values for beam scanning. The method is based on a numerical study of the transverse mode (introduced in Chapter 3) propagation constant in the ferrite substrate. Specific magnetic field values, corresponding to a value of the propagation constant, produce optimal steering, and these are identified in the chapter.

Chapter 6 emphasizes the importance of practical considerations when using ferrite microstrip antennas. The effects of temperature on the antenna performance are demonstrated in this chapter. The increased temperature in the ferrite material causes the magnetization of the material to decrease, thus affecting the performance of the antenna.

Chapter 7 concludes with a summary of the salient points contained in each chapter. Ideas for future work in this area are also presented.

CHAPTER II

BACKGROUND

This chapter presents basic concepts for applying the FEM to ferromagnetic materials.

2.1 Ferromagnetic Material Overview

The anisotropy of a ferromagnetic material is caused by the interaction between an applied DC bias field and an RF signal. Application of the DC field causes the magnetic moments in the material to align themselves with the DC field producing a net magnetization. Depending on the polarization of the RF field, a microwave signal will propagate through a ferrite medium differently depending on the direction [58]. Thus, a tensor is needed to characterize the ferrite medium.

Figure 2.1 shows a spinning electron in the presence of a z directed DC magnetic field. The field exerts a torque on the magnetic moment ($\mathbf{m}$) of the electron, and forces the electron to precess about the magnetic field. From a macroscopic viewpoint there are N moments in the ferrite material which leads to a net magnetization

$$\mathbf{M} = N\mathbf{m}. \tag{2.1}$$

The equation of motion for the net magnetization $\mathbf{M}$ is

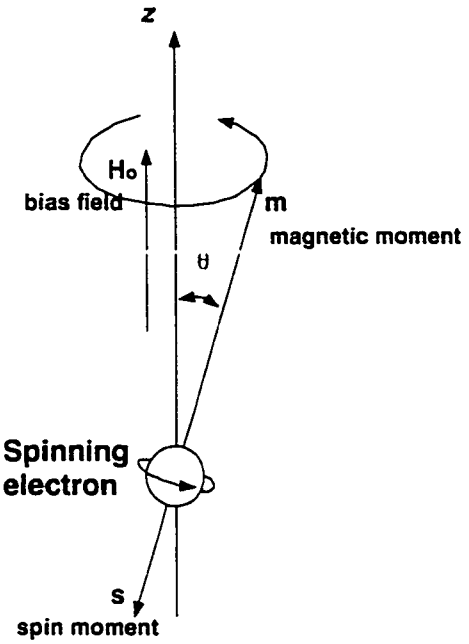

Figure 2.1: Spinning electron in the presence of a DC bias field (H_o).

$$\frac{d\mathbf{M}}{dt} = -\mu_o \gamma \mathbf{M} \times \mathbf{H} \tag{2.2}$$

where $\mathbf{H}$ is the external bias field, and γ is the gyromagnetic ratio which is the ratio of the spin magnetic moment to the spin angular momentum [58]. As the strength of $\mathbf{H}$ is increased, $\mathbf{M}$ increases until it reaches a saturation limit. This upper bound on $\mathbf{M}$ is referred to as the saturation magnetization, $\mathbf{M_s}$. In this dissertation, the ferrite materials are assumed to be in saturation.

To model the interaction effects due to a microwave signal, an alternating current (AC) field ($\mathbf{h}$) is added to $\mathbf{H}$ so that the total field ($\mathbf{H_t}$) becomes

$$\mathbf{H_t} = \mathbf{H} + \mathbf{h}. \tag{2.3}$$

This leads to a total magnetization of the form,

$$\mathbf{M_t} = \mathbf{M_s} + \mathbf{m} \tag{2.4}$$

where **m** is the AC magnetization produced by **h**.

If the AC fields possess an $e^{j\omega t}$ time dependence, (2.3) and (2.4) can be substituted into (2.2), and after a few algebraic manipulations the following linear relationship between **m** and **h** is obtained (assuming a z-directed bias).

$$\mathbf{m} = [\chi]\mathbf{h} = \begin{bmatrix} \chi_{xx} & \chi_{xy} & 0 \\ \chi_{yx} & \chi_{yy} & 0 \\ 0 & 0 & 0 \end{bmatrix} \mathbf{h}. \tag{2.5}$$

The elements of $[\chi]$ are given by [58]

$$\chi_{xx} = \chi_{yy} = \frac{\omega_o \omega_m}{\omega_o^2 - \omega^2} \tag{2.6}$$

and

$$\chi_{xy} = -\chi_{yx} = \frac{-\omega\omega_m}{\omega_o^2 - \omega^2}. \tag{2.7}$$

with

$$\omega_o = \gamma \mu_o H \tag{2.8}$$

and

$$\omega_m = \gamma \mu_o M_s. \tag{2.9}$$

In (2.8), ω_o is the Larmor precession frequency, and is the frequency at which the electron precesses about **H** [58]. The time varying magnetic flux density, **B**, can then be written as

$$\mathbf{B} = [\mu]\mathbf{h} = \begin{bmatrix} \mu & j\kappa & 0 \\ -j\kappa & \mu & 0 \\ 0 & 0 & \mu_o \end{bmatrix} \mathbf{h} \tag{2.10}$$

where the elements of $[\mu]$ are [58]

$$\mu = \mu_o(1 + \chi_{xx}) \tag{2.11}$$

$$\kappa = -j\mu_o\chi_{xy}. \tag{2.12}$$

For an arbitrary bias, the procedure is the same, only the expression for $[\mu]$ becomes more complex. The general expression for an arbitrary bias can be written as

$$\mathbf{H} = H_{o_x}\sin\theta\cos\phi\,\hat{\mathbf{x}} + H_{o_y}\sin\theta\sin\phi\,\hat{\mathbf{y}} + H_{o_z}\cos\theta\,\hat{\mathbf{z}} \tag{2.13}$$

Following the steps outlined in the preceding paragraph, substitution of (2.13) into (2.3), leads to the most general form for the susceptibility and permeability tensors.

Throughout section 2.1, MKS units have been used. In practice, values for the saturation magnetization and applied bias field are displayed in the CGS unit system. For the remainder of the thesis, this is the unit system of choice. Thus, the saturation magnetization and magnetic field strengths can be converted using the following relations, $\mu_o\gamma M_s[\frac{W}{m^2}] = 10^{-4}(4\pi M_s)[G]$ and $\mu_o\gamma H_o[\frac{W}{m^2}] = 10^{-4}(H)[Oe]$.

2.2 FEM Overview

In electromagnetics, the FEM is used to solve for scalar or vector unknowns, such as electric and magnetic fields. The FEM is used to discretize the region governing the domain of the problem which is characterized by a differential equation. In this thesis, the computational domain is a PEC cavity housing the microstrip patch and/or microstrip line residing on the cavity aperture. The fundamental equations governing the fields in the cavity are:

$$\nabla \times \mathbf{E} = -j\omega\mathbf{B} - \mathbf{M} \tag{2.14}$$

$$\nabla \times \mathbf{H} = j\omega\mathbf{D} + \mathbf{J} \tag{2.15}$$

where $\mathbf{E}$ and $\mathbf{H}$ are the electric and magnetic field intensities, $\mathbf{D}$ and $\mathbf{B}$ are the electric and magnetic flux densities. $\mathbf{M}$ is the impressed magnetic current density, and $\mathbf{J}$ is the electric current density, composed of both impressed and conductor current densities ($\mathbf{J} = \mathbf{J_i} + \mathbf{J_c}$) [4]. The form of (2.14) and (2.15) assumes an $e^{j\omega t}$ time dependence. Using (2.14) and(2.15), the differential equation obeyed, by the electric field, is the well known wave equation for the electric field intensity.

$$\nabla \times \overline{\overline{\mu_r}}^{-1} \nabla \times \mathbf{E} - k_o^2 \, \overline{\overline{\epsilon_r}} \cdot \mathbf{E} = -j\omega\mu_o \, \mathbf{J} - \nabla \times \overline{\overline{\mu_r}}^{-1} \cdot \mathbf{M}. \tag{2.16}$$

A similar equation can be derived for $\mathbf{H}$, but is not included since an electric field formulation is used throughout the thesis. In (2.16), the medium is assumed to be anisotropic meaning

$$\mathbf{D} = \epsilon_o \overline{\overline{\epsilon_r}} \cdot \mathbf{E} \tag{2.17}$$

and

$$\mathbf{B} = \mu_o \overline{\overline{\mu_r}} \cdot \mathbf{H} \tag{2.18}$$

where $\overline{\overline{\epsilon_r}}$ and $\overline{\overline{\mu_r}}$ are rank 3 tensors. In this dissertation, the permittivity is assumed to be isotropic, and only the permeability is modeled as anisotropic.

To obtain the unknown field, in the context of the FEM, the variational equation

$$\delta F(\mathbf{E}) = \mathbf{0} \tag{2.19}$$

is solved [75], where

$$\begin{aligned} F(\mathbf{E}) &= \frac{1}{2}\int\int\int_V [\frac{1}{\mu_r}(\nabla \times \mathbf{E}) \cdot (\nabla \times \mathbf{E}) - k_o^2 \epsilon_r \mathbf{E} \cdot \mathbf{E}]\mathbf{dV} \\ &+ \int\int\int_V [jk_o Z_o \mathbf{J^{int}} \cdot \mathbf{E} - \frac{1}{\mu_r}\mathbf{M^{int}} \cdot (\nabla \times \mathbf{E})]\mathbf{dV} \\ &+ jk_o Z_o \int\int_S (\mathbf{E} \times \mathbf{H}) \cdot \hat{\mathbf{z}}\mathbf{dS} \end{aligned} \tag{2.20}$$

In this equation, V denotes the cavity volume, S is the cavity aperture, ϵ_r and μ_r are the relative permittivity and permeability of the ferrite substrate, $\mathbf{J^{int}}$ and $\mathbf{M^{int}}$ are internal electric and magnetic sources due to the antenna feeds, and the last term in (2.20) is the BI term. Discretization of (2.20) using Galerkin's method leads to the linear system,

$$[A]\{E\} = \{b\} \tag{2.21}$$

where $[A]$ is an $N \times N$ matrix and $\{b\}$ is an $N \times 1$ column vector given by [39].

When modeling gyromagnetic substrates, the functional must be modified to incorporate the inherent anisotropy of the ferrite material. Specifically, for general anisotropic media, we have

$$\begin{aligned} F(\mathbf{E}) &= \frac{1}{2}\int\int\int_V [\overline{\overline{\mu_r}}^{-1} \cdot (\nabla \times \mathbf{E}) \cdot (\nabla \times \mathbf{E}) - k_o^2 \overline{\overline{\epsilon_r}} \cdot \mathbf{E} \cdot \mathbf{E}]\mathbf{dV} \\ &+ \int\int\int_V [jk_o Z_o \mathbf{J^{int}} \cdot \mathbf{E} - \overline{\overline{\mu_r}}^{-1} \cdot \mathbf{M^{int}} \cdot (\nabla \times \mathbf{E})]\mathbf{dV} \\ &+ jk_o Z_o \int\int_S (\mathbf{E} \times \mathbf{H}) \cdot \hat{\mathbf{z}}\mathbf{dS} \end{aligned} \tag{2.22}$$

where $\overline{\overline{\epsilon_r}}$ and $\overline{\overline{\mu_r}}$ are the relative permittivity and Polder permeability tensors. The element matrices in the FE assembly process, resulting from this functional, are given in Appendix A.

2.3 Summary

In this chapter, pertinent equations relating to the permeability tensor for a biased ferromagnetic material were shown. Also, a brief description of the FEM was given.

CHAPTER III

FERROMAGNETIC PATCH ANALYSIS

In this chapter, results are shown which demonstrate the FEM's capability to effectively model ferrite substrate antennas. Ferrite modes and their relation to the convergence properties of iterative solvers are also discussed. Finally, the effects of nonuniform bias fields on the radiation properties of microstrip ferrite antennas are shown. The work in this chapter was published in [11].

3.1 Introduction

Patch antennas on ferrite substrates are attractive because they offer greater agility in controlling the radiation characteristics of the antenna. Their inherent anisotropy and non-reciprocal properties [58], permit variable frequency tuning [35, 59, 60], and antenna polarization diversity [62]. External biasing of the ferrite substrate also allows for beam steering [13, 32, 43, 49], pattern shape control, and radar cross section control [25, 55] by forcing the ferrite into a cut-off state [57].

Measurements and analytical studies based on the Moment Method (MoM) have verified these attractive properties of ferrite substrates. Several papers have already considered the performance of ferrite patch antennas [42, 56, 82, 84]. These works employed the Moment Method (MoM) technique in conjunction with the substrate

Green's function. Validation of the results given in [56, 86] have so far been difficult to achieve. Also, MoM formulations do not permit modeling of nonuniform biasing and inhomogeneous constitutive parameters, a situation which inherently occurs when the ferrite is biased. To provide for greater flexibility in modeling the ferrite substrate and the substrate cavity (see Figure 3.1), an analysis of the ferrite patch was performed using the Finite Element-Boundary Integral (FE-BI) method. As usual, the substrate housed within the cavity is modeled by the FEM using an edge-based formulation [39, 75]. Consequently, multiple substrate (and superstrate) layers can be handled easily including lateral material inhomogeneities within each layer. In the formulation, the finite element (FE) mesh is truncated at the surface of the cavity using the rigorous BI method. Thus, the proposed FE-BI implementation is equally rigorous to the traditional MoM (employing the substrate Green's function) and allows modeling of finite and inhomogeneous substrates.

Because of their tensor properties, ferrites introduce a great deal of complexity into the formulation when solving radiation problems. When using the FE method, it is observed that the system matrix becomes asymmetric and can be poorly conditioned at certain values of the ferrite parameters. Initially, the Bi-Conjugate Gradient(BiCG) method was used for solving the matrix system. To improve performance, a preconditioned BiCG algorithm was also examined. However, the BiCG was not robust under certain bias conditions. In these cases, it was necessary to resort to the Generalized Minimal Residual (GMRES) method as described later.

In the following sections, a brief description of the formulation and it's implementation for ferrite materials is given. Next, some simple ferrite patch antenna calculations involving scattering and radiation examples are presented. These serve to validate the implementation and preciseness of the results. They also reveal that serious solution convergence difficulties can arise for certain bias states of the substrate. It is shown that these difficulties can be predicted *a priori*. For this implementation

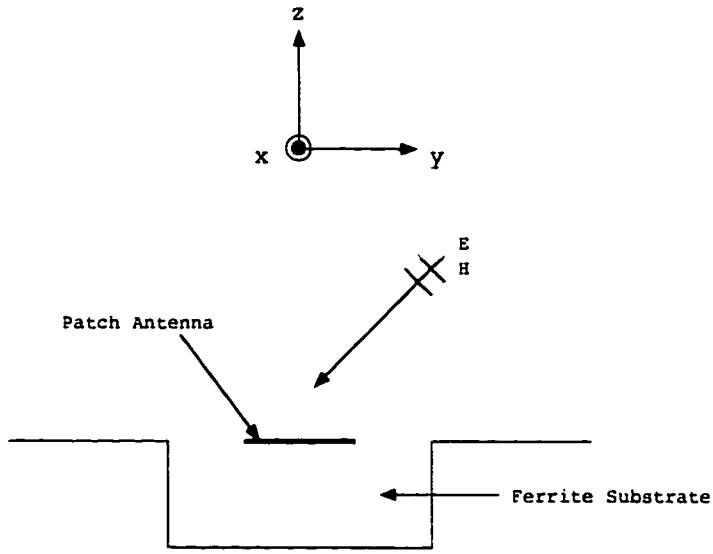

Figure 3.1: Geometry for a patch antenna on an anisotropic substrate.

it was necessary to employ a more robust iterative solver: one employing the GMRES method with preconditioning. Calculations showing the effects of biasing on the antenna resonance and scattering characteristics are given in the latter part of the chapter. The final example is a calculation simulating a nonuniform substrate (due to natural biasing). This example demonstrates the importance of modeling nonuniformities accurately for evaluating the performance of a radiating antenna.

3.2 Applications and Validation

3.2.1 Probe-Fed Patch Antenna

Consider the probe fed patch antenna geometry given in Figure 3.1. For this example the ferrite substrate parameters were $4\pi M_s = 650$ G, $H_o = 600$ Oe. and $\epsilon_r = 10$. The calculated input impedance and radiation pattern are given in Figures 3.2 and 3.3. As expected, biasing caused a shift in resonance and this is clearly seen in Figure 3.2. Specifically, the ferrite substrate decreased the lowest resonance of the patch from 4.44 GHz to 2.24 GHz, thus reducing the overall size of the patch for

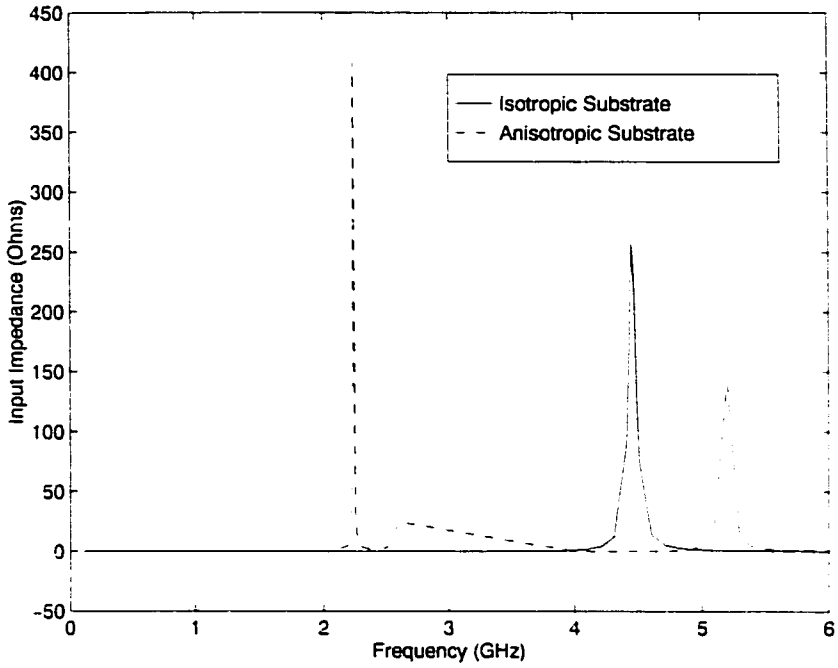

Figure 3.2: Real input impedance for an x-biased patch, with a 2.2 GHz frequency shift in the first resonance of the patch.

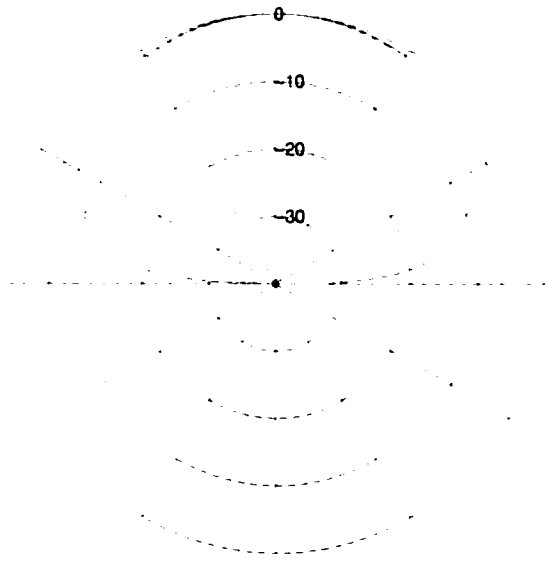

Figure 3.3: Radiation pattern in the yz plane on an x-biased ferrite substrate (Frequency = 2.2 GHz, – Isotropic Substrate, - - Anisotropic Substrate).

operation at the same frequency. From Figure 3.3, it is observed that the biased patch exhibits a null along the horizontal direction. This patch was also considered by Schuster and Luebbers [66] using the Finite Difference Time Domain (FDTD) method. The computed resonance shift was within 40 MHz of their values (1.8%). Although this type of agreement is considered very good for patch antennas, the small difference may be attributed to possible numerical implementation inaccuracies. The simulation used a cavity size of 4.085 cm × 4.085 cm × .015 cm and the FE-BI system consisted of 3766 unknowns.

3.2.2 Ferrite Filled Cavity

Biased Substrate

Consider a cavity with several magnetized layers as shown in Figure 3.4. Layers 2 and 4 are magnetized in the $\hat{y}$ direction, e.g.

$$\bar{\bar{\mu}}_r = \begin{pmatrix} \mu & 0 & -j\kappa \\ 0 & \mu_o & 0 \\ j\kappa & 0 & \mu \end{pmatrix} \tag{3.1}$$

This is a particular example considered by Kokotoff [41]. The RCS of the layered ferrite cavity for different biasing values (H_o) is given in Figure 3.5, and the calculations are seen to be in agreement to those of Kokotoff [41] for all cases.

This example again demonstrates the frequency shifting property of ferrite materials with biasing and validates the employed FEM formulation. The number of unknowns for this example was 6,776 (BI unknowns = 420).

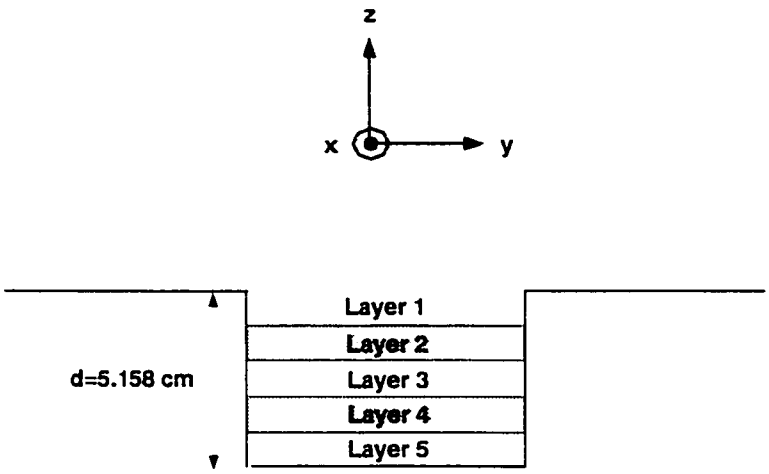

Layer1 d = 0.726 cm, ε_r = 2.2, μ_r = 1.0

Layer2 d = 1.790 cm, ε_r = 13.9, $4\pi M_s$=800G, ΔH=5Oe

Layer3 d = 0.737 cm, ε_r = 2.2, μ_r = 1.0

Layer4 d = 0.762 cm, ε_r = 13.9, $4\pi M_s$=800G, ΔH=5 Oe

Layer5 d = 1.143 cm, ε_r = 1.0, μ_r = 1.0

Figure 3.4: Geometry of a cavity with ferrite layers.

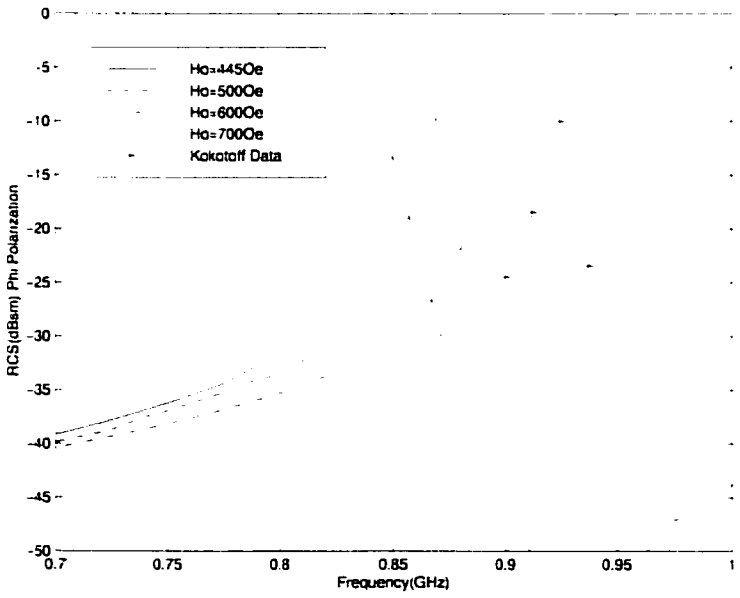

Figure 3.5: Effect of biasing on the RCS of the cavity in Figure 3.4. All computations were carried out using the FE-BI method except as noted.

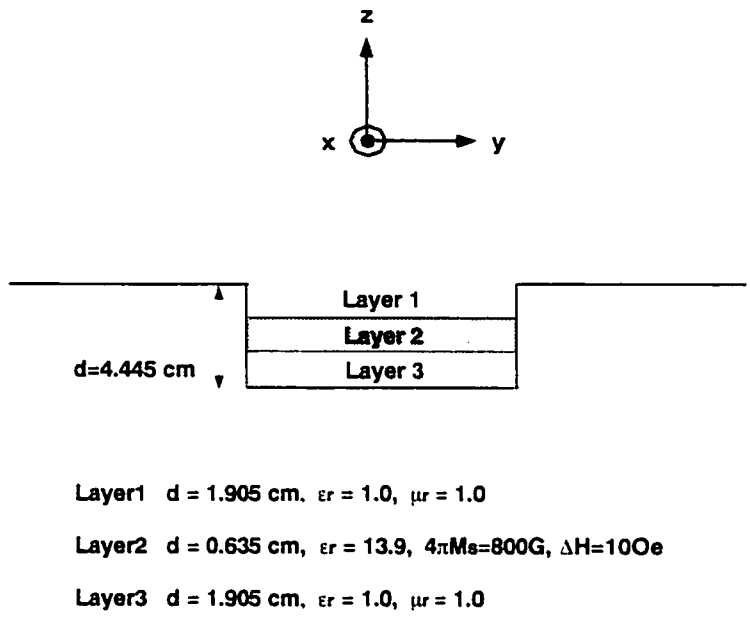

Figure 3.6: Ferrite cavity geometry.

Unbiased Substrate

Next a 3 layer cavity was analyzed which consisted of a ferrite layer between two free space layers. The ferrite layer is magnetized with parameters $\epsilon_r = 13.9$ and $4\pi M_s = 800$ G. However, no biasing is applied. As shown in Figure 3.7, calculations using the BiCG solver, for $4\pi M_s = 0$, were in complete agreement with results given in [41]. Figure 3.8 shows results for the same geometry with the ferrite layer magnetized. About 780 unknowns (BI unknowns $\simeq$ 180) were used to simulate this cavity. However, this example presented convergence difficulties when the BiCG solver was used. An investigation of several other cases demonstrated that, in general, convergence difficulties were encountered when the propagation constant, β, was zero. To better illustrate this, the convergence performance for the result shown in Figure 3.2 was plotted in Figure 3.9. Looking at Figure 3.10, it is apparent that the region of non-convergence extending from 2.5 GHz to 3.5 GHz corresponds directly to where β has a value of zero in Figure 3.10.

When dealing with ferrite materials, the field behavior is determined by the prop-

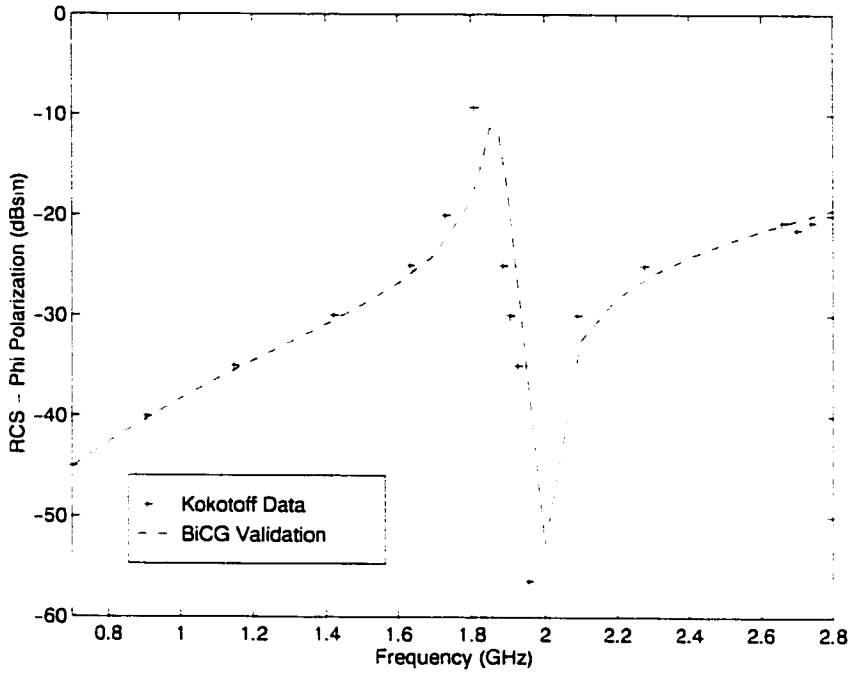

Figure 3.7: RCS (normal incidence), using the FE-BI, of the loaded cavity in Figure 3.6 with $M_s = 0$ (i.e. no magnetization).

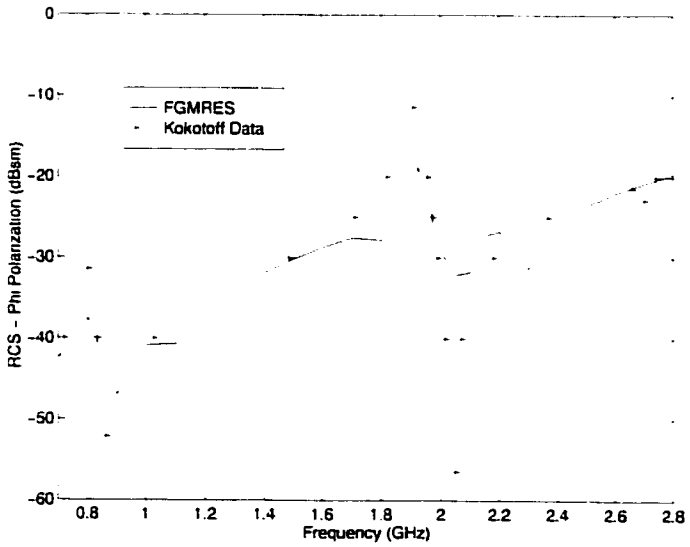

Figure 3.8: RCS(normal incidence), using the FE-BI, of the loaded cavity shown in Figure 3.6 with the values of M_s and ΔH as given there.

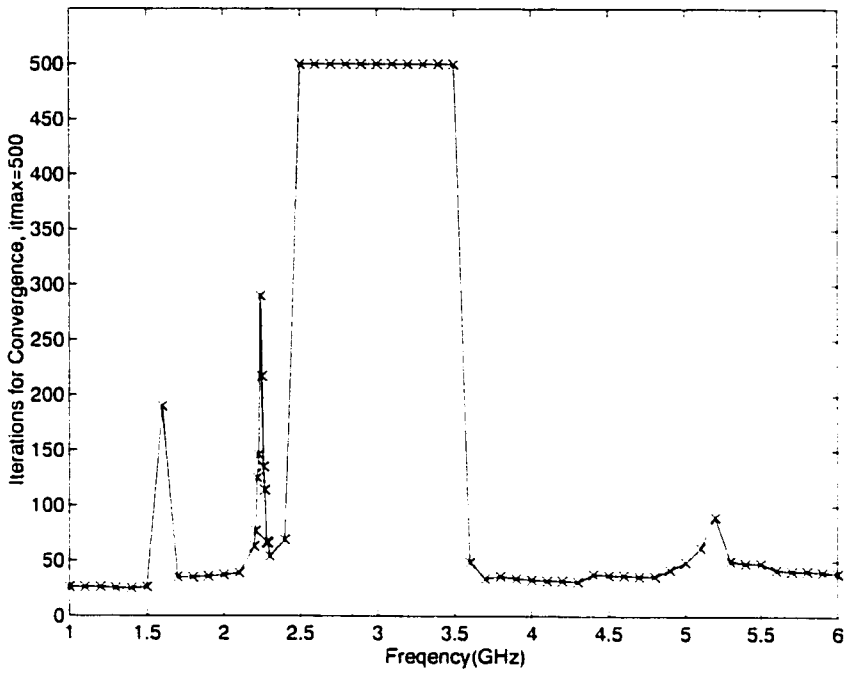

Figure 3.9: Plot of convergence performance for the simulation results shown in Figure 3.2

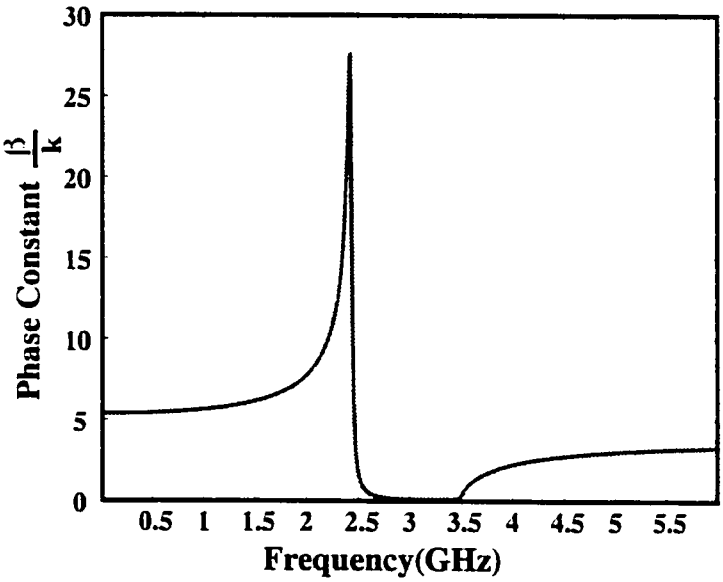

Figure 3.10: β plot, for the transverse mode, which corresponds to the areas of non-convergence in Figure 3.9

agation direction and its orientation with the applied magnetic bias field direction. There are two separate cases which determine the effective permeability(μ_{eff}) within the ferrite [34, 58] - the longitudinal case where propagation is parallel to the applied bias field and the transverse case where propagation is perpendicular to the applied bias field. In the longitudinal case

$$\mu_{eff} = \mu \pm \kappa \tag{3.2}$$

whereas in the transverse case

$$\mu_{eff} = \frac{\mu^2 - \kappa^2}{\mu} \tag{3.3}$$

For both propagation modes, the propagation constant within the ferrite is calculated as

$$\gamma = j\omega\sqrt{\epsilon_o\epsilon_r\mu_o\mu_{eff}} \tag{3.4}$$

$$= \alpha + j\beta \tag{3.5}$$

The modes due to the propagation constant play a major role in the FE solution.

For the previous example, β vanished for one of the longitudinal modes corresponding to $\mu_{eff} = \mu + \kappa$ and the transverse mode. The actual values of β for all three modes are given in Figure 3.11 and it is observed that for the aforementioned two modes, β vanishes from about 1 GHz to 2.5 GHz (see Figure 3.11). In concert, the BiCG solver failed to converge within this frequency range. Results based on a direct solver were also inaccurate due to the poor system condition. To overcome convergence difficulties for those frequencies where $\beta = 0$ for one or more of the modes, the preconditioned Flexible GMRES (FGMRES) [64] was used.

Features that make the FGMRES algorithm attractive are its guaranteed conver-

gence, ability to adapt variable preconditioners, and a predictable error history (i.e. a smooth and monotonic convergence pattern as compared to the erratic convergence pattern of the BiCG algorithm). An important parameter for the GMRES solver is the number of interior iterations(m) before restarting the solver. These initial iterations control the number of spanning basis vectors used for an initial approximation of the solution. For our examples, the minimum m used was 70 while the maximum m was 280. For frequencies where the system is ill-conditioned a higher value for m is required, along with preconditioning. From the analysis, these points occur near resonance, which is approximately 1.98 GHz (Figure 3.8).

Using the GMRES solver, with the Approximate Inverse Preconditioner(AIPC) [64], convergence was obtained at all points for the geometry in Figure 3.6. Figure 3.8 shows the results, and it is observed that the GMRES solution tracks the data in [41] quite well. However, given the poor condition of the system, it is not clear as to which of the curves in Figure 3.8 is not accurate. Both curves predict the RCS peak at 1.9 GHz except that the value of the peaks differ.

3.3 Nonuniform Biasing

When building a ferrite antenna, a permanent magnet is required to produce the applied magnetic bias field. Due to the finite nature of the magnet, the field is no longer uniform and thus the electrical material properties become inhomogeneous. Since many analysis methods assume a uniform bias field, this produces a solution which is no longer accurate. In contrast, the FEM allows for arbitrary specification of the material within the volume which is an inherent advantage of FEM over other numerical methods.

To observe the effect of nonuniform magnetization, consider modeling the measured bias field in a ferrite cavity as given in Figure 3.12 [41]. Indeed, Figure 3.12

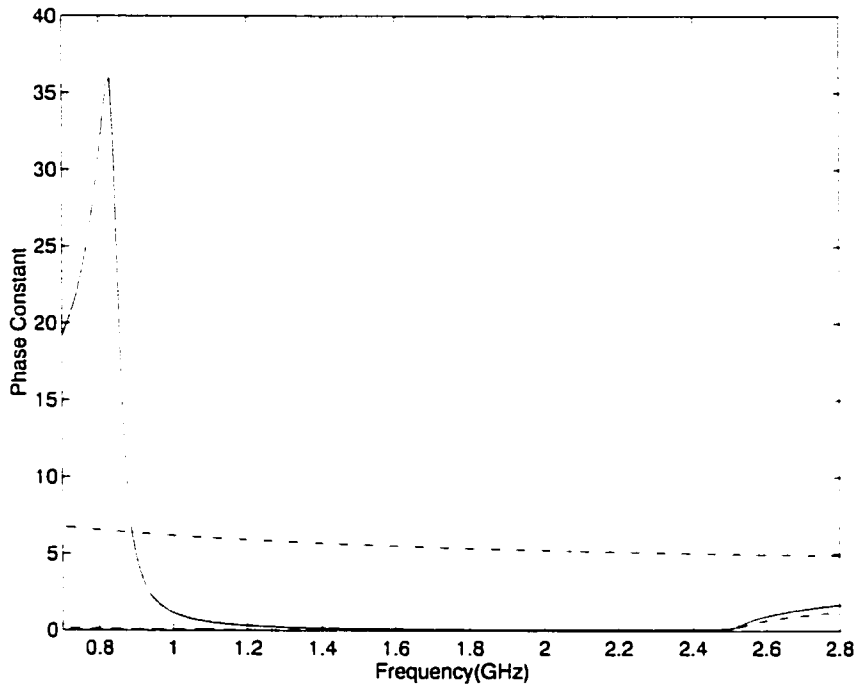

Figure 3.11: β Normalized to k_o. $-$ $\mu_{eff} = \frac{\mu^2-\kappa^2}{\mu}$. $--$ $\mu_{eff} = \mu+\kappa$. $-.$ $\mu_{eff} = \mu-\kappa$ for a ferrite medium having $4\pi M_s = 800$ G. $\Delta H = 10$ Oe. and $\epsilon_r = 13.9$.

reveals a difference of more than 1000 G at different locations within the cavity, showing the necessity of the FEM technique to handle this inhomogeneous behavior. RCS calculations for this nonuniform biasing are provided in Figure 3.13 for a 6 cm x 6 cm x 1 cm cavity filled with this material. It is clear, that the resonance of the cavity is substantially affected by the nonuniformity of the bias field. In Chapter 5, the actual nonuniformities of the bias field are computed using a DC analysis.

3.4 Summary

This chapter presents several results and validations demonstrating the attractive properties of ferrite patch antennas. The high dielectric constant of the ferrite, inherent magnetization, and external biasing all serve to minimize the size of the patch, in addition to providing pattern control and lower radar cross section over a given band. The employed hybrid FE-BI method also permitted an investigation on the effects of the typical nonuniform bias fields which occur across the substrate volume. These nonuniform bias fields cause inhomogeneities which affect the operation frequency and overall response of the antenna and may be a cause of discrepancies between measurements and calculations.

Also poor matrix conditioning and solution convergence difficulties may be traced to band regions where one or more ferrite modes are non-propagating. This situation prompted the use of a more robust iterative solvers, and, to achieve convergence, a preconditioned version of the GMRES method was used. GMRES proved effective in cases where the usual conjugate and biconjugate gradient algorithms failed.

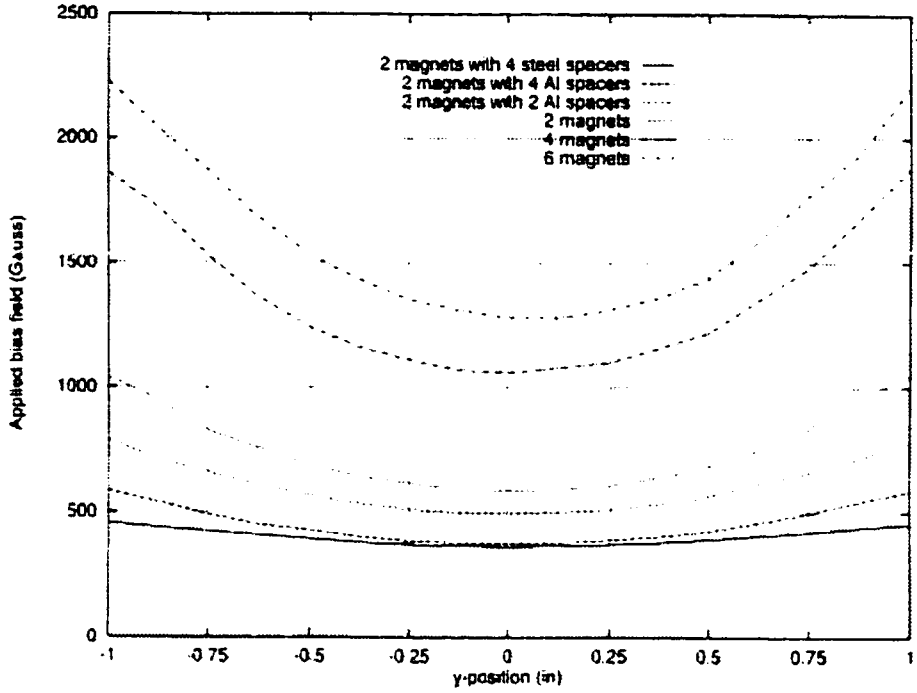

Figure 3.12: Measurement of the nonuniform magnetic field within a cavity [41].

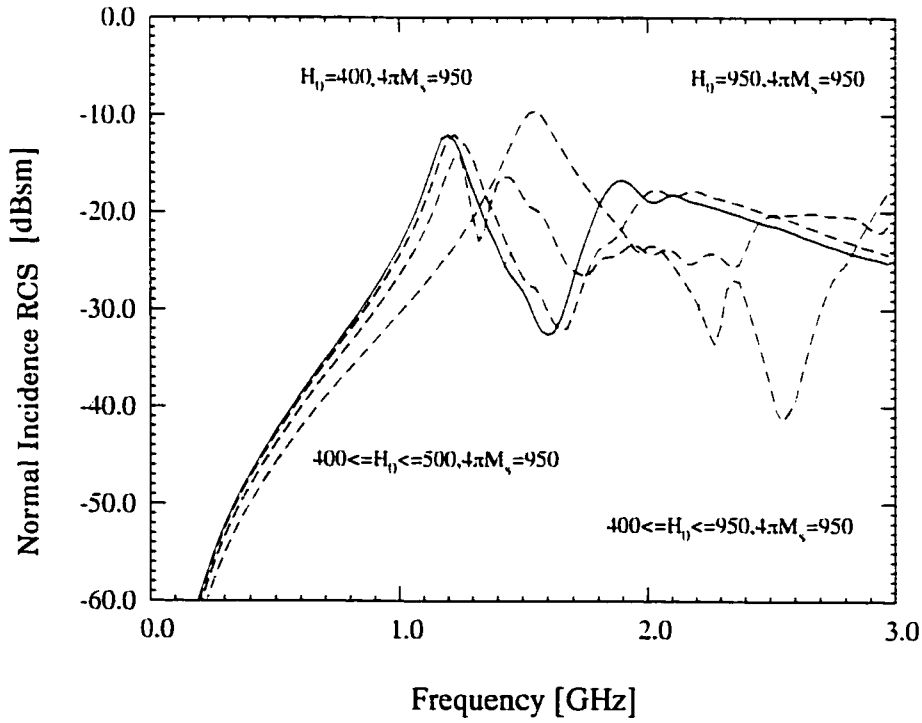

Figure 3.13: RCS due to a nonuniform magnetic field (see Figure 3.12) across a 6 cm x 6 cm x 1 cm cavity.

CHAPTER IV

FERRITE COPLANAR WAVEGUIDE PROPAGATION CONSTANT ANALYSIS

This chapter consists of measurements, conducted on a ferrite backed CPW, to validate the propagation constant for a z-directed bias field. The measurements serve to support the use of the FEM for phased array analysis and design. This chapter also demonstrates the importance of analyzing the static magnetic field distribution when using ferrite patch antennas.

4.1 CPW Propagation Analysis

4.1.1 Introduction

As seen in Chapter 3, ferromagnetic materials are extremely useful for microstrip antenna applications. However, Chapter 3 primarily focused on isolated microstrip antenna elements. Certainly, single elements are important, but the added functionality which ferrites provide for antenna arrays is of greater interest. Particulary, variable tuning of an applied bias field, can be used for array beam steering. This method is more advantageous than conventional electronically steered arrays [33].

For beam steering to occur, it is necessary to vary the phases of the individual array elements. For microstrip arrays, this entails changing the phase of the feeding

network/microstrip feed lines. This can be accomplished by replacing different length sections of the feed line substrates (dielectric) with ferrite material. Thus, when the feed lines are biased with an appropriate external magnetic field, the phases along the individual lines will vary, thereby causing beam steering. This steering can then be controlled simply by changing the bias field. This method of beam scanning is discussed, in detail, in Chapter 5.

To numerically model the combination of a phased array printed on a dielectric substrate and a feed line printed on a ferrite substrate, we must employ a method allowing for inhomogeneous material modeling in the substrate region. The FEM is a natural choice because it is capable of simulating inhomogeneous structures. A necessary step before proceeding with the array analysis was to ensure that the FEM was able to effectively compute $\mathcal{J}_{eff}$, within the ferrite medium, as the frequency and applied bias field were varied. As will be discussed in Chapter 6, determining $\mathcal{J}_{eff}$ in the ferrite substrate is necessary to obtain optimum bias field values for beam steering.

In this chapter, experimental measurements and numerical results are shown for a z-biased ferrite CPW. The measurements were carried out using a network analyzer, and the corresponding S parameters were found for the simple 2-port circuit. The S parameters were then used to extract the propagation constant of the CPW transmission line (TL) The measurements were conducted from 1 - 4 GHz, and 2 different biasing variations were measured (unbiased and biased) using external magnets. For validation, computations employing the FEM were performed for the CPW geometry. The longitudinal electric field values in the CPW slots were graphed, and the corresponding wavelength was measured using the standing wave pattern. The corresponding $\mathcal{J}_{eff}$ values were then extracted and compared to measurements.

For the remainder of this chapter, the details of the measurement setup (CPW geometry, dimensions, and relevant material parameters) are given first, followed

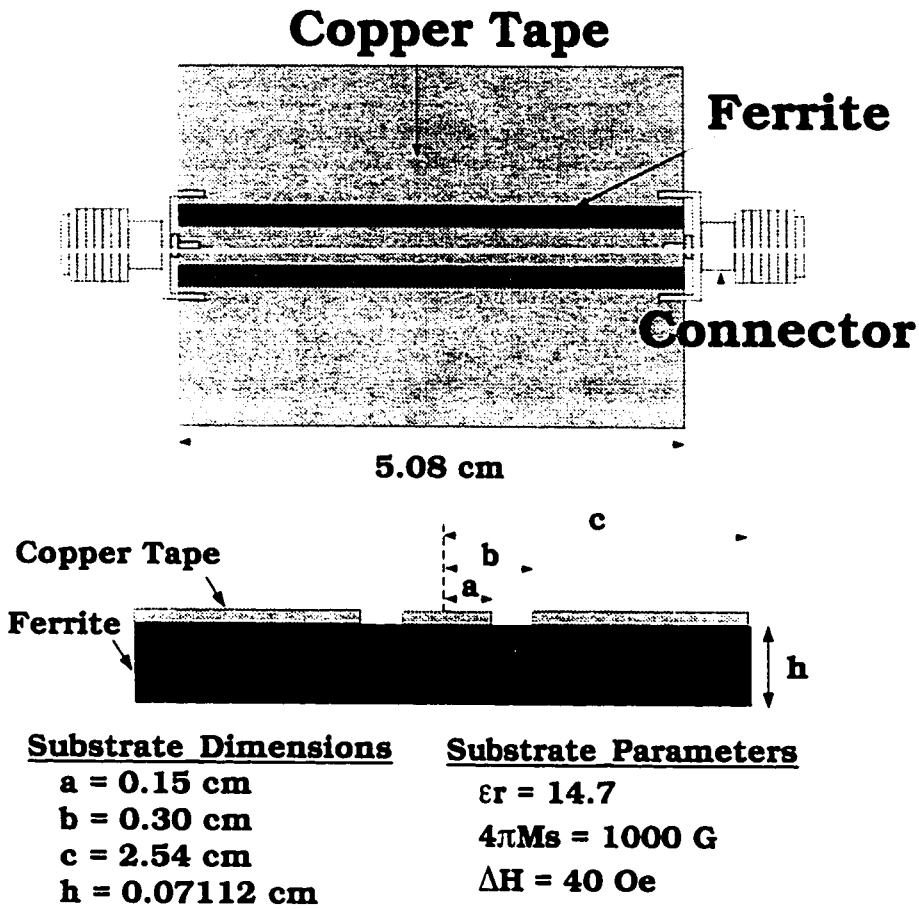

Figure 4.1: Coplanar waveguide geometry, substrate dimensions, and substrate parameters.

by measurement data. Next, details of the corresponding numerical simulations are shown, followed by a comparison of measured and calculated data. A brief summary concludes the chapter.

4.1.2 Measurements

Figure 4.1 shows the CPW geometry along with the corresponding dimensions and parameters. The rectangular substrate is composed of a TransTech G-1010 ferrite garnet which is a low loss ferromagnetic material. A CPW with finite ground planes was created on the ferrite substrate, using copper tape for the ground planes and

Material	B_r (Gauss)	H_c (Oersted)
G1010 Ferrite	694	0.55
Magnet (NdFeB)	12,300	11,300

Table 4.1: Magnetic material characteristics.

the conducting strip. SMA female connectors were then soldered onto the copper tape. The brass connectors were gold plated with gold plated contacts. The slot width ($s = b - a$) and conducting strip width ($w = 2a$) were chosen to produce a characteristic impedance (Z_{o_c}) equal to 61 Ω. This was done to minimize the impedance mismatch between the network analyzer and the CPW TL as much as possible with the given geometric parameter constraints. The value for Z_{o_c} was computed using the analytical formula for a CPW TL with finite ground planes and a finite substrate [24]. It is important to note that this computation does not account for perturbations in Z_{o_c}, due to the ferrite bias field, since μ_{eff} is no longer unity due to H_o.

A CPW TL was chosen over a more simple microstrip TL because an extremely narrow conducting strip would have been necessary to achieve a Z_{o_c} near 50 Ω, due to the small substrate height and high permittivity. Figure 4.2 shows a plot of Z_{o_c} versus the strip width W. The plot shows that for a microstrip impedance near 50 Ω, it is necessary to have $W \simeq 0.04$ cm which is impractical when using copper tape for the conducting strip. NdFeB permanent magnets were used as the external bias source. The specifications for the magnet are listed in Table 4.1. B_r is the remanent magnetization and is the value of the magnetic flux density when the magnetic field used to bias the magnet is zero. H_c is the coercive force and represents the bias field strength necessary to reduce the magnetic flux density to zero. The magnets used were rectangular blocks with the dimensions: $2'' \times 2'' \times 0.15''$.

A network analyzer was used to compute the S parameters for the 2 port CPW TL circuit. Measurements were taken in the frequency range 1 - 4 GHz, under unbiased

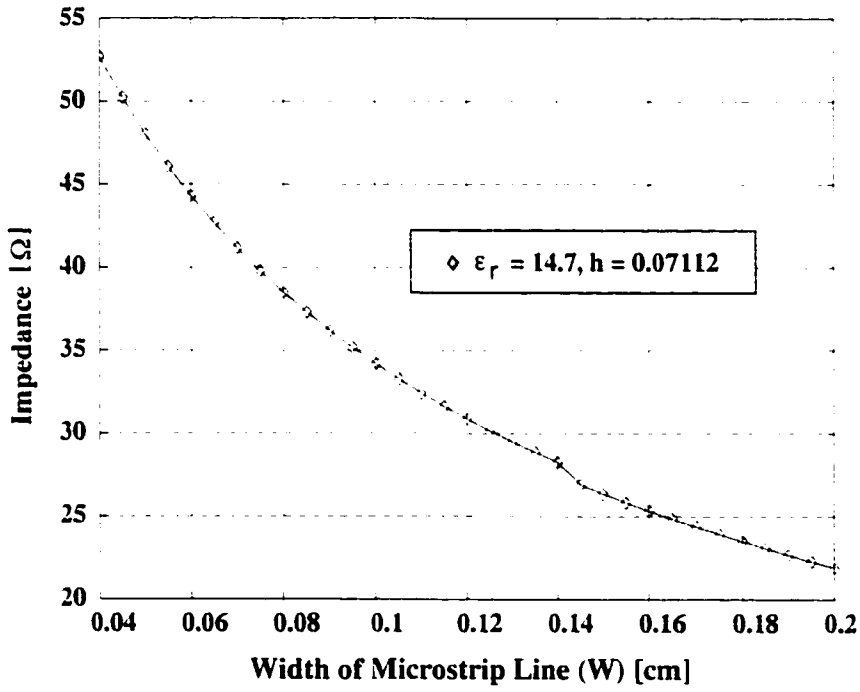

Figure 4.2: Microstrip TL characteristic impedance versus strip width.

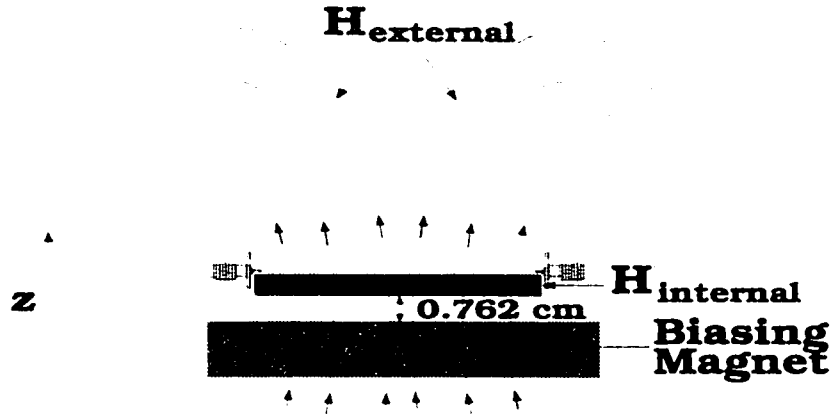

Figure 4.3: Biasing configuration.

and biased conditions. For the biased case, the magnet was placed underneath the CPW TL as shown in Figure 4.3. The magnet had a magnetic field intensity of 1900 Oe at a distance of 0.762 cm. In order to maintain this separation distance between the CPW TL and the biasing magnet, a piece of styrofoam was used that had a thickness of 0.762 cm. Figure 4.3 also denotes an external and an internal magnetic field. This is because the magnetic field inside the ferrite substrate does not equal the externally applied magnetic field. For a ferromagnetic material placed in a uniform magnetic field, H_e, the internal magnetic field, H_i, is

$$H_i = H_e - N_r(4\pi M_s) \tag{4.1}$$

where N_r is the demagnetization factor with subscript $r = x, y,$ or z depending on the bias field direction. For a rectangular slab, $N_x = 0$, $N_y = 0$, and $N_z = 1$. So for this particular case, $H_i = H_e - 4\pi M_s$, since the applied bias is z directed.

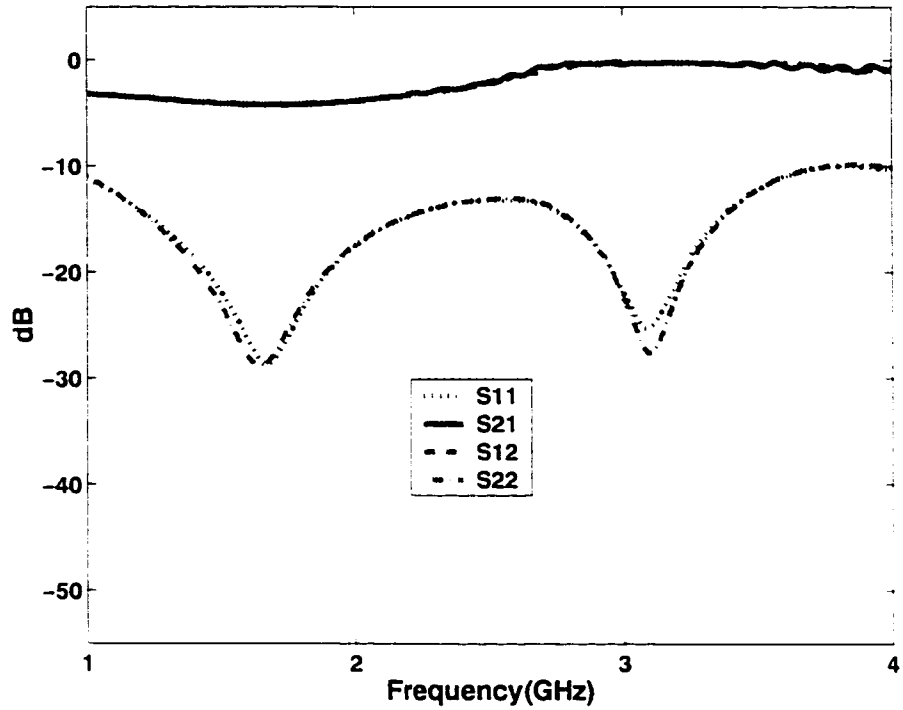

Figure 4.4: Measurement of S parameters, unbiased.

From equation 4.1, H_i for the CPW ferrite substrate due to the biasing magnet is 900 Oe ($4\pi M_s$ = 1000 G). For the case of 2 magnets, the magnetic field intensity is 3000 Oe at a distance of 0.762 cm resulting in H_i = 2000 Oe for the ferrite substrate. These values were used in the numerical simulations which will be discussed in section 4.1.3.

Figures 4.4, 4.5 and 4.6 show the S parameters for both the unbiased and biased cases. Figure 4.4 shows that for the unbiased case the CPW TL is matched well particularly near the frequencies 1.65 GHz and 3.1 GHz. For the single magnet bias case, the frequency regions where the TL is well matched are shifted in frequency, in comparison to the unbiased measurements. This is attributed to the bias field which changes the impedance of the ferrite TL.

For the dual magnet case, the same frequency shift occurs near 1.5 GHz similar to the single magnet biasing. However, the frequency shift of the second null in

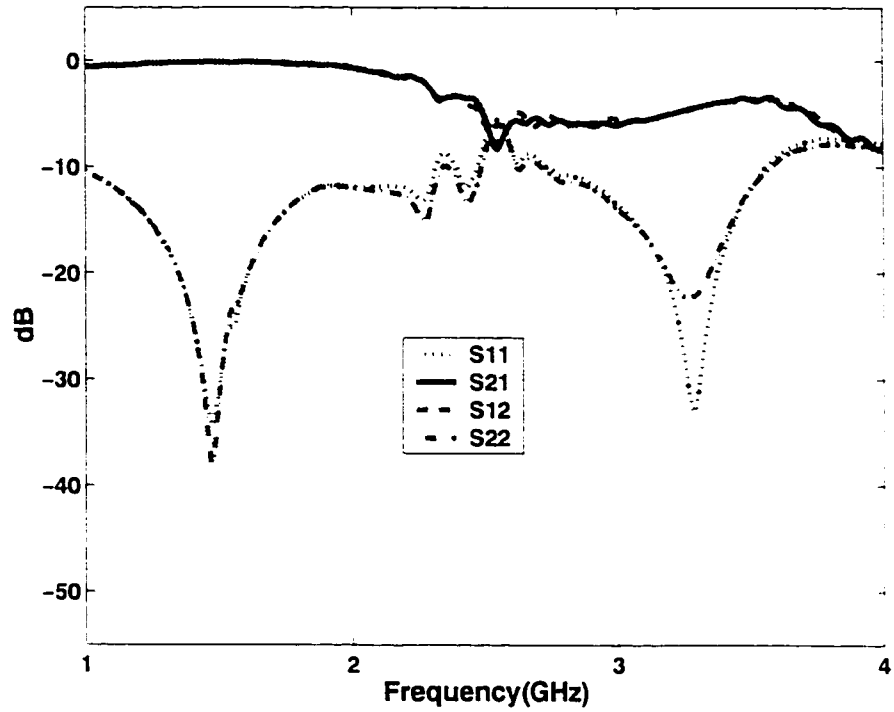

Figure 4.5: Measurement of S parameters, biased (1 Magnet).

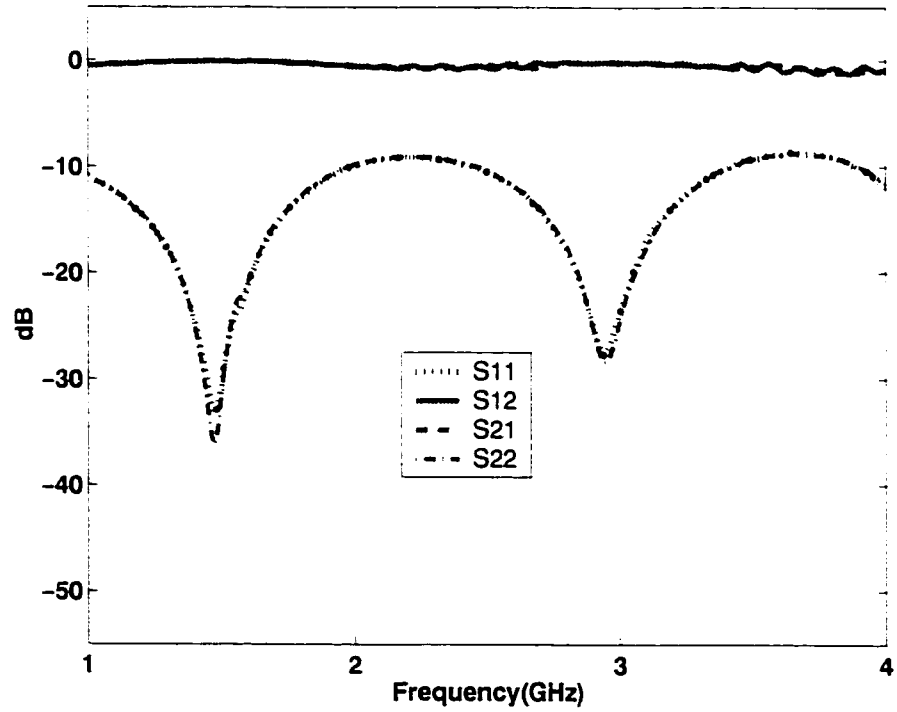

Figure 4.6: Measurement of S parameters, biased (2 Magnets).

the S_{11} and S_{22} parameters moves below 3 GHz. From Figure 4.6, the S_{12} and S_{21} values show that the CPW is well matched. The unstable S parameter behavior is not present in the dual magnet case because of the increased magnetic field strength intensity.

4.1.3 Numerical Simulations

As mentioned earlier, a FE analysis, described in section 4.1.1, was used to conduct the numerical simulation of the CPW TL. The FEM was used to generate the electric field values within the CPW slots. These values were then used to plot the standing wave pattern inside the slots. From basic TL theory, the wavelength of the standing wave on a TL line can be found by measuring the distance between successive minima or maxima, or the distance between minima and maxima [58]. The distance between successive minima or maxima is $\frac{\lambda_g}{2}$ and the distance between minima and maxima is $\frac{\lambda_g}{4}$. Thus, λ_g was extracted by observing the computed standing wave pattern and then used to obtain $\beta_{eff} = \frac{2\pi}{\lambda_g}$. This calculated β_{eff} was then used to compare with the β_{eff} found from the measurements. In order to verify the accuracy of the FEM for this type of analysis, a validation was performed using data from [80]. In [80], an open-circuited microstrip line on a biased ferrite substrate was analyzed using the MoM. Figure 4.7 shows the comparison between results achieved using the FEM and MoM. Figure 4.7 clearly shows excellent agreement between the two numerical methods.

The FEM model assumed a metal-backed cavity. A boundary integral (BI) method was used to couple the interior region of the cavity with the external domain via the cavity aperture. Since the CPW TL was not backed by a ground plane, this was a necessary consideration for modeling the CPW line in the FE simulation. Initially, an absorber was used for the CPW TL modeling. Placing the absorber at the bottom of the cavity decreases the number of layers needed to model the ferrite/air

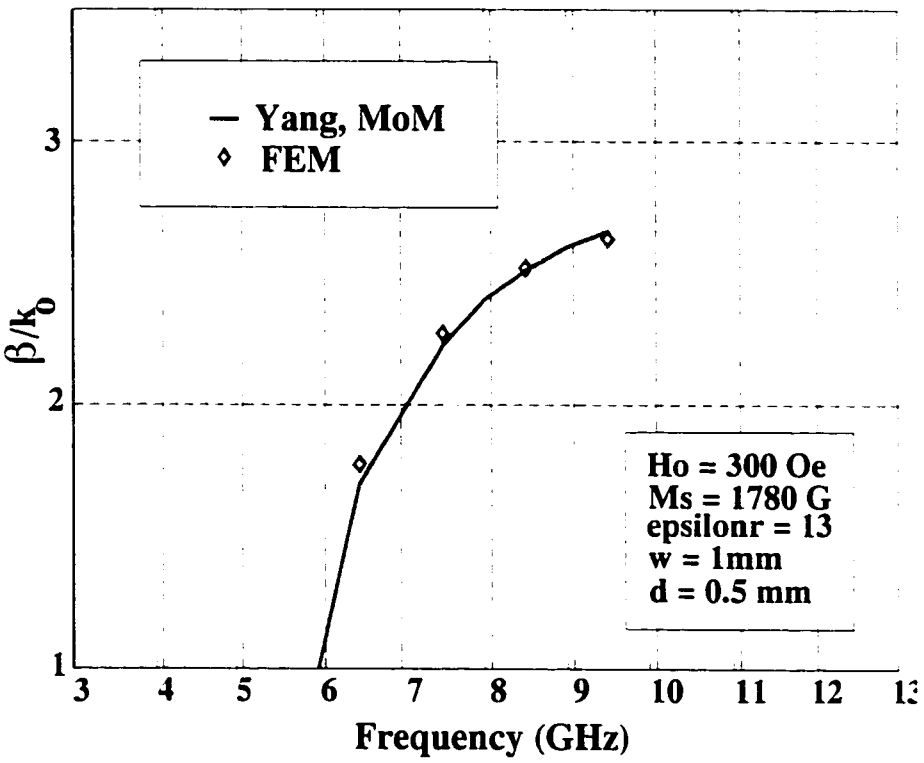

Figure 4.7: FEM propagation constant validation for an open circuited TL with y bias.

Figure 4.8: Cavity with bottom absorber layer.

interface, thereby reducing the number of unknowns for the problem. However, the simulation computation time increases (In comparison to a free space layer where $\mu_r = \epsilon_r = 1$.) with the use of an absorber which is disadvantageous. Figure 4.8 shows the geometry for the simulation. There are 3 layers: layer 1 - ferrite substrate, layer2 - air, layer 3 - absorber($\mu_r = \epsilon_r = 1 - 2.2j$).

To observe the absorber's performance, the unbiased CPW line was simulated. Figures 4.9 and 4.10 show the tangential electric fields at different depths in the cavity, for the unbiased CPW TL and the biased CPW TL respectively. Inspecting the plots, it is apparent that the absorber demonstrates no significant advantage. Replacing the absorber with another air layer produced the same results. As a result, we can conclude that the CPW's wavelength was not affected by reflections from the ground plane and therefore no absorber was placed at the cavity bottom. Instead, several more air layers were introduced to ensure that the cavity bottom did not interfere with the calculations thereby providing accurate parameter extraction. Figure 4.11 shows the new geometry for the simulation.

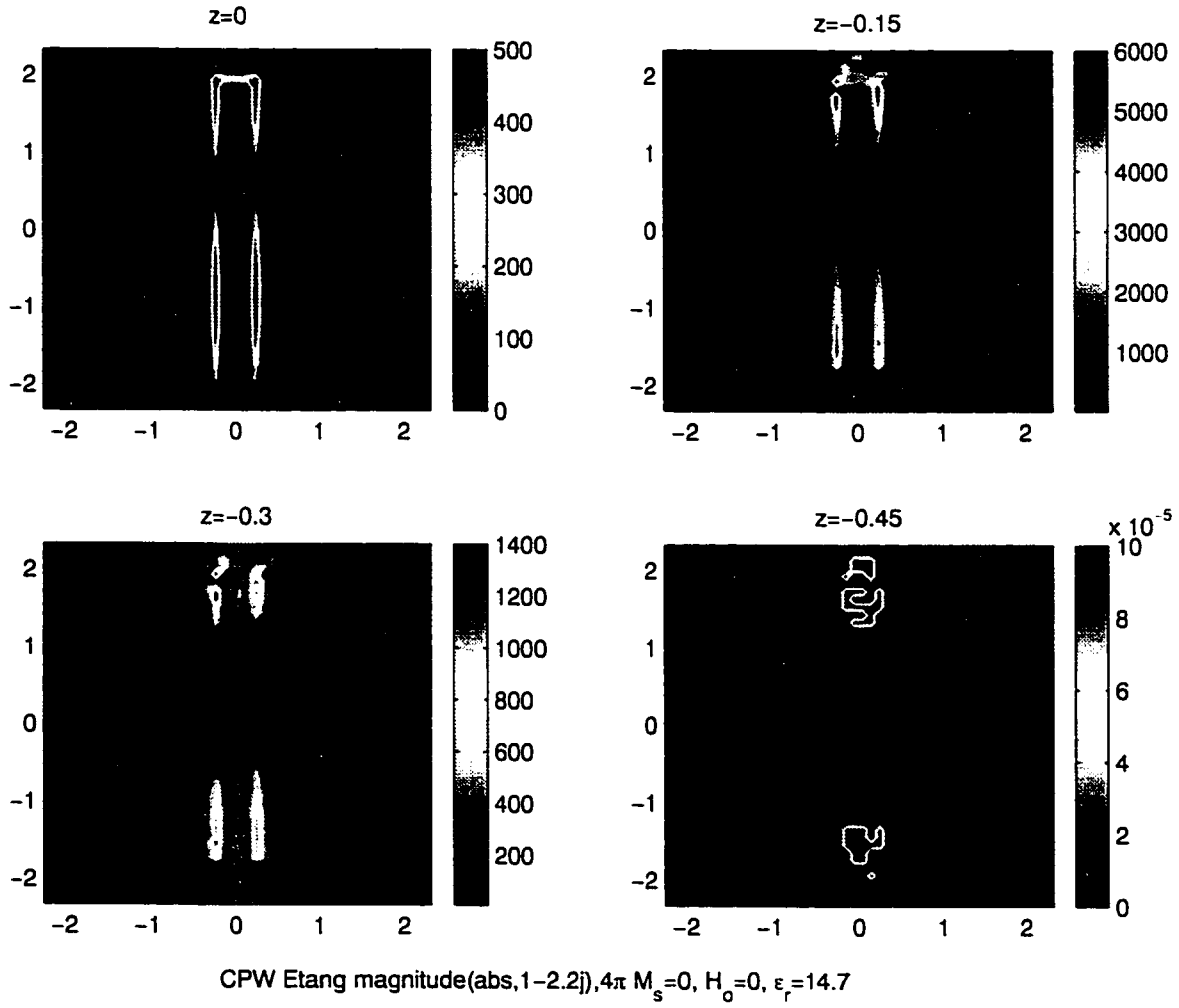

Figure 4.9: Surface electric fields with absorber at cavity bottom

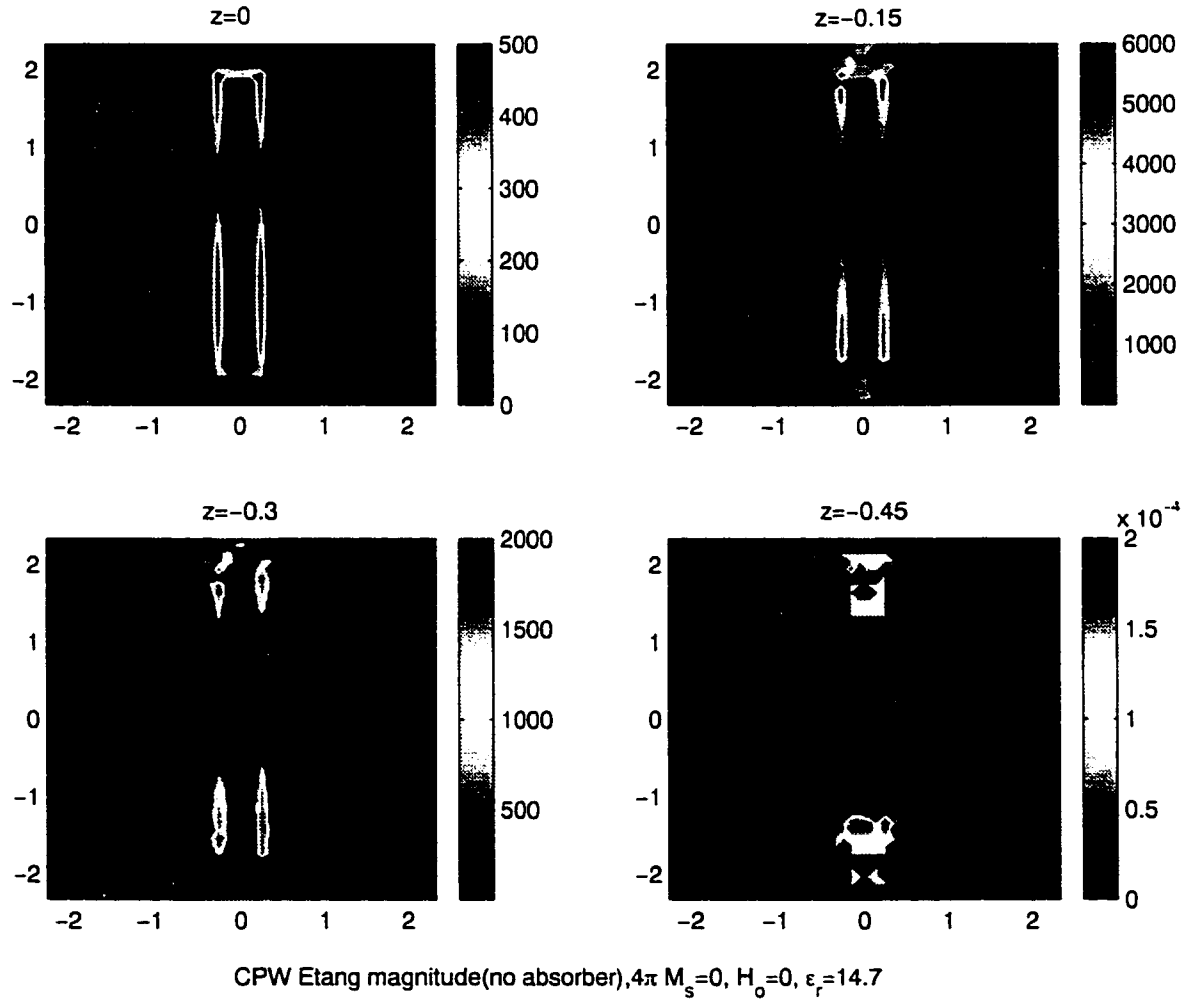

Figure 4.10: Surface electric fields with no absorber at cavity bottom.

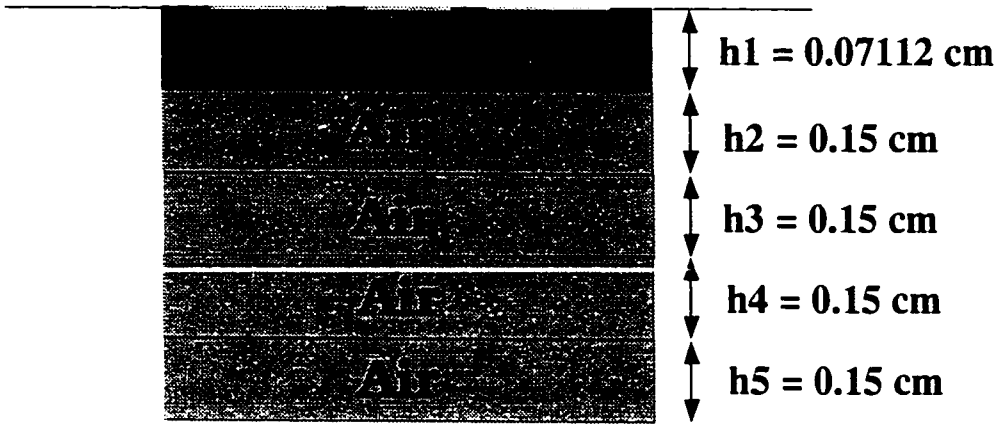

Figure 4.11: Cavity with No Absorber Layer.

4.1.4 Results

Only the dual magnet case will be considered for the following comparison. This is because the dual magnet setup maintains a better uniform magnetic field within the substrate, because there is a smaller fringing magnetic field contribution as opposed to the single magnet case. Also, the effects of the bias on the field propagation within the ferrite are not apparent when no bias is present, hence comparison with the unbiased case is of little interest. As mentioned earlier, the external bias field for the dual magnet setup was 3000 Oe. This corresponds to a magnetic field intensity of 2000 Oe internal to the ferrite substrate, and is the value used for the simulations.

After measuring the S paramters for the biased CPW, it was necessary to find a method of extracting the value of the propagation constant, β_{eff}, from the measurement data. The approach used was to calculate the reflection coefficent, Γ, at port 1 and extract β_{eff} from the phase of Γ. The CPW TL can be modeled by the basic TL shown in Figure 4.12. The general expression for Γ as a function of TL length is

$$\Gamma(z) = \frac{|V_1^-|}{|V_1^-|} e^{j\Delta\phi} e^{j2\beta_{eff}z} \tag{4.2}$$

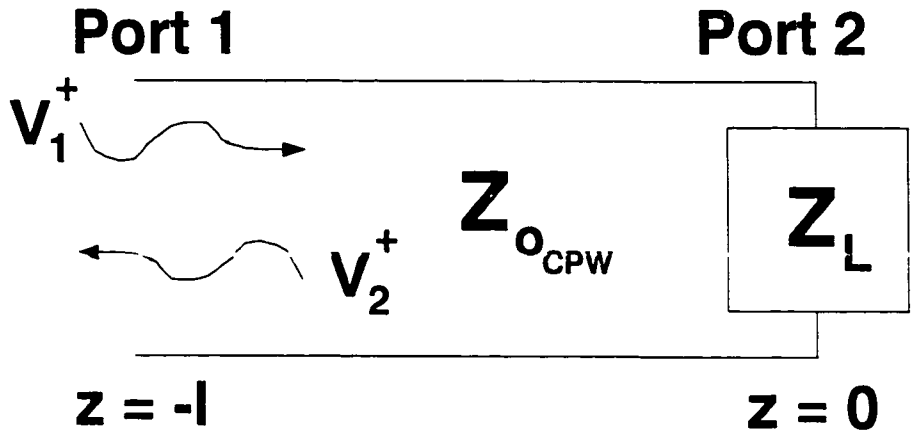

Figure 4.12: Transmission line model of the CPW 2 port circuit.

where $\Delta\phi = \phi^- - \phi^-$ and ϕ^- and ϕ^- are the phases of V_1^- and V_1^- respectively. From Equaton 4.2. it is apparent that β_{eff} is not a function of the load impedance at port 2 which implies that any load impedance can be used to compute β_{eff}. For the measurement comparison. an open circuit was used to compute Γ since for an open circuit. $\Delta\phi = 0$. Γ at port 1 then becomes

$$\Gamma_{port_1} = \Gamma(-l) = \frac{|V_1^-|}{|V_1^-|} e^{-j2\beta_{eff}l} \tag{4.3}$$

In order to extract β_{eff} from the measurements it is necessary to find an expression for (4.3) in terms of the S parameters. To do so. we begin with the definition of the scattering matrix

$$\begin{bmatrix} V_1^- \\ V_2^- \end{bmatrix} = \begin{bmatrix} S_{11} & S_{12} \\ S_{21} & S_{22} \end{bmatrix} \begin{bmatrix} V_1^- \\ V_2^- \end{bmatrix} \tag{4.4}$$

where the subscripts 1 and 2 refer to ports 1 and 2 respectively. S_{ij} are the S-parameters of the 2-port network. and the $\pm$ superscripts refer to the outgoing and incoming waves at the respective ports. For an open circuit ($Z_2 = \infty$). $V_2^- = V_2^-$.

and after substituting into (4.4)

$$\frac{V_1^-}{V_1^-} = S_{11} + S_{21}\frac{S_{12}}{1 - S_{22}} = \Gamma_{port_1}. \tag{4.5}$$

This provides us with an explicit relation between Γ_{port_1} and S_{ij}. The propagation constant can be extracted from 4.3 once Γ_{port_1} is computed.

For the numerical simulations, β_{eff} was found by exploiting standing wave pattern properties. The distance between consecutive maxima or minima along the standing wave pattern, on the CPW TL, corresponds to a distance of $\frac{\lambda_g}{2}$, where λ_g is the guided wavelength. From a knowledge of λ_g, then

$$\beta_{eff} = \frac{2\pi}{\lambda_g}(rad/m). \tag{4.6}$$

Figure 4.13 shows the initial comparison between measurements and simulations. Theoretically, H_i should be 2000 Oe which corresponds to the lowest set of points in Figure 4.13. However, the curve corresponding to H_i = 2000 Oe differs substantially from the measurements. A lower value of 1050 Oe was initially tried for H_i (in the simulations) to better match the measured data. Although the lowering of H_i increased the simulation values for β_{eff}, as seen from Figure 4.13, the increase was small. This meant that some other physical phenomenon in the ferrite substrate was the cause for the differences between measurements and calcualtion. The investigation showed that the uniform nature of the external ferrite fields was responsible for the discrepancies. To obtain the correct distribution of H_i, a static field analysis was necessary. The next section contains a static analyisis of the configuration, subject to the applied DC magnetic field generated by the bias magnets.

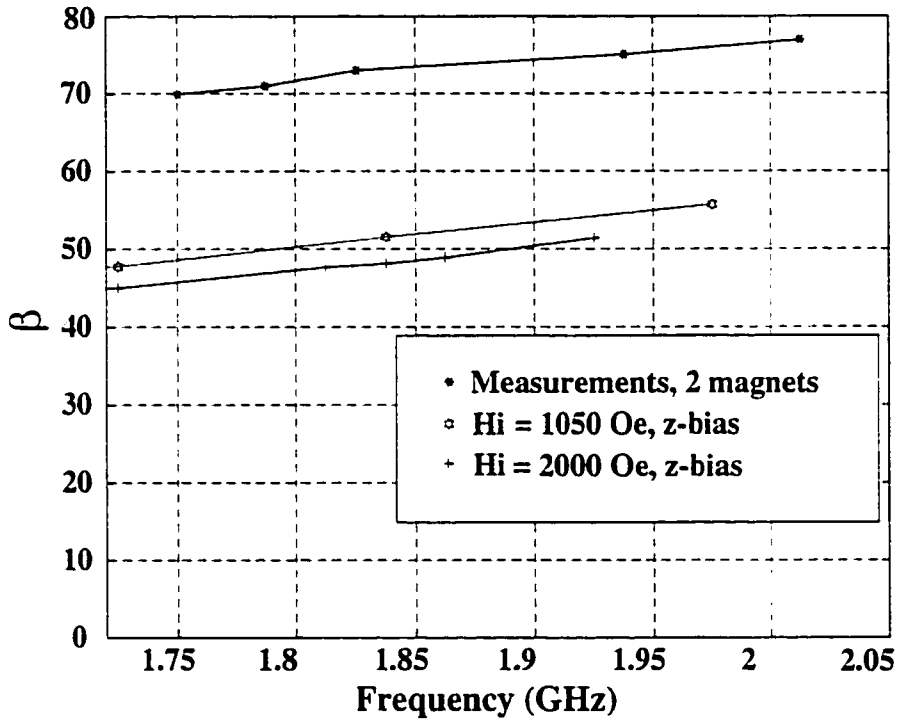

Figure 4.13: Propagation constant comparison between measurements and numerical simulations.

4.2 Static Magnetic Field Analysis

4.2.1 Introduction

As seen in the previous chapter, ferrites can be used for improving the bandwidth of patch antennas by varying the applied bias field. The phenomenon responsible for these characteristics is the interaction between the AC and DC magnetic fields, occuring within the ferrite material. For the radiating structures considered in this thesis, the AC magnetic field is that associated with the patch and/or microstrip feed line. The DC field is attributed to an external magnet with sufficiently strong magnetic flux density to bring the ferrite into saturation. This is because below saturation, the ferrite material becomes lossy, and more importantly the AC interaction is reduced [58]. To this point, emphasis has only been placed on the ferrite characteristics when the ferrite substrate is properly biased. For completeness, it is necessary to analyze the source of the bias magnetization, and it's effect on the ferrite's performance. To accomplish this, a characterization of the magnetic field distribution for the biasing magnet(s) is necessary.

Permanent magnets are generally used to generate the bias magnetic field source. This is concurrent with the existing literature on ferrite antenna applications. The permanent magnet produces a magnetic field, H_e, which in turn creates an internal magnetic field distribution, H_i, within the ferrite substrate. When modeling a ferrite antenna, it is necessary to know precisely the value of the internal magnetic field, in order to perform an accurate numerical analysis. As noted earlier (see section 4.1.2),

$$H_i = H_e - 4\pi M_s \tag{4.7}$$

relates H_i and H_e. The saturation magnetization value, $4\pi M_s$, is readily known for a given commercially available ferrite. Thus, H_i can be obtained once H_e is known.

and to accomplish this it is necessary to model the permanent magnets. The DC magnetic field distribution produced by the magnet is not changed. Since the DC magnetic field is decoupled from the concurrent presence of RF fields, a static field analysis of the permanent magnet suffices. Of particular interest is the evaluation of nonuniformities in H_e due to fringing.

The following section describes the theory involved to solve for the magnetic fields produced by a magnet biasing a ferrite rectangular block. The issues related to bias field nonuniformity will be addressed as they relate to the computation of $\mathcal{J}_{eff}$ inside the TransTech G-1010 ferrite substrate.

4.2.2 Theory

4.2.3 Fundamental Magnetostatic Principles

Maxwell's equations for the static case can be reduced to

$$\nabla \cdot \mathbf{D} = \rho_v. \tag{4.8}$$

$$\nabla \times \mathbf{E} = 0. \tag{4.9}$$

$$\nabla \cdot \mathbf{B} = 0. \tag{4.10}$$

and

$$\nabla \times \mathbf{H} = \mathbf{J}. \tag{4.11}$$

These equations can be separated into two uncoupled pairs in which the electric and magnetic fields are independent of each other. Therefore, when solving for magnetostatic fields, the relevant equations are 4.10 and 4.11 which include the magnetic flux density ($\mathbf{B}$), the magnetic field intensity ($\mathbf{H}$) and the static current density ($\mathbf{J}$).

For magnetic materials, the constitutive relation, $\mathbf{B} = \mu_o \mathbf{H}$, must be modified to include the effects of magnetization. In this case, the magnetization vector (M) must be included in the definition of **B**. **M** is a function of **H**, such that

$$\mathbf{M} = \chi_m \mathbf{H}. \tag{4.12}$$

where χ_m is the susceptibility of the magnetic material, and can be on the order of 1×10^6 [9]. For ferromagnetic substances, χ_m is nonlinear and hysteretic. This means that the ferromagnetic substance has a material history which depends upon **M**. Figure 4.14 shows a sample hysteresis curve for a typical ferromagnetic material [72].

When the substance is initially biased, **B** increases with **H** as seen along path $\overline{OA_1}$. When **H** is decreased, **B** does not travel along it's initial path but traverses a different path while decreasing in magnitude. When $\mathbf{H} = 0$, **B** is no longer 0 but retains a value which is called the remanent magnetic flux density, and will be denoted as B_r. To cause **B** to return to 0, a *negative* bias must be applied, and the value of **H** which reduces **B** to 0 is called the coercive force, denoted as H_c. When the process is reversed, it is observed that **B** increases along another path ($\overline{A_4A_1}$) (see Figure 4.14). The combination of these different paths form what is referred to as the hysteresis loop, and varies for different ferromagnetic materials.

Due to the aforementioned properties, the equation for **B** must be modified. The relation for **B** becomes

$$\mathbf{B} = \mathbf{H} + 4\pi \mathbf{M_s} = \mu \mathbf{H} = (1 + \chi)\mathbf{H} \tag{4.13}$$

and $\chi = \frac{4\pi M_s}{H}$. Thus, **B** is dependent upon the magnetic field and the magnetization of the magnetic material.

When dealing with magnetostatic problems, the end goal is to find the magnetic

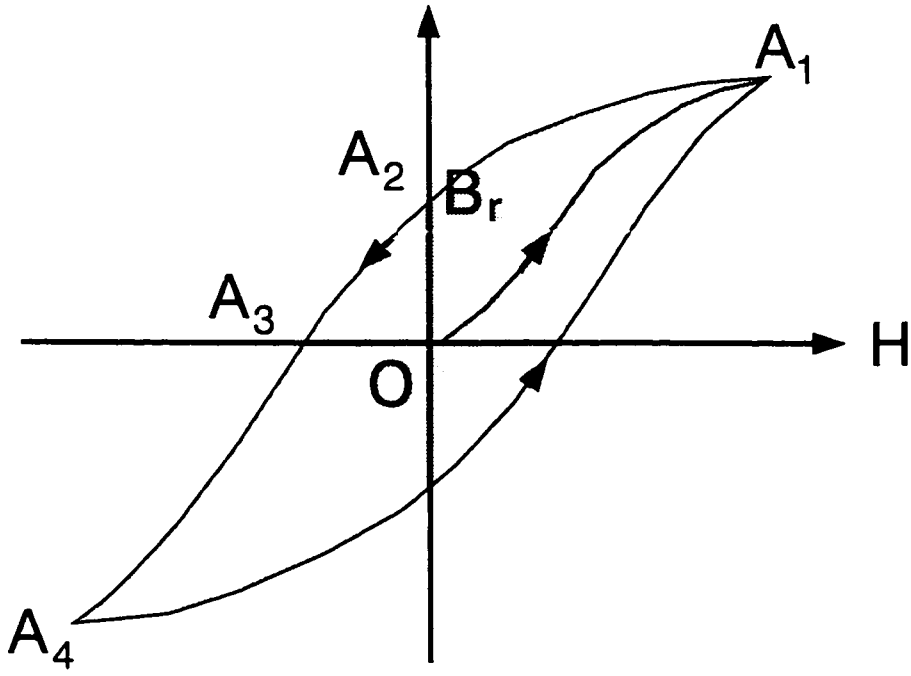

Figure 4.14: Hysteresis curve.

field distribution due to a current source and/or magnetic material. This can be accomplished using either a magnetic *vector* or a magnetic *scalar* potential approach. For simple problems, Ampere's law or the Biot Savart law may also be used, but for problems involving a higher level of complexity the aforementioned approaches should be employed.

Because the magnetic flux density has zero divergence (Equation 4.10), it can be expressed as the curl of a potential **A** such that

$$\mathbf{B} = \nabla \times \mathbf{A} \tag{4.14}$$

implying that **B** can be determined from the vector potential **A**. To solve for **A**, Maxwell's equations in conjunction with a gauge condition (which completely spec-

ifies **A**) must be used. This leads to

$$\mathbf{A} = \frac{\mu}{4\pi}\int_{\Omega}\frac{\mathbf{J}}{\mathbf{R}}d\Omega \tag{4.15}$$

where $\mathbf{R} = |\mathbf{r} - \mathbf{r}'|$, and $\int_{\Omega}$, can be a volume, surface, or line integral depending on the current density **J**. After determing **A**, **B** is readily found through Equation 4.14.

The magnetic scalar potential can be used to solve magnetostatic problems involving current distributions and/or magnetic media. Unlike the magnetic vector potential, the scalar potential focuses on the magnetic field intensity (**H**) rather than the magnetic flux density (**B**). The unknown field **H**, can be separated into two fields: that generated by the current source(s), $\mathbf{H_s}$, and that generated by the ferromagnetic material, $\mathbf{H_m}$ [6]. Thus, the total magnetic field intensity can be represented as

$$\mathbf{H} = \mathbf{H_s} + \mathbf{H_m} \tag{4.16}$$

$\mathbf{H_s}$ can be solved using the Biot Savart law

$$\mathbf{H} = \frac{1}{4\pi}\int_{\Omega}\mathbf{J}\times\nabla(\frac{1}{\mathbf{R}})d\Omega. \tag{4.17}$$

Since $\nabla\times\mathbf{H} = \mathbf{J}$ and $\nabla\times\mathbf{H_m} = 0$, $\mathbf{H_m}$ can be represented by the *reduced scalar potential* (ϕ) as

$$\mathbf{H_m} = -\nabla\phi. \tag{4.18}$$

and thus,

$$\mathbf{H} = \mathbf{H_s} - \nabla\phi. \tag{4.19}$$

In this chapter it will be assumed that $\mathbf{J} = 0$ and thus $\nabla\times\mathbf{H} = 0$ as well. Consequently,

$$\mathbf{H} = -\nabla w \tag{4.20}$$

where ψ is the total scalar potential. With a slight change to account for the coercive field, $\mathbf{H_c}$, (4.13) becomes [6]

$$\mathbf{B} = \mu(\mathbf{H} - \mathbf{H_c}). \tag{4.21}$$

$\mathbf{H_c}$ must be included in (4.13), because for permanent magnets $\mathbf{B}$ does not equal zero when $\mathbf{H}$ equals zero. Since $\nabla \cdot \mathbf{B} = 0$, the governing equation for the scalar potential is

$$\nabla \cdot \mu \nabla \psi = \nabla \cdot \mu \mathbf{H_c}. \tag{4.22}$$

It is noted that $\mathbf{H_c}$ possesses significant values only for permanent magnets and for all other regions can be assumed to be zero.

For the remainder of this section the total scalar potential formulation is used to determine the bias field internal to the ferrite. This is particularly suited for the magnetostatic problem because there are no current sources.

4.2.4 Static Field Effects

In section 4.1.4, the propagation constant of a ferrite substrate was experimentally measured and compared with numerical simulations. To bias the ferrite substrate, a permanent magnet was used. Thus far, the numerical modeling for the experimental set-up assumed a uniform magnetic field across the ferrite substrate and of sufficient strength to cause saturatioin. However, the assumption of uniformity does not hold when the magnet and substrate are of finite size. Fringing effects contribute to changing the strength and polarity of the field. Thus, careful modeling is necessary to assess the correct field distribution.

To model the magnet and ferrite substrate, the Ansys FEM modeling software package was used to carry out the static analysis. Because the problem involved no steady currents, the total magnetic scalar potential (described in section 4.2.2) was used for the magnetic field solution. In contrast to the high frequency analysis

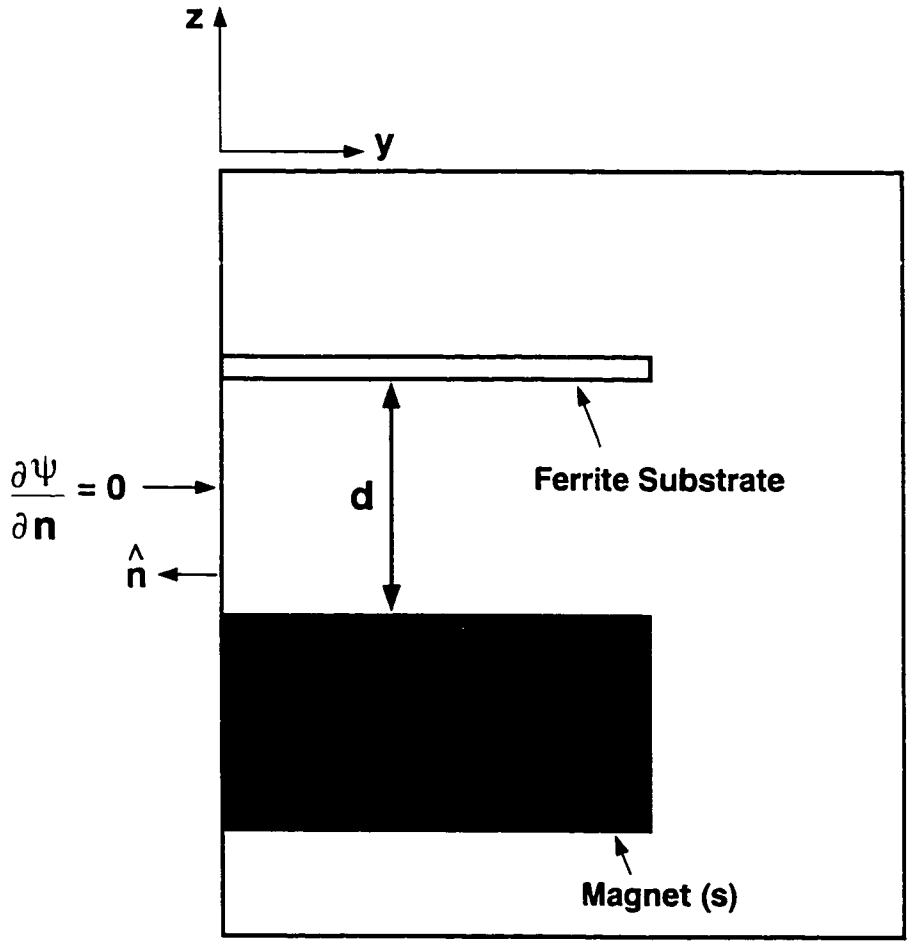

Figure 4.15: Magnetic FEM geometry.

discussed in Chapters 2 and 3, node elements were used to carry out the static FEM analysis. Because both the ferrite substrate and the magnet were square in geometry, symmetry was also taken into account. Thus, only half of the magnet and substrate were used in the computation provided the boundary conditions $\hat{n}\cdot\mathbf{H} = 0$ and $\frac{\partial \psi}{\partial n} = 0$ were enforced at the symmetry plane. Figure 4.15, depicts the FEM computational domain. For the remaining boundaries of the domain interior, surface elements were used to couple the fields interior to the FE region to the exterior space extending to infinity.

The ferrite substrate was modeled assuming a permeability constant of 1262. This

value of μ_r was computed using the available B_r and H_c values of the ferromagnetic material where $\mu_r = \frac{B_r}{H_c}$. The permanent magnet was modeled in a similar fashion as the ferrite substrate using a relative permeability constant of 1.12. The only difference is that the $\mathbf{H_c}$ value for the magnet is extremely large and must be taken into consideration. Also, the direction of $\mathbf{H_c}$ determines where the poles of the magnet are located. For the magnets used, the poles are located on the top and bottom faces, perpendicular to the z plane.

The CPW measurements were done with both 1 magnet and 2 magnets. From the magnetostatic simulations it was observed that for either magnet configuration, the distance between the ferrite substrate and the magnet(s) was too great. Thus, the external magnetic field around the magnet was not uniform, i.e. it's direction varied at different locations within the substrate. It was assumed that for the 1 magnet configuration the external field strength was 1900 Oe at 0.762 cm, which would correspond to an internal field of $900Oe$ within the ferrite ($H_{int} = H_{ext} - 4\pi M_s$, and $4\pi M_s = 1000\ G$).

Figures 4.16 and 4.17 show the magnetic field distribution for the single magnet configuration. Figure 4.16 shows the field distribution when the magnet is isolated. From these plots it is evident that the field distribution is not uniform particularly near the edges of the ferrite. Looking at Figure 4.17 an even more interesting result is apparent. Because the external field is not uniform around the ferrite substrate, the magnetic flux leaving the sides of the substrate are much greater than the flux near the top center of the ferrite, i.e. there is a great deal of flux leakage from the sides of the substrate due to fringing. Figure 4.18 further highlights the nonuniformity of the external magnetic field. It is clear that the distance used for the measurements was too large. The magnetic field internal to the substrate was not uniform except near its center. This is made clear by observing the magnetic flux leakage from the sides of the ferrite substrate.

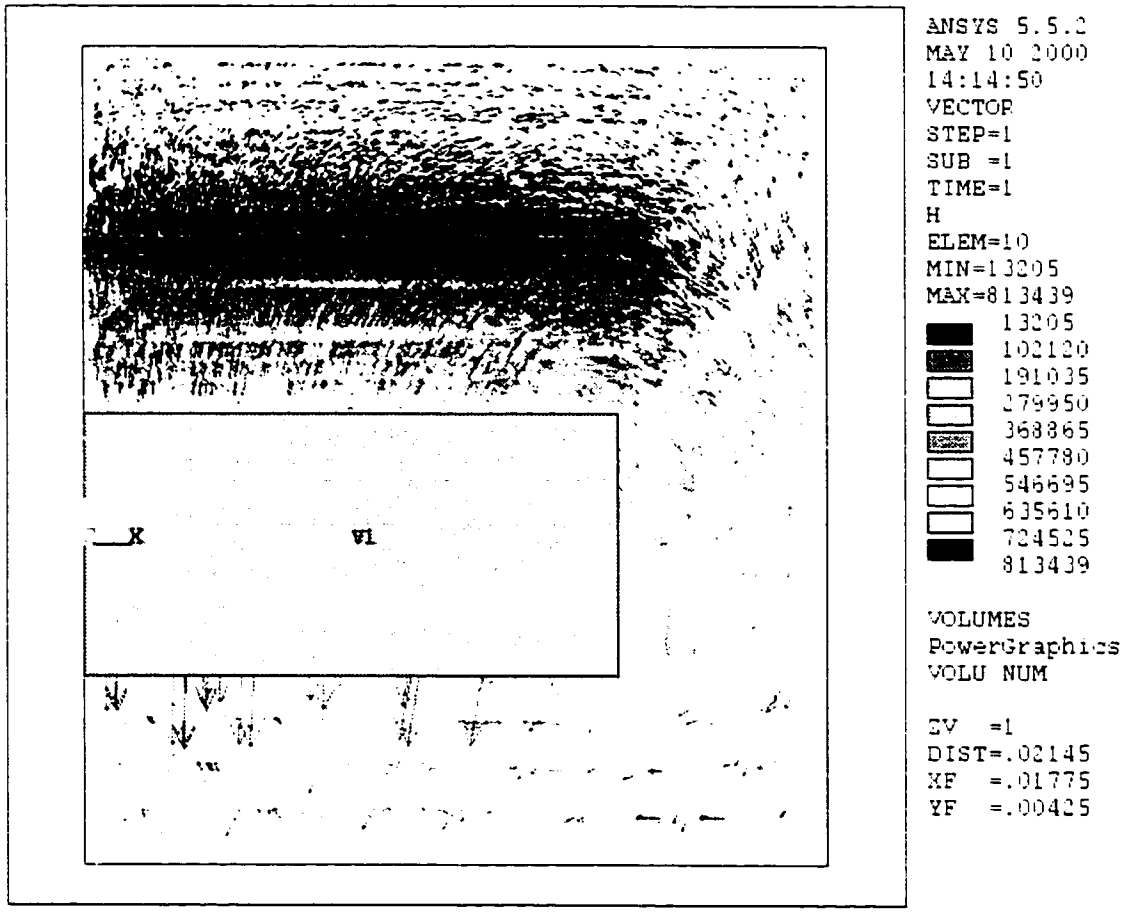

Figure 4.16: Magnetic field distribution without the ferrite substrate: one magnet simulation.

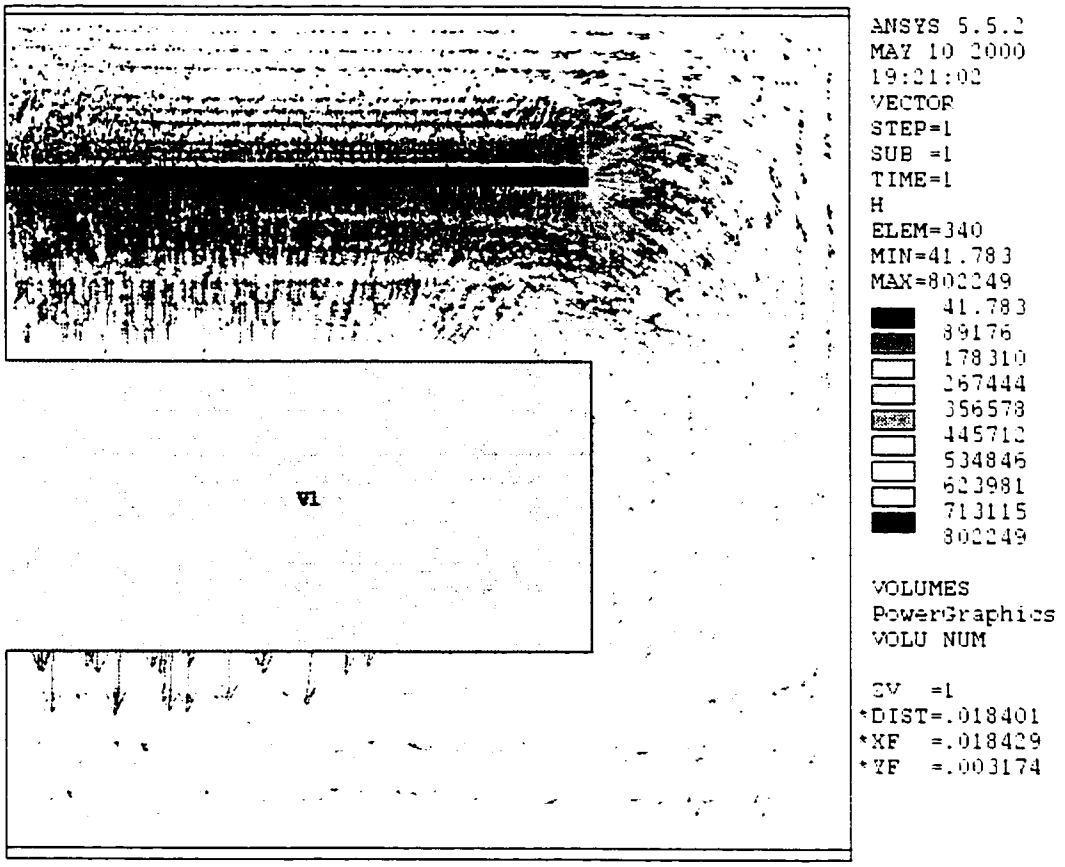

Figure 4.17: Magnetic field distribution exterior to the magnet in the presence of the ferrite substrate: one magnet simulation.

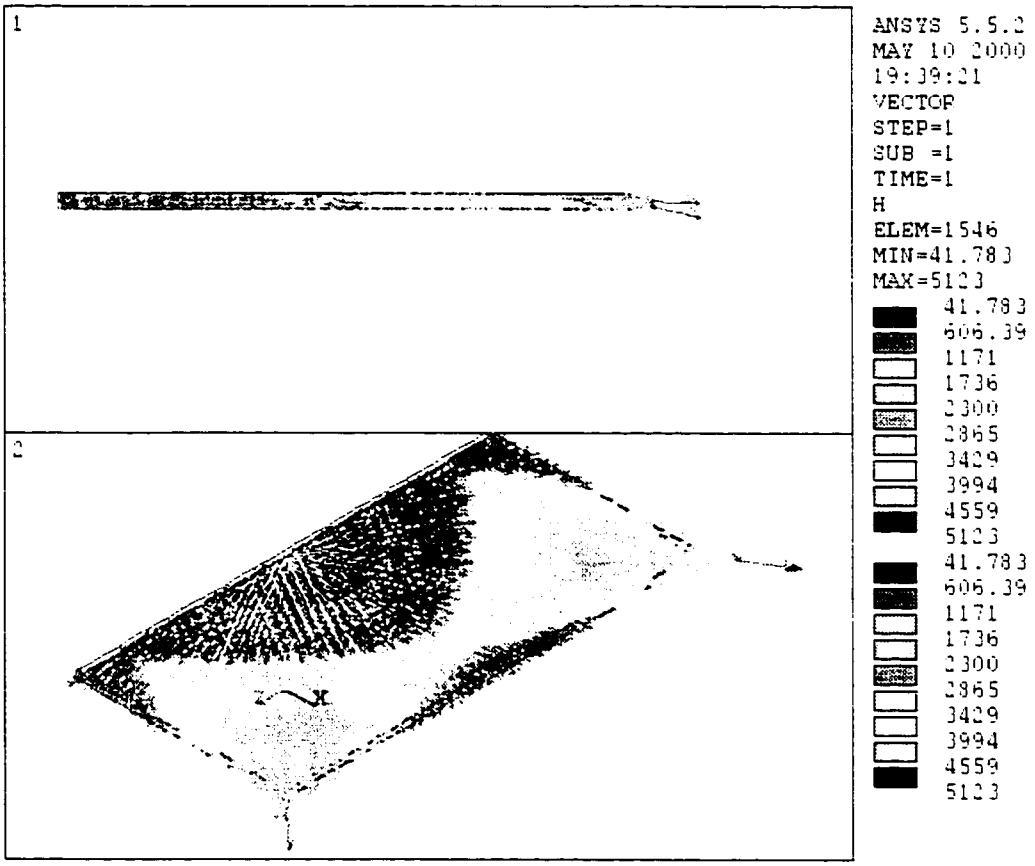

Figure 4.18: Magnified view of the magnetic field distribution, exterior to the magnet, in the presence of the ferrite substrate: one magnet simulation.

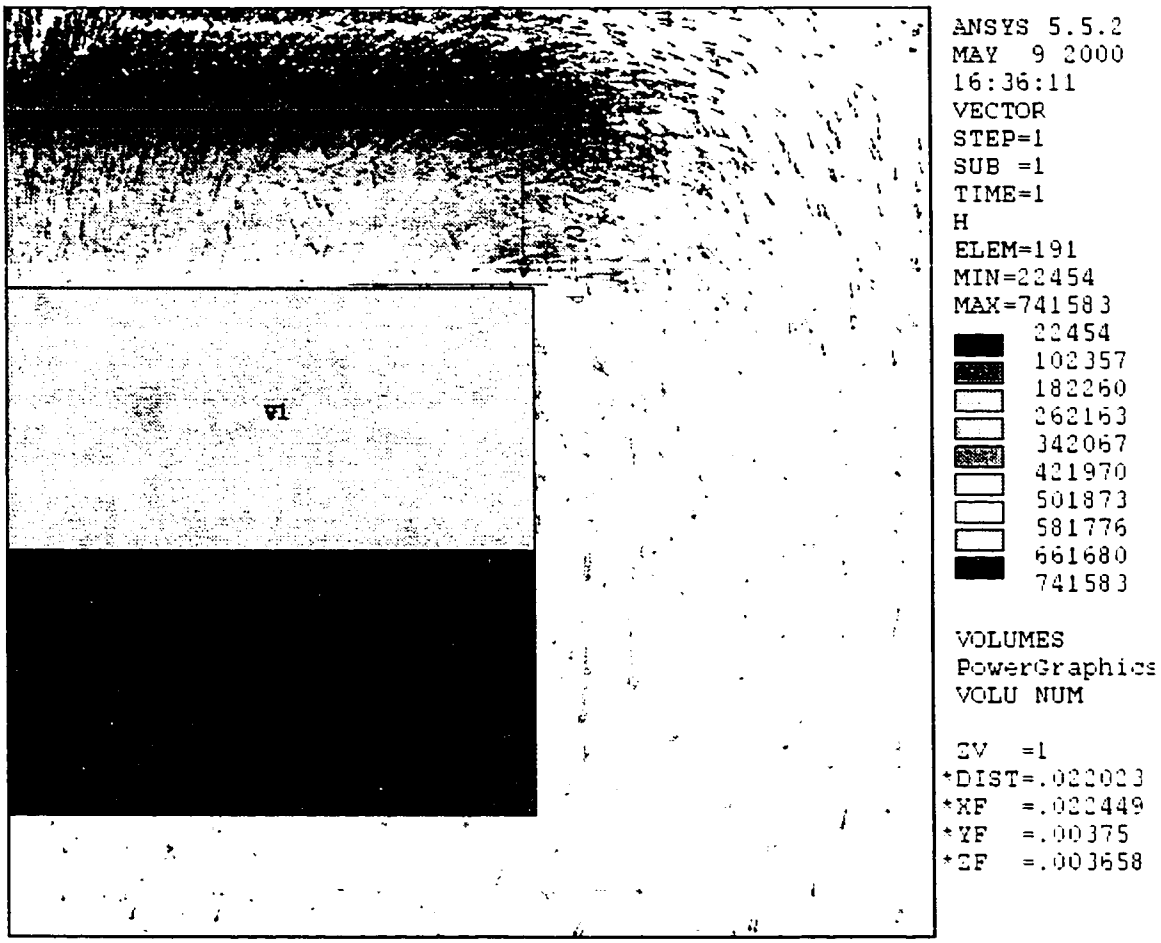

Figure 4.19: Magnetic field distribution due to two magnets without the ferrite substrate.

For the two magnet configuration, the combined strength of the magnet was assumed to be greater than one magnet. Furthermore, it was believed that not only would the external field produced by the magnets be stronger but it would also produce a more uniform H_i. Although these assumptions were indeed correct, the fringing of the fields was still too large near the ferrite substrate edges. Figures 4.19 and 4.20 show the magnetic field distribution for the double magnet configuration. Basically, the same flux leakage which occurred for the single magnet configuration also occurs for the two magnets. Figure 4.21, more clearly demonstrates this phenomenon.

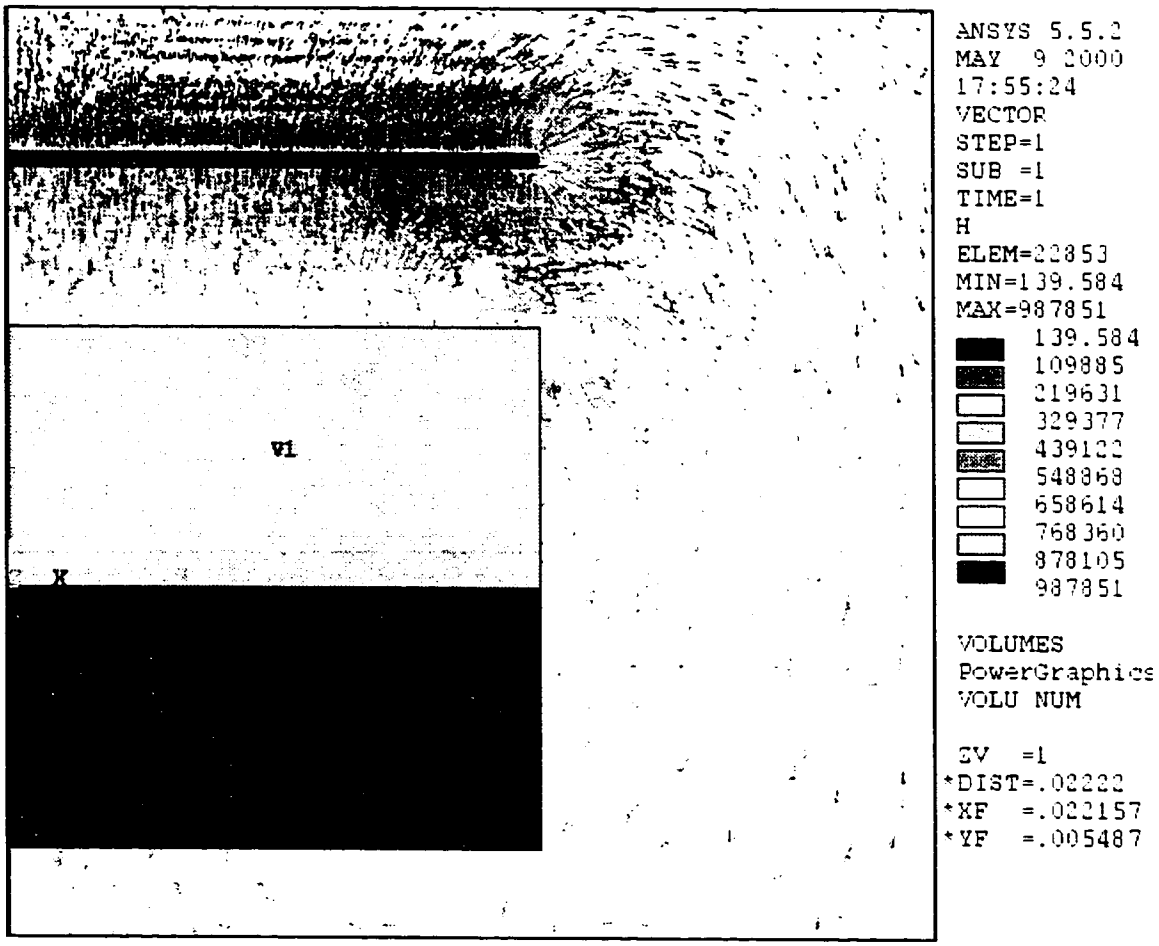

Figure 4.20: Exterior magnetic field distribution due to two magnets in the presence of the ferrite substrate.

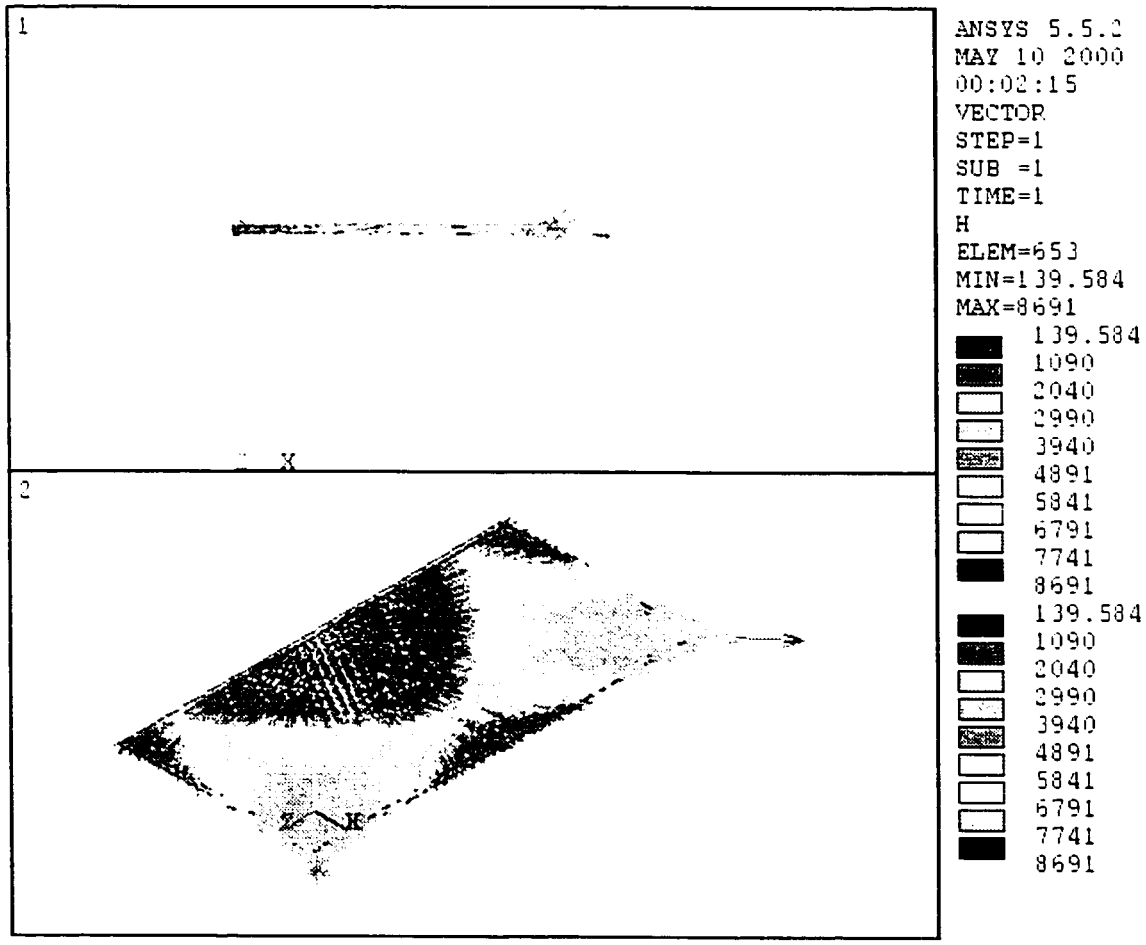

Figure 4.21: Magnified view of the magnetic field distribution given in Figure 4.20: simulation done using two magnets.

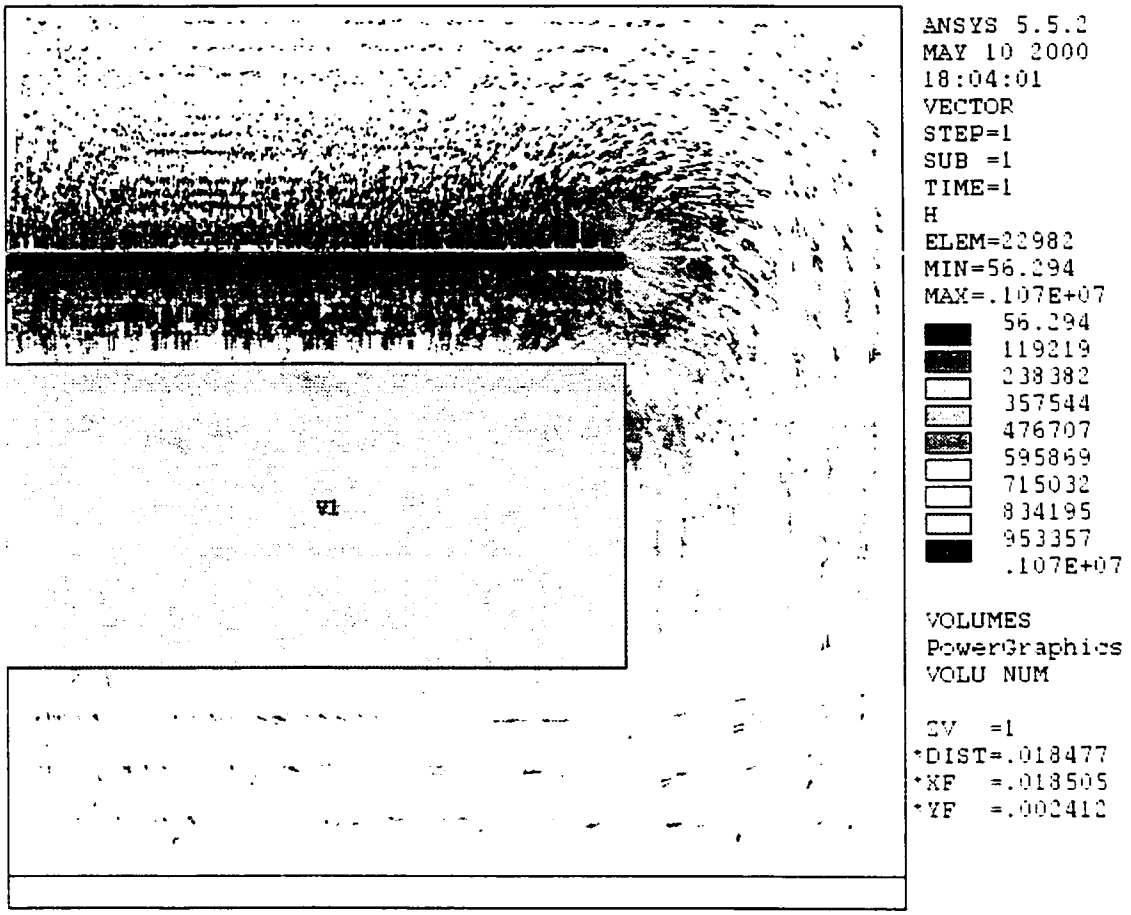

Figure 4.22: Magnetic field distribution with the ferrite substrate placed closer to the magnet: simulation done using one magnet.

To better improve the measurements, a logical conclusion would be to place the ferrite substrate closer to the biasing source. In this manner, the fringing fields could be avoided. However, Figure 4.22 shows that this conclusion is incorrect. In the figure, the magnetic field leaving the top of the substrate is very small meaning that most of the field escapes through the sides of the substrate. In order for the field to be truly uniform, the ferrite would have to be placed at an extremely small distance from the magnet, which is an impractical situation.

The previous figures have shown the limitations of placing the ferrite substrate in proximity to the magnet(s). Although this is important, the size of the substrate in

relation to the biasing source is important also. The employed ferrite substrate had width and length dimensions approximately the same as those of the magnets. With this size of substrate, no matter how close the ferrite is placed near the magnet(s), some fringing will exist. To counteract this, it would be necessary to make the ferrite width and length dimensions smaller than the biasing magnet.This would reduce the fringing fields tremendously.

To completely bypass the problems of magnetic fringing field effects, another biasing configuration could be considered. This would involve placing the substrate in between two magnets. Figure 4.23 shows this setup and it is apparent that there is little fringing from the fields near the ferrite substrate terminations. However, looking at the magnitude of the ferrite internal field in Figure 4.23, a small field value is shown. This is because the ferrite substrate dimensions were large, and the magnets have to be placed at a large distance away from each other (decreasing the field strength in between the magnets). This could be counteracted by using a smaller ferrite sample with a smaller separation distance between the magnets, or using stronger magnets.

After determining the actual H_i, within the ferrite substrate, the simulations were redone to recompute β_{eff}. Figure 4.24 shows the new simulation parameters for the CPW TL. The values used for the magnetic field intensities and the nonuniformity were those extracted from the static analysis simulation of Figure 4.21. Near the center of the ferrite substrate, Figure 4.21 shows a value of 139 Oe for H_i. Due to convergence difficulties, the lowest simulation value used for H_i, near the center of the ferrite substrate, was 500 Oe.

Figure 4.25 shows the β_{eff} comparisons with the modified simulation parameters. Clearly, the agreement shown in Figure 4.25 between the computed and measured propagation constant values is much better, indicating the importance in modeling the nonuniform field.. To improve the comparison, a more detailed model of Γ can

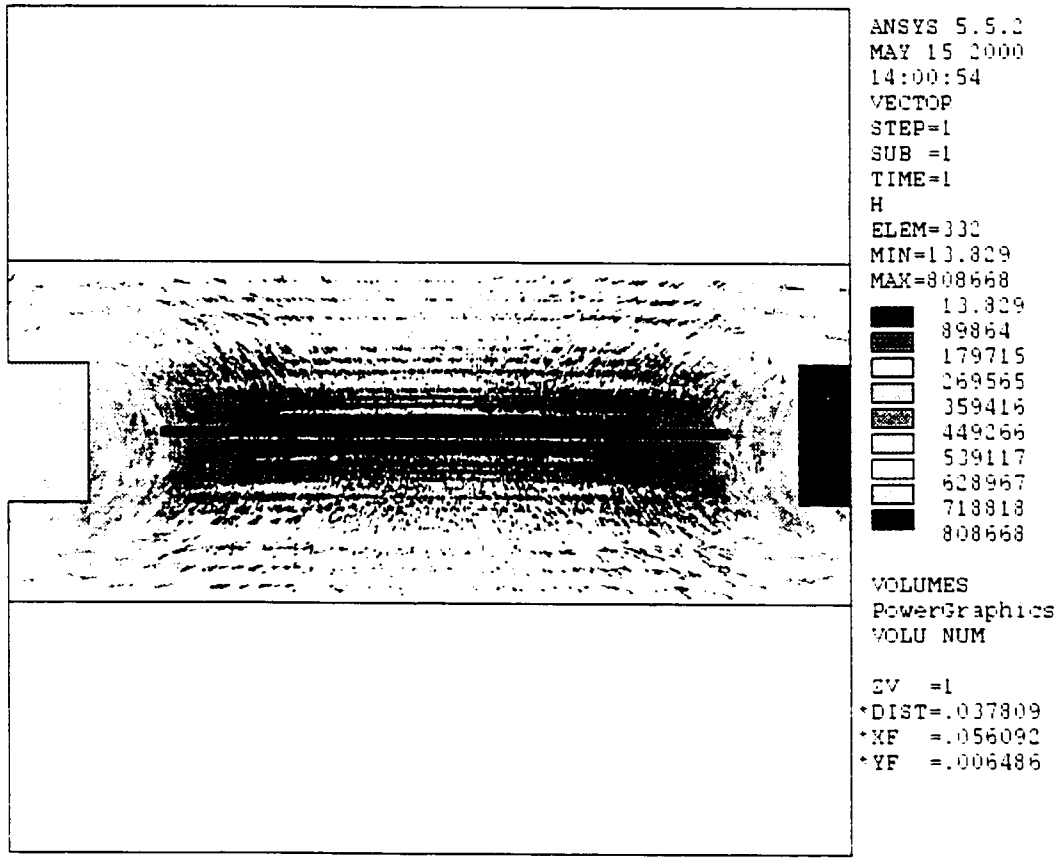

Figure 4.23: Alternative biasing configuration.

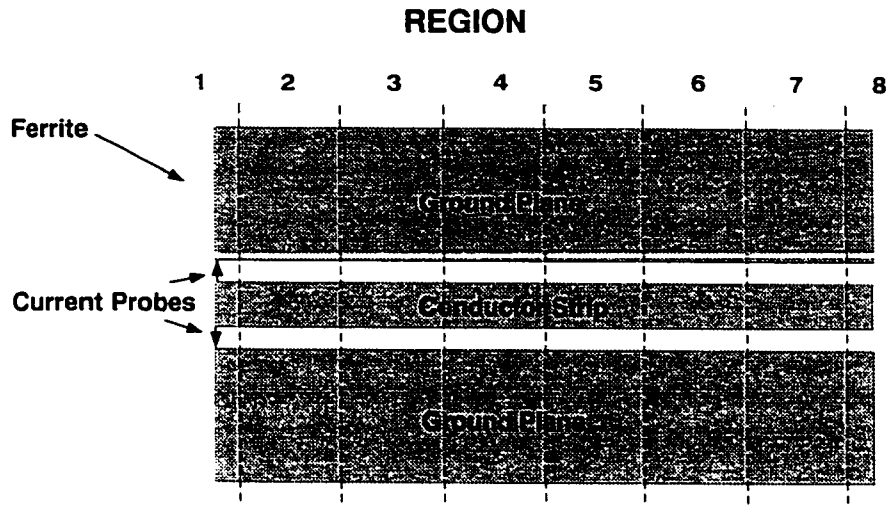

Hint=Ho($\hat{z}$ cos(θ) + $\hat{y}$ sin(θ))

	1	2	3	4	5	6	7	8
Hint (Oe)	**1090**	**2040**	**1090**	**500**	**500**	**1090**	**2040**	**1090**
θ	θ(1)	θ(2)	θ(3)	θ(4)	θ(5)	θ(6)	θ(7)	θ(8)

Figure 4.24: Illustration of the modified $H_{internal}$ for the CPW TL simulations.

be used. Figure 4.26 illustrates the TL model for an improved evaluation of Γ (and β_{eff}). Using this model, Γ can be determined from the following expression.

$$\Gamma = \Gamma_1 + T_1 T_s e^{-j\beta 2l} + T_1 T_s \sum_{n=1}^{\infty} \Gamma_s^n e^{-j\beta(n-1)2l} \tag{4.23}$$

which in contrast to the earlier model, includes multiple interactions between the two ports. Here, $\Gamma_1 = \frac{Z_{ocpw} - Z_{in}}{Z_{ocpw} - Z_{in}}$, $\Gamma_s = -\Gamma_1 =$, $T_1 = \frac{2Z_{ocpw}}{Z_{ocpw} - Z_{in}}$, and $T_1 = \frac{2Z_{in}}{Z_{ocpw} - Z_{in}}$. As seen from Figure 4.25, this improved TL model does show some improvement but this improvement is not sufficient to make-up the differences between measurement and calculation. Given the importance of nonuniformity, the differences are likely due to dimension and model inaccuracies.

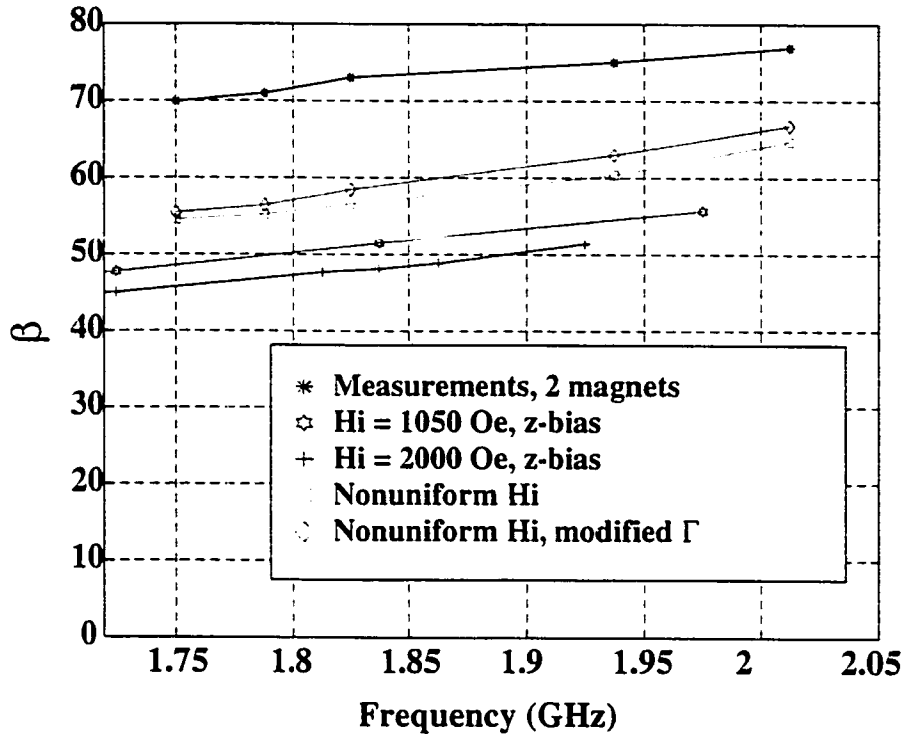

Figure 4.25: Measured and calculated propagation constant. Calculations were carried out using the nonuniform bias field distribution, illustrated in Figure 4.24.

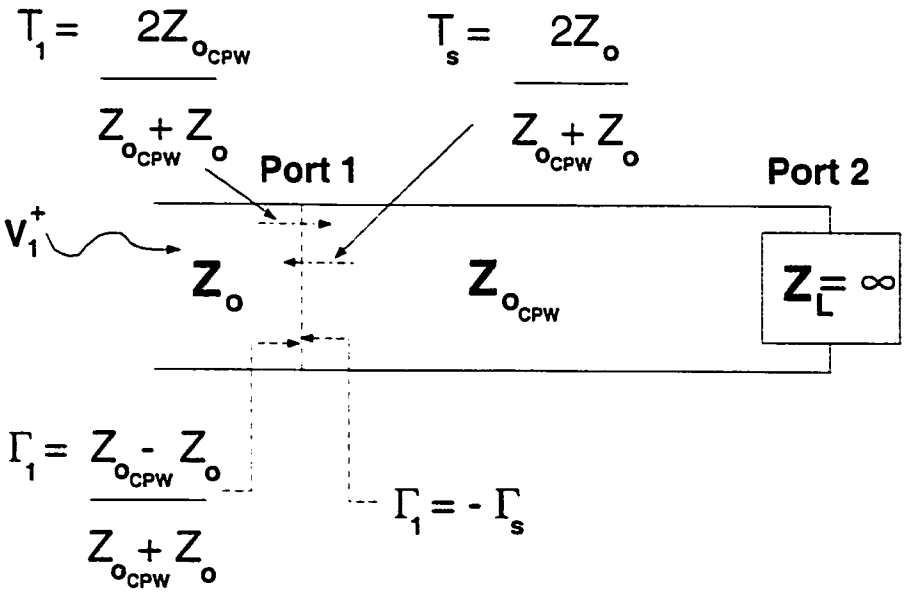

Figure 4.26: Improved TL model for extracting the reflection coefficient at port 1.

4.3 Summary

A CPW TL was built and measured to validate the extraction of the propagation constant using the FEM. Several comparisons were shown between the experimental and numerical data for the propagation constant within the ferrite medium. The initial comparison showed poor agreement, and this was attributed to the bias field nonuniformity. Therefore, a static analysis was necessary to determine the magnetic field distribution internal to the ferrite substrate. The analysis showed that $H_{internal}$ was nonuniform and also that the bias was not uniform in the z-direction. A final comparison between the measurements and simulations using the nonuniform H_i, showed substantially better agreement between the measured and calculated β_{eff}. Such an improved agreement demonstrates the importance of using the actual nonuniform bias field rather than it's average value. It is clear that the differences due to the uniform and nonuniform fields are quite important and must therefore be included for applications where the field is nonuniform.

CHAPTER V

MICROSTRIP FERRITE ARRAY PHASE SHIFTING

This chapter discusses array phase shifting using ferromagnetic materials. A method is proposed to determine the optimal values of the bias field (H_o) to achieve maximum array beam steering.

5.1 Background

Ferromagnetic materials have characteristics which make them attractive for antenna array applications. Due to their frequency dependent nature, ferrites can be used for array beam steering. The use of ferrites for phase shifting in waveguides and waveguide antennas has been investigated and well documented. [8, 26, 31, 38, 47, 51, 61, 65, 67]. Because ferrites exhibit good performance for waveguide antennas, their consideration in microstrip patch arrays is also of interest. Specifically, it is important to assess how the ferrite and the bias field should be configured (within the microstrip substrate) to achieve element by element phase control.

In general, beam steering is accomplished by mechanical or electronic scanning technology which can be costly and cumbersome [33]. However, the same type of beam steering capability can be achieved using ferrites, by simply changing H_o. Vary-

ing H_o provides steering for a range of scan angles. It has already been shown that steering can be accomplished by biasing the entire substrate on which the radiating antenna element resides [32, 33]. The analysis of infinite arrays on ferrite substrates [13, 52, 83] has also highlighted beam steering utilizing frequency agile ferromagnetic substrates. Another approach is to only place the ferromagnetic material underneath the feed lines [69]. Using this technique scan angles up to 40^o have been reported [5].

Although results have been presented which demonstrate beam steering capability, no consideration has been given on design issues determining what H_o values provide significant steering. In this chapter, the connection between the propagation constant in the ferrite substrate and the bias field is identified. This is done by isolating the ferrite feed line and determining the effective substrate wavelength (λ_{eff}) in the ferrite for different H_o values. With knowledge of λ_{eff}, β_{eff} can be calculated to determine the appropriate values of H_o to achieve maximum phase shifting.

5.2 Theory

For microstrip arrays, the phase along each feed line associated with each individual element must be controlled to achieve beam steering.. As mentioned in section 5.1, phasing for ferromagnetic microstrip arrays can be controlled in two ways: 1) placing the ferrite underneath the entire antenna structure including the feed [32], [33], or 2) placing the ferrite only underneath the microstrip feeds [5]. From a practical standpoint, the first method is perhaps better since it is easier to fabricate a structure with a uniform substrate. Unfortunately, due to losses inherent with ferrite materials, the antenna array is not as efficient as compared to an array on a dielectric substrate. From an efficiency viewpoint, the second method is therefore more optimal since only a portion of the feed lines is printed on ferromagnetic material, whereas the actual array elements reside on a dielectric substrate (see Figure 5.1).

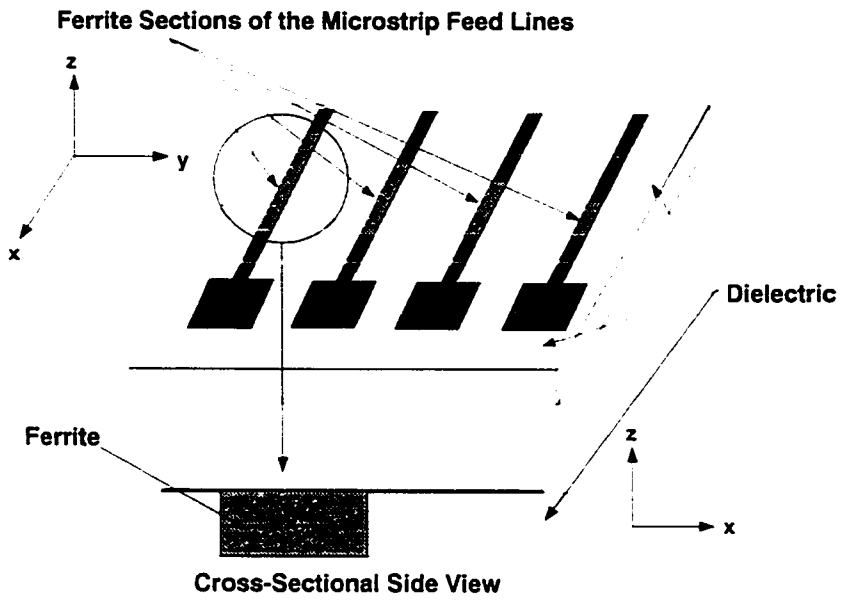

Figure 5.1: Ferrite antenna array employing microstrip ferrite phase shifters.

Figure 5.1 shows a simple ferrite array composed of rectangular microstrip patch elements, in which the ferrite substrate is placed underneath a section of the microstrip feed lines. The individual ferrite feed lines serve as phase shifters for the entire array. In Figure 5.1, it is important to note that each line has a different length of ferrite substrate beneath it. Thus, by changing the propagation constant with the ferrite, each element has a different phase at it's feed. This is done by controlling the external bias field and for this analysis a z-directed bias is assumed.

For ferrite arrays, a bias perpendicular to the radiating elements is desired (z bias for the geometry of Figure 5.1). This is because the phase constant exhibits a resonant behavior for the mode produced by the transverse bias. This is demonstrated in Figure 5.2, where it is observed that between 6.5 and 7.5 GHz, the propagation constant exhibits rapid variations. To obtain beam steering it is necessary to operate the antenna in this frequency range.

To determine optimal steering, it is necessary to compute β_{eff} in the ferrite region of the microstrip feed lines as a function of H_o. This can be done by analyzing a

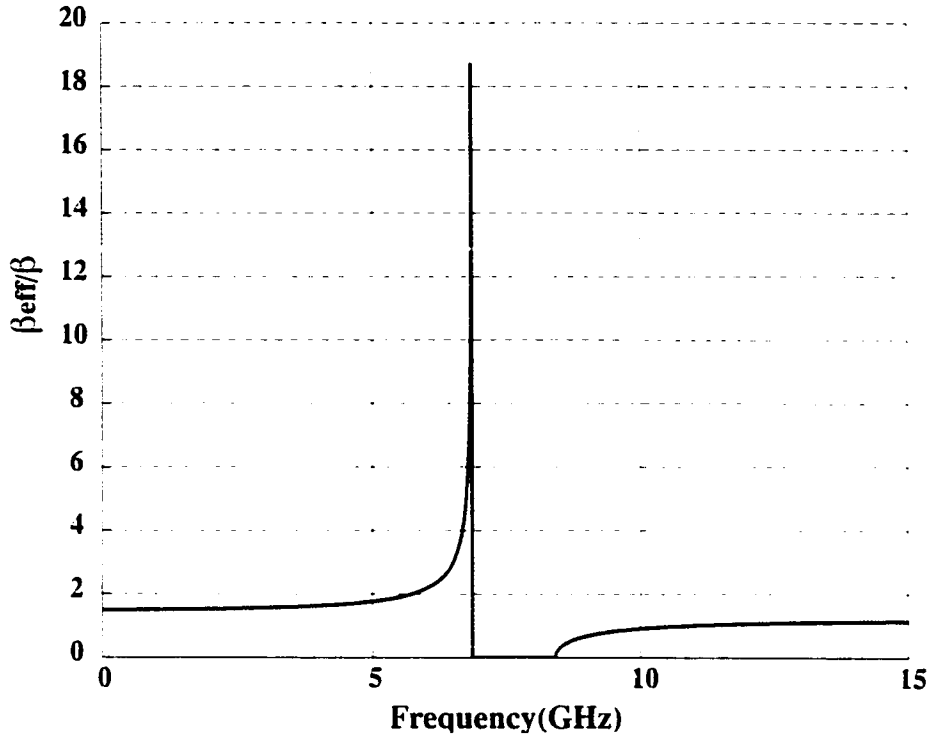

Figure 5.2: β vs. frequency behavior for arbitrary H_o in the transverse biasing mode.

single section of the ferrite microstrip line. Consider a single microstrip line fed by a vertical probe. The line is terminated at an open circuit, which produces a standing wave along the TL.

When the substrate is unbiased and unmagnetized ($H_o = 0$ and $4\pi M_s = 0$), the ferrite material simply acts as a regular dielectric. The propagation constant underneath the microstrip line is then given by

$$\beta = \frac{\omega}{c}\sqrt{\epsilon_{r_{eff}}\mu_r} \tag{5.1}$$

where $\mu_r = 1$. For the biased and magnetized substrate, the substrate acts as a ferrite and μ_r no longer equals unity. This means that β_{eff} must be introduced to account for the new effective permeability ($\mu_{r_{eff}}$). By looking at the value of β_{ratio} ($\beta_{ratio} = \frac{\beta_{eff}}{\beta}$), it is clear that for any appreciable phase change along the line, β_{ratio}

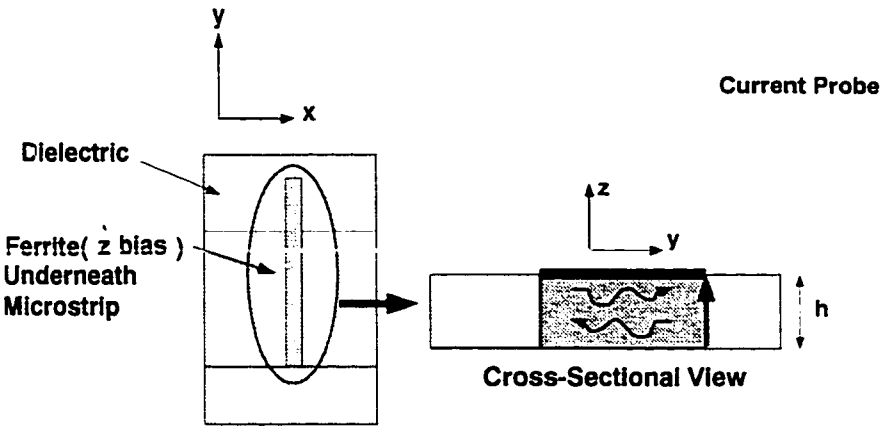

Figure 5.3: Ferrite microstrip feed line.

must be greater than unity. Observing the behavior of β_{ratio} versus frequency for different values of H_o determines which values of H_o will produce the largest amount of phase change.

To obtain a better understanding of β_{ratio}, it is beneficial to first think of the ferrite line section as a bulk ferrite. For a bias field applied transverse to the direction of propagation (which is the case presented here) in a bulk ferrite, $\mu_{r_{eff}}$ is found using Equation 3.3. Figure 5.4 shows a plot of β_{ratio} versus frequency for different values of H_o for a bulk ferrite. It is apparent that for the bias values shown, H_o = 680 Oe would produce the most phase shift because β has the largest value for the given frequency range.

For the actual biased configuration, (3.3) is no longer correct due to fringing fields under the microstrip line (see previous chapter). Therefore, the fields underneath the line were numerically computed and λ_{eff} was determined. Using the relation

$$\beta_{eff} = \frac{2\pi}{\lambda_{eff}}. \tag{5.2}$$

β_{ratio} was then found to determine which values produced the greatest phase shift.

Figures 5.5 - 5.7 show the standing wave pattern underneath the microstrip line

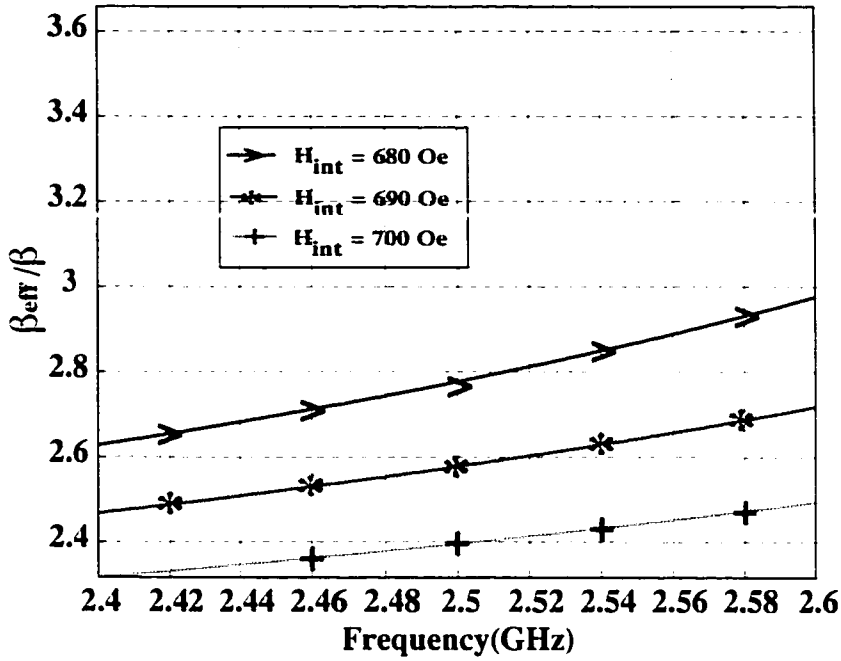

Figure 5.4: β_{ratio} vs. frequency for different H_o values, for field propagation within a bulk ferrite.

depicted in Figure 5.3. For each of these plots, λ_{eff} was computed using simple TL theory. From the plots, it is apparent that as the frequency increases and the bias is kept constant, λ_{eff} becomes smaller as expected. Of importance, is that λ_{eff} changes from it's isotropic (no bias) value as H_o is varied. This property allows ferrites to be used for array phasing. Figure 5.8 shows the fields ($\mathbf{E_z}$) on the surface of the modeled microstrip TL, and as expected these depict the standing wave pattern on the terminated line.

5.3 Results

5.3.1 Array Example

In the previous section, a method for determining optimum values for the applied magnetic field was shown. These values for H_o can be used for beam steering. To

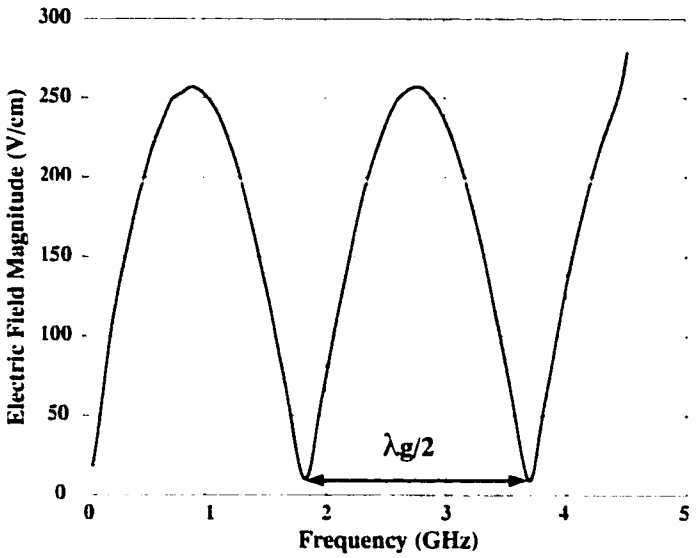

Figure 5.5: Standing wave pattern along the unbiased feed line ($4\pi M_s = 0$ G) shown in Figure 5.3 for $f = 2.5$ GHz.

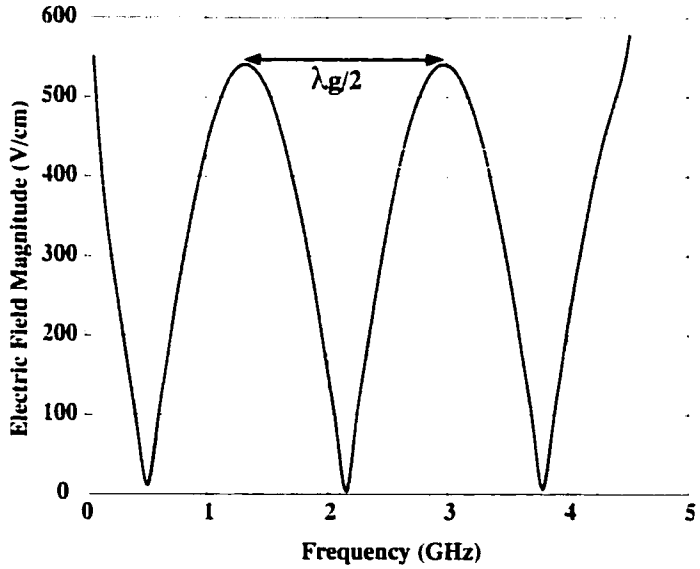

Figure 5.6: Standing wave pattern along the biased feed line ($4\pi M_s = 1000$ G and $H_o = 2000$ Oe) shown in Figure 5.3 for $f = 2.5$ GHz.

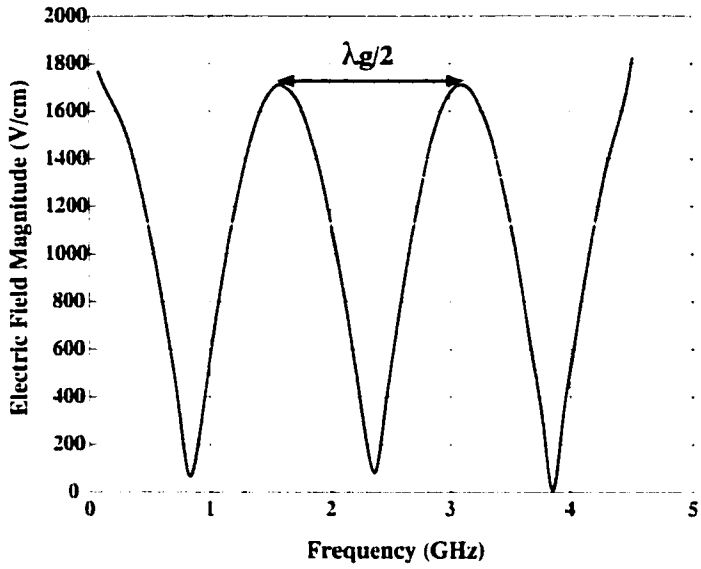

Figure 5.7: Standing wave pattern along the biased feed line ($4\pi M_s$ = 1000 G and H_o = 2000 Oe) shown in Figure 5.3 for f = 2.7 GHz.

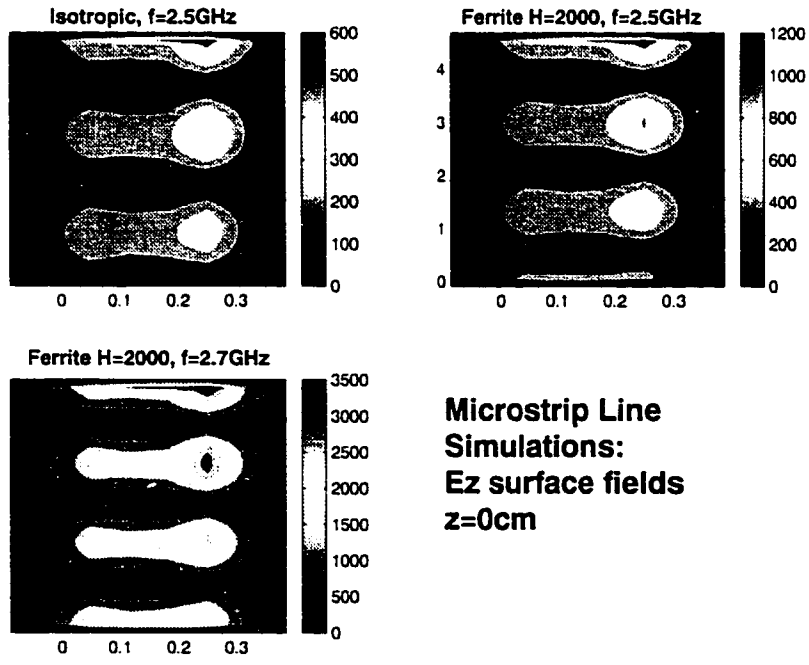

Figure 5.8: E_z component of the electric field on the surface of the modeled microstrip TL in Figure 5.3.

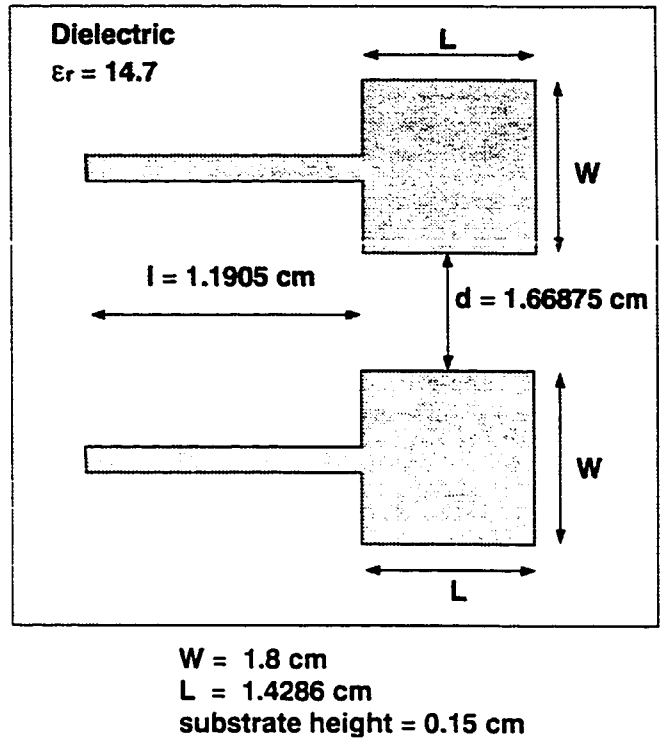

Figure 5.9: 2x1 microstrip array.

demonstrate this, a simple 2x1 array of rectangular microstrip patches was considered. The geometry is shown in Figure 5.9. The individual patches were designed to resonate near 2.5 GHz and were placed on a substrate having $\epsilon_r = 14.7$. This dielectric constant was selected to reduce the impedance mismatch at the junction between the biased and the unbiased portion of the microstrip line. In reality, the patches would be designed using a dielectric with a lower ϵ_r. Appropriate matching techniques would then be necessary to reduce impedance mismatch losses. Since the aim of this work was to primarily observe the beam steering capabilities of the ferrite array, a simplified model was designed for numerical simulation.

Figures 5.10 and 5.11 show the radiation characteristics for a single patch and the 2x1 array without the microstrip feeds. In accordance with the design paramaters, both resonate near 2.5GHz. With the addition of the biased feed lines, a change in the radiation pattern will occur. The degree of change will depend on the H_o values

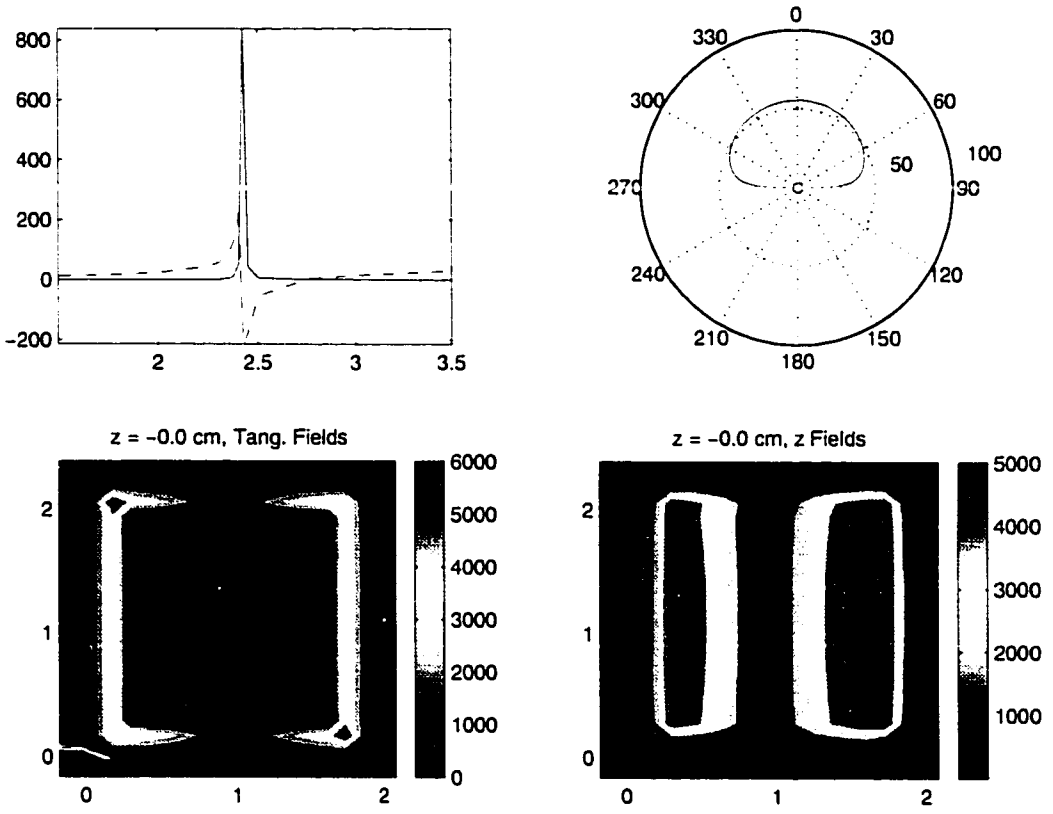

Figure 5.10: Input impedace, radiation pattern, surface tangential electric fields and surface z component electric fields for the single element design microstrip patch.

chosen to bias the lines.

Figure 5.12 shows the geometry of the designed array with ferrite microstrip feed lines and denotes the regions on the microstrip line which include ferrite material. For this configuraton, Figure 5.14 shows the variance in the radiation pattern as the applied magnetic field bias is changed. It is seen that as the bias field is decreased, the main lobe of the radiation pattern is shifted. This is to be expected since at 2.5 GHz, $\mathcal{Z}_{eff}$ is largest at $H_o = 680$ Oe as shown in Figure 5.13. This shows that for a microstrip array which employs ferrite feed lines, the optimal H_o value for steering can be determined. Figure 5.15 shows the amount of beam steering versus H_o. From

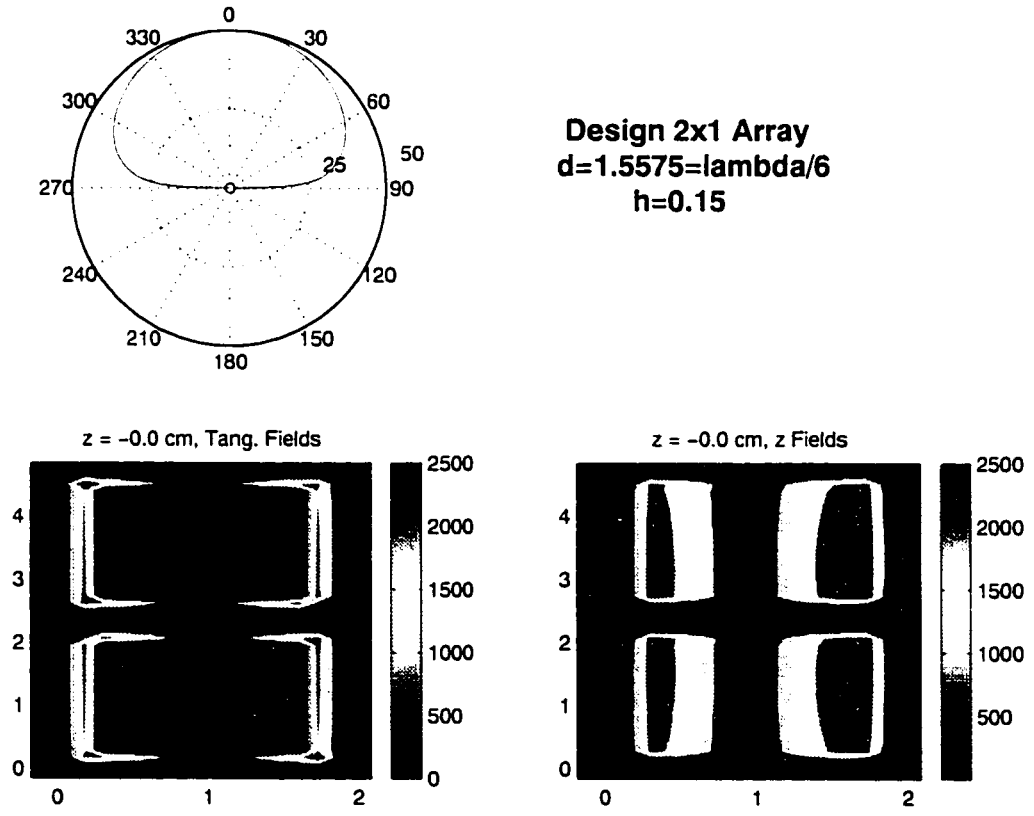

Figure 5.11: Radiation pattern, surface tangential electric fields and surface z-component electric fields for the 2x1 design microstrip array.

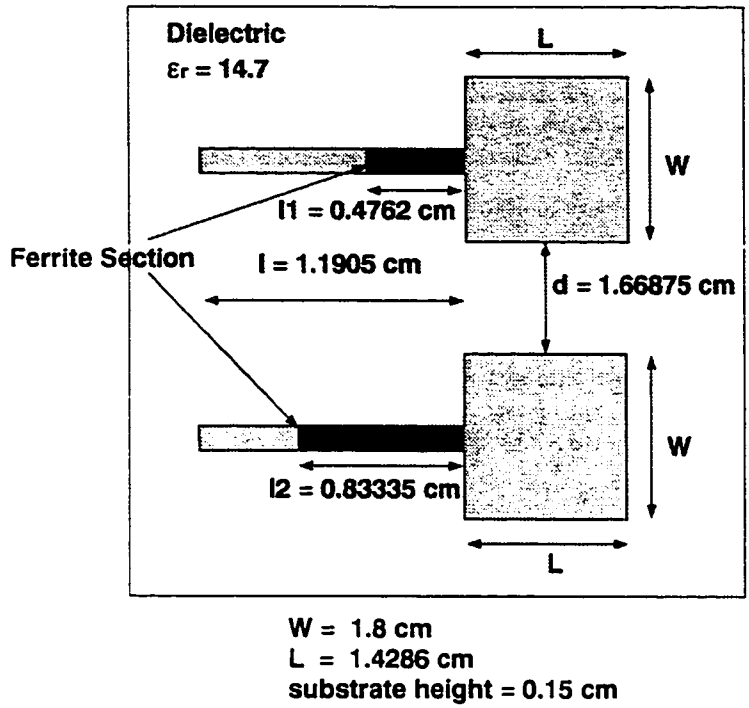

Figure 5.12: Array geometry with ferrite biased feed lines.

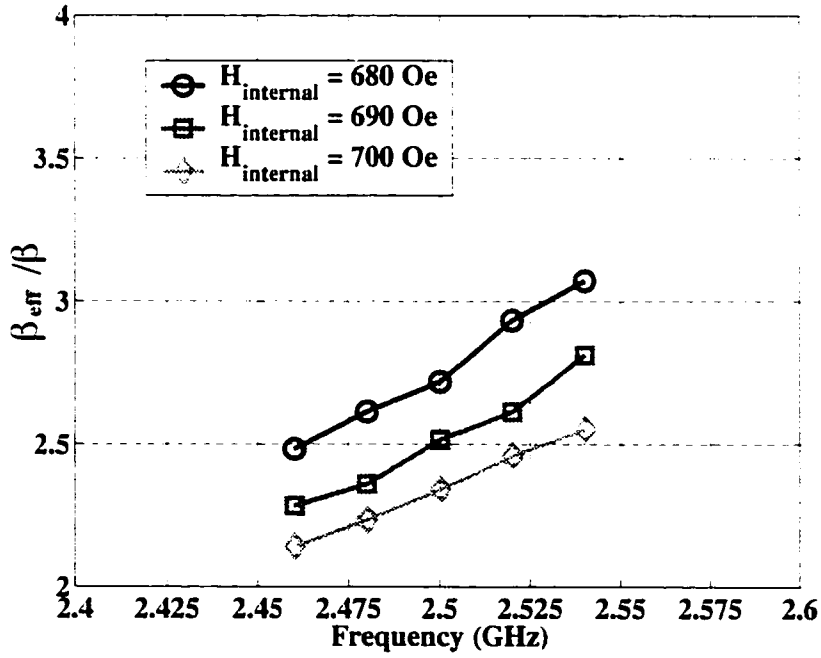

Figure 5.13: β_{ratio} vs. frequency for different H_o values. for the ferrite sections of the microstrip feed lines of the 2x1 array shown in Figure 5.12.

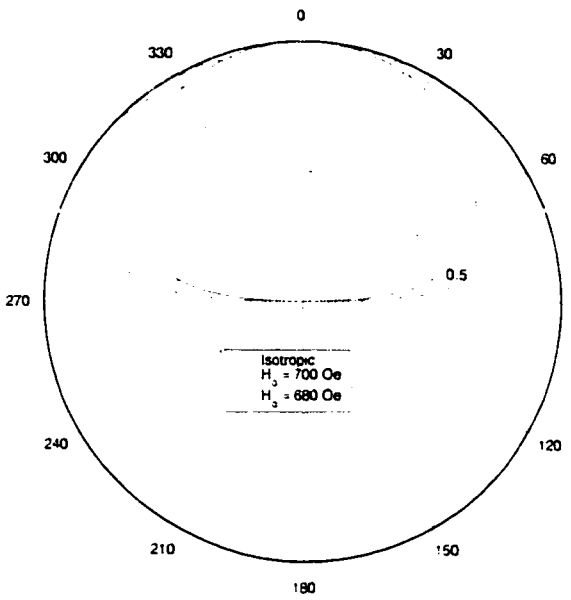

Figure 5.14: Normalized beam steering radiation patterns for the ferrite array shown in Figure 5.12.

the graph, a scan angle of 35° is observed. However, because of the wide beam angle of the radiation pattern (only 2 elements used) beam steering is not as pronounced

.

To better demonstrate the beam steering effect, the element spacing was increased to produce a more directive pattern. The geometry is shown in Figure 5.16. Figure 5.17 and 5.18 show the beam steering as a function of H_o and corresponds to the situation that may be typically implemented. Figure 5.19 depicts $\mathcal{J}_{ratio}$ for the H_o values plotted in Figures 5.17 and 5.18. Similar to the previous example, the maximum amount of beam steer occurs around the frequency region where $\mathcal{J}_{eff}$ is maximum.

Next an array of the 2x1 element in Figure 5.16 was considered. Figure 5.21 shows the beam steering for an array of fourteen 2 x 1 elements aligned along the y-axis separated by a distance $d = \frac{\lambda}{1.7}$ (see Figure 5.20). Because of the narrower

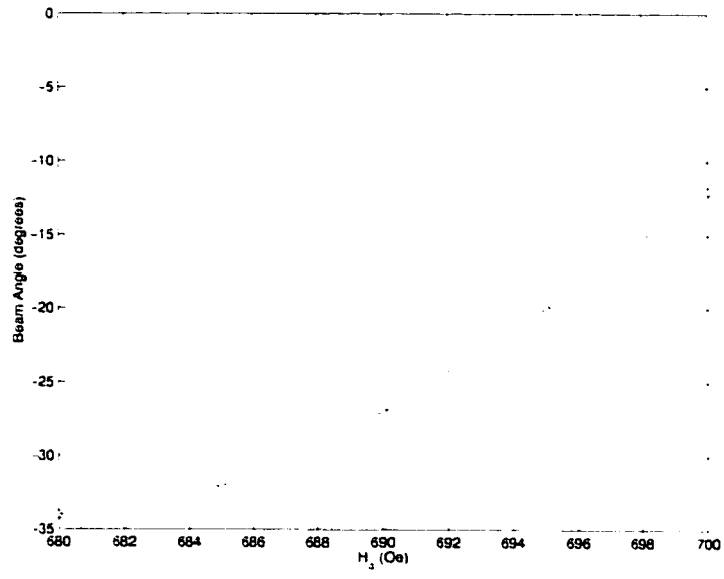

Figure 5.15: Scan angle vs. H_o for the ferrite array shown in Figure 5.12.

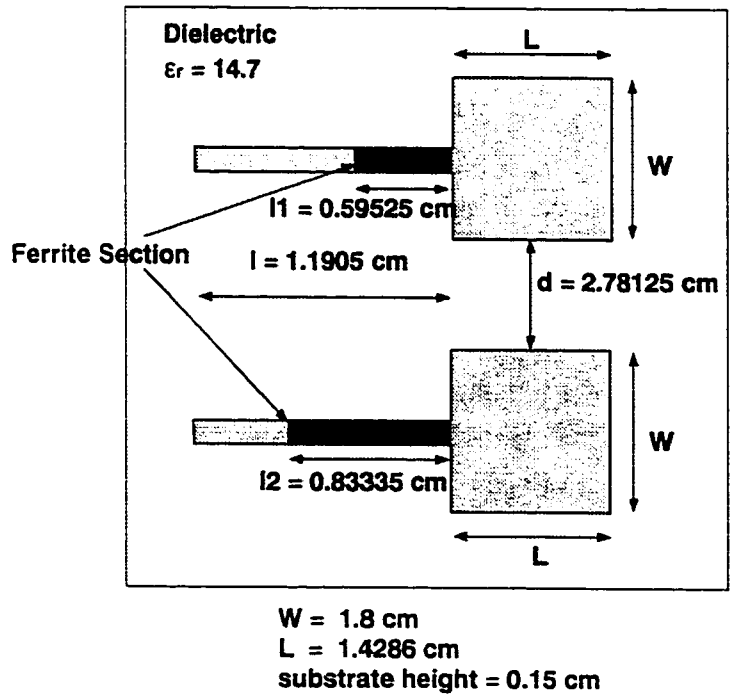

Figure 5.16: Array geometry with ferrite biased feed lines and increased element spacing (d).

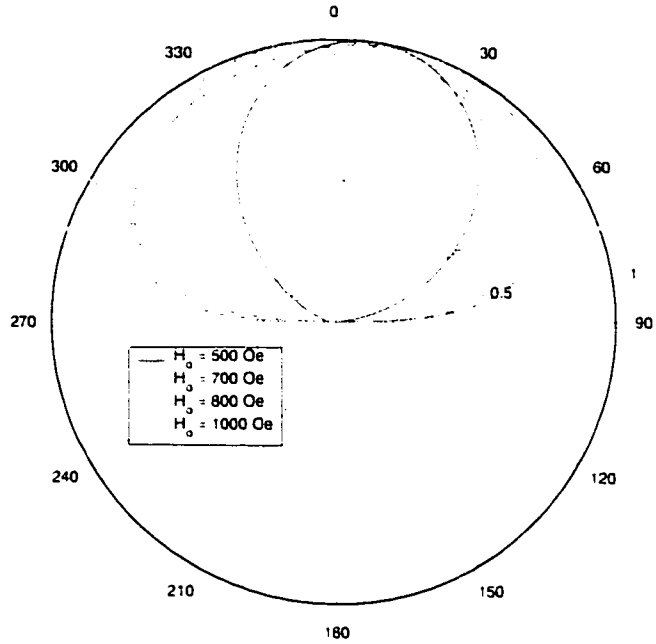

Figure 5.17: Normalized beam steering radiation patterns for the 2 x 1 array in Figure 5.16.

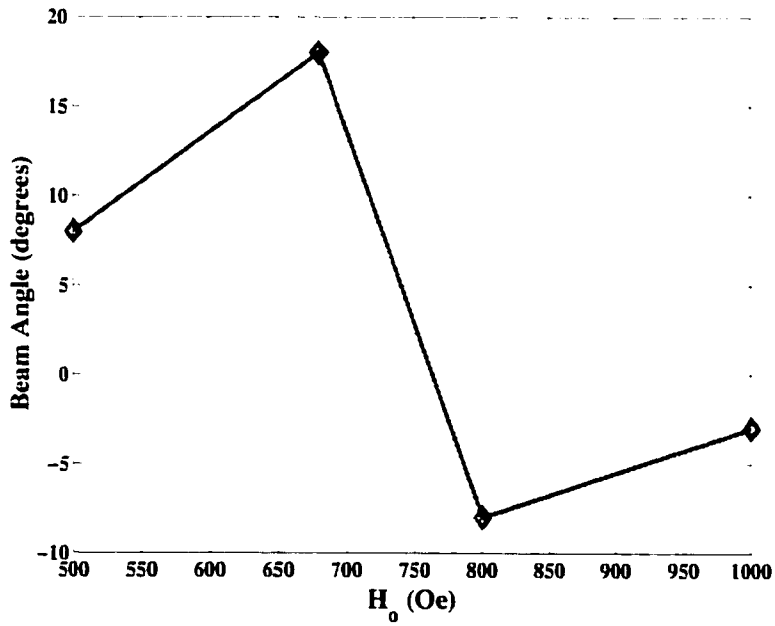

Figure 5.18: Scan angle vs. H_o for the 14 element array show in Figure 5.16.

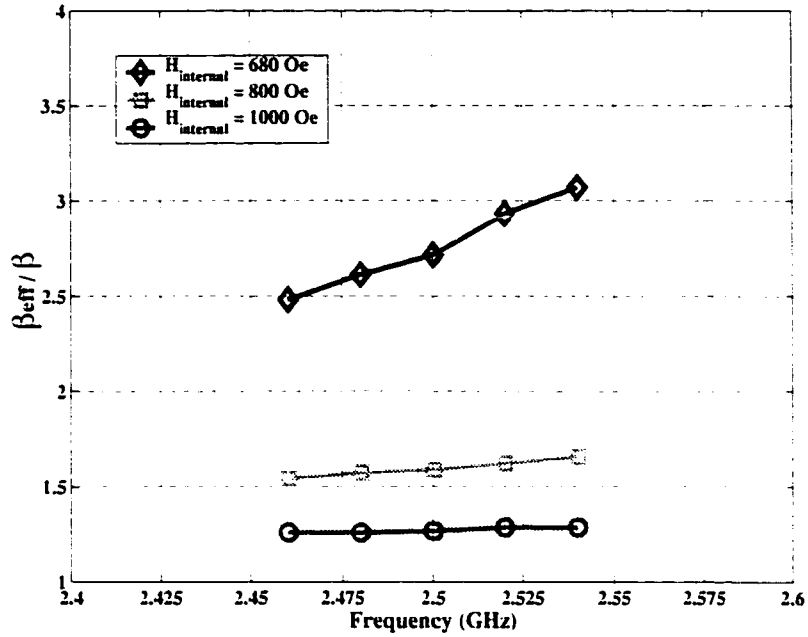

Figure 5.19: β_{ratio} vs. frequency for different H_o values, for the ferrite sections of the microstrip feed lines of Figure 5.16.

beamwidth, the beam steering is more pronounced in the radiation pattern of Figure 5.21. These examples demonstrate that optimal values of H_o for beam steering correspond to the case where β_{eff} is maximum. β_{eff} can then be used to design microstrip arrays using ferrite phase shifters for maximum beam steering.

5.3.2 Impedance Transformation

Another interesting application of the ferrite feed line, is it's use as an impedance transformer. As shown in Figure 5.22, for H_o = 680 Oe, the radiated field is 10 dB higher at the pattern maximum due to the improved match between the ferrite line and the dielectric patch.. In essence, a ferrite microstrip feed could also be used to match the line to the antenna, thus acting as an impedance transformer. The impedance of the ferrite microstrip transformer would be controlled by varying the applied bias field. This would lead to a reduction in the impedance mismatach

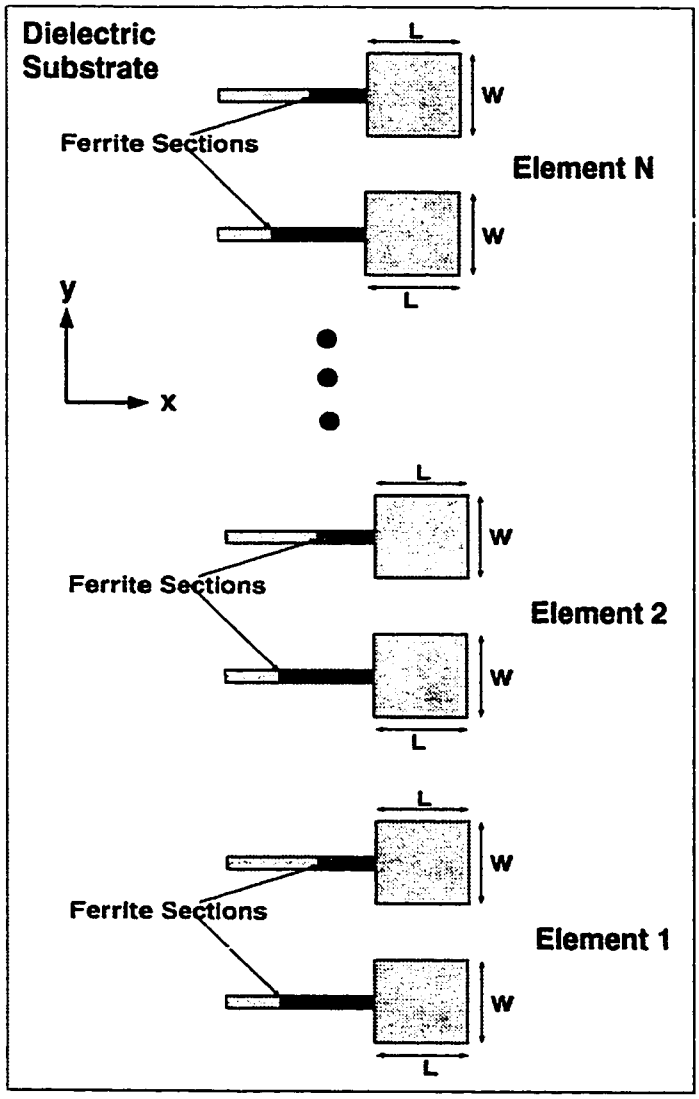

Figure 5.20: Geometry for the array of 2 x 1 elements (Figure 5.16) with $N = 14$.

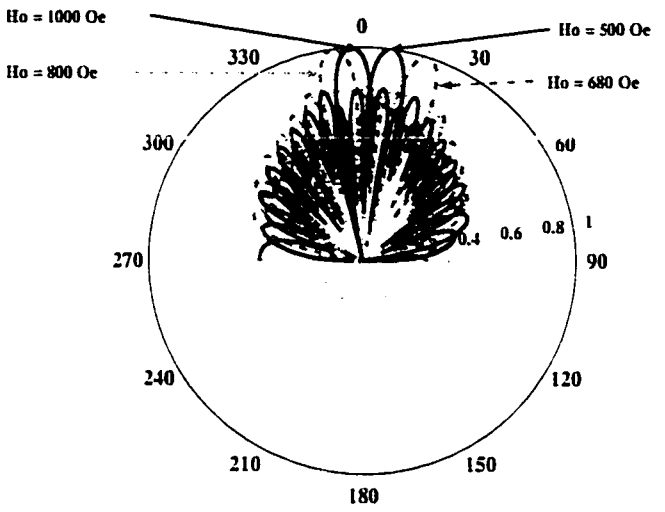

Figure 5.21: Normalized beam steering radiation patterns for an array consisting of 14 elements of the 2 x 1 configuration in Figure 5.16.

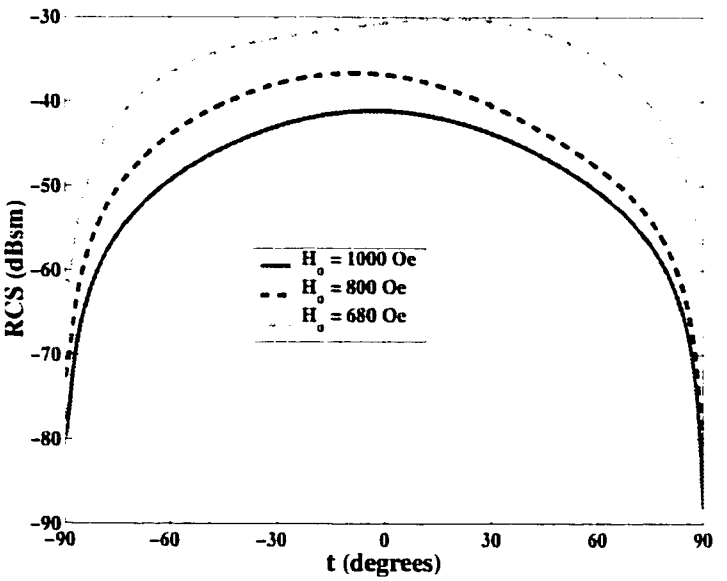

Figure 5.22: Radiation patterns for different biasing values.

thereby improving the antenna efficiency.

5.4 Summary

In this chapter, phase characteristics of ferrite substrates were presented and it was demonstrated that different bias fields allow for beam steering. It was also shown that the effective propagation constant plays a significant role in determining what values of H_o will result in beam steering. Basically, values of H_o can be determined that will result in optimum beam steering performance. It was also shown that ferrite lines acts similar to impedance transformers and can be used to improve antenna efficiency by adjusting the bias field to achieve impedance matching.

CHAPTER VI

TEMPERATURE EFFECTS ON FERROMAGNETIC PATCH ANTENNAS

This chapter explores the effects of temperature on the performance of ferrite loaded microstrip antennas.

6.1 Motivation

When analyzing ferrite materials for practical applications, temperature effects must be considered. Because the magnetization properties of any ferromagnetic material are highly dependent on temperature, the performance of ferrite devices are also expected to be temperature sensitive. Therefore, it is necessary to determine how a microwave ferrite device operates with fluctuations in temperature.

For microwave integrated circuits, ferrites have been used extensively [58], and issues related to temperature stabilization have been investigated [3, 37] for these devices. Ferrite materials that are less temperature senstive have been developed [37], and substrates that combine *nonmagnetic* ferrites with normal ferrites [29] have been considered. The nonmagnetic or substituted ferrite regions possess a Curie temperature below room temperature, implying that at room temperature they act like a

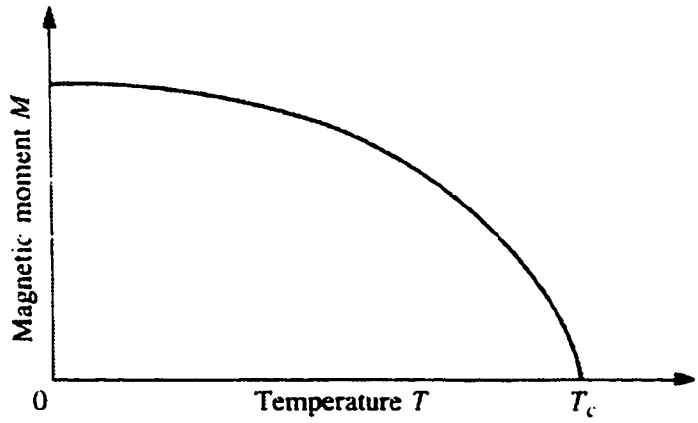

Figure 6.1: Effect of temperature on ferrite magnetization.

pure nonmagnetized dielectric.

Currently, there is no literature on how the temperature effects the performance of loaded antennas. In the case of microstrip antennas, currents generated on the radiating PEC surfaces dissipate power into the substrate to effectively raise the substrate temperature. As the temperature increases, the magnetization of the ferrite substrate decreases thereby changing the resonant properties of the antenna when biased. This chapter presents an analysis, of the temperature variations resulting from currents generated on the PEC portions of a microstrip antenna.

6.2 Theory

6.2.1 Relationship Between Temperature and Saturation Magnetization

As mentioned previously, ferromagnetic materials are inherently temperature sensitive. This is because the intrinsic magnetization of all ferromagnetic materials is a function of temperature. When an external bias field is applied to a ferrite material, the ferrite becomes magnetically saturated. However, the saturation level is dependent on the ferrite temperature. For example, Table 6.1 shows the saturation magnetization for some metals under different ambient temperatures [9].

Saturation Magnetization (G)		
Metal	$4\pi M_s$ $T = 0^oK$	$4\pi M_s$ $T = 293.15^oK$
Iron	2.2×10^4	2.15×10^4
Cobalt	1.82×10^4	1.76×10^4
Nickel	0.641×10^4	0.609×10^4

Table 6.1: Typical $4\pi M_s$ values for several ferromagnetic metals.

Curie Temperature (^oK)	
Iron	1043
Cobalt	1400
Nickel	631

Table 6.2: Curie temperature values for several ferromagnetic metals.

An interesting phenomenon occurs when the temperature of the ferrite is increased beyond the saturation magnetization temperature. In this case the net magnetization of the material begins to *decrease* (see Figure 6.1). Eventually, at a certain temperature, the net magnetization becomes zero, and the temperature at which this occurs is referred to as the magnetic change point or the Curie temperature (T_c) [9]. Figure 6.1 illustrates the effect of T_c on a certain ferrite magnetization. Basically, at T_c the electrons are thermally agitated to such an extent, that the magnetization energy is unable to overcome the thermal energy, thus preventing the magnetic moments from aligning themselves with the external bias field. Table 6.2 shows the T_c values for the materials in Table 6.1.

The dependence of the saturation magnetization on temperature directly affects the performance of ferrite loaded microstrip antennas. The dissipated power from the antenna patch currents causes an increase in the temperature of the ferrite substrate, decreasing the saturation magnetization, and thereby changing the antenna resonant frequency. It is therefore of interest to carefully consider temperature effects. In the next section details are discussed for evaluating dissipative power and it's effect on temperature.

6.2.2 Heat Conduction

In general, there are three types of heat transfer:

1. conduction
2. radiation
3. convection.

Conduction and radiation occur in both solids and fluids while convection is the transfer of heat from a solid to a fluid [70]. Heat transfer in the form of conduction, as it occurs between the radiating patch and the ferrite substrate, is the primary mechanism of interest.

The general heat conduction equation is

$$\nabla \cdot \bar{\bar{k}} \cdot \nabla T + q''' = \rho c \frac{\partial T}{\partial \tau} \tag{6.1}$$

where $\bar{\bar{k}}$ is the thermal conductivity tensor of the medium, T is the temperature, q''' is the rate of energy generation at time τ per unit volume, ρ is the material density and c is the specific heat. For the analysis of the ferrite loaded antenna, several assumptions can be made to simplify (6.1). The ferrite material used for the antenna substrate is thermally isotropic, thereby reducing the thermal conductivity from a tensor to a scalar ($\bar{\bar{k}} \Longrightarrow k$). Furthermore, for a steady state solution, $\frac{\partial t}{\partial \tau} = 0$, which also simplifies (6.1). With these simplifications taken into account, (6.1) reduces to

$$\nabla^2 T = \frac{q'''}{k} \tag{6.2}$$

where $\frac{q'''}{k}$ is identified as the excitation source.

Before continuing with the analysis, a pictorial representation of the problem is shown in Figure 6.2. Figure 6.2 illustrates that the patch dissipates power into the

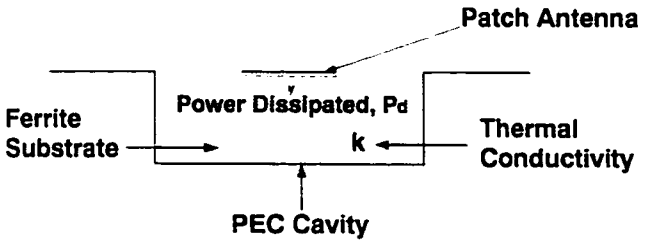

Figure 6.2: Illustration of heat conduction problem.

cavity, due to the conduction currents on the patch. Subsequently, the substrate temperature increases, with consequential effects on the ferrite's net magnetization as discussed previously.

6.2.3 Boundary Conditions

In order to solve 6.2 the following conditions are necessary [50]:

1. Initial conditions ($T(\mathbf{r}, 0)$)

2. Boundary conditions which specify temperature or heat flow ($\mathbf{q}$)

When these conditions are specified a unique solution for (6.2) can be found. Specifying the initial temperature is straightforward, but in order to determine the boundary conditions at the surface an energy balance equation must be used. At any arbitrary boundary, the following relation must hold [50]

$$\text{Heat supply} = \text{Heat loss}.$$

This is simply the first law of thermodynamics applied at a boundary which states that the amount of created energy is zero [70].

To solve the heat balance equation at a boundary, it is necessary to determine expressions for the heat supply and the heat loss. This is done by considering the heat fluxes produced by convection, radiation, and external heat supplies as illustrated in Figure 6.3 [50]. In Figure 6.3, the shaded surface area, with outward normal $\hat{\mathbf{n}}$,

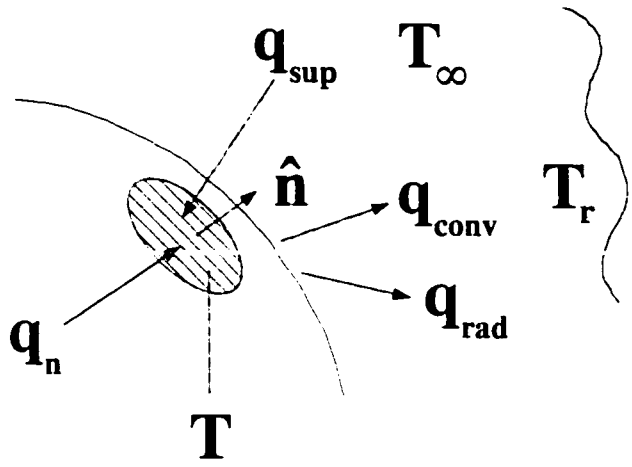

Figure 6.3: Different heat fluxes which can exist at an arbitrary boundary for a heat conduction problem.

is subjected to the various heat fluxes q_{sup}, q_{conv} and q_{rad}, where q_n is the normal component of the heat flux at the boundary. T_∞ and T_r are external ambient temperatures for q_{conv} and q_{rad}, respectively, and T is the boundary temperature. The quantity $q_{sup}[\frac{W}{m^2}]$ represents the energy supplied to the surface. The heat flux q_{conv} represents heat loss from the surface at temperature, T, by convection with a heat transfer coefficient, $h[\frac{W}{m^2 \cdot ^oC}]$, into an external ambient at temperature T_∞

$$q_{conv} = h(T - T_\infty)[\frac{W}{m^2}]. \tag{6.3}$$

The term q_{rad} corresponds to the heat loss from the surface by radiation into an ambient at an effective temperature T_r

$$q_{rad} = \epsilon\sigma(T^4 - T_r^4)[\frac{W}{m^2}] \tag{6.4}$$

where ϵ is the surface emissivity and σ is the Stefan-Boltzmann constant ($\sigma \equiv 5.6697 \times 10^{-8}[\frac{W}{m^2} \cdot K^{-4}]$). Finally, q_n can be represented as

$$q_n = -k\frac{\partial T}{\partial n}. \tag{6.5}$$

To determine the heat balance equation at the surface, the relation

$$\text{Heat supply} = \text{Heat loss}$$

can be expressed as

$$q_n + q_{sup} = q_{conv} + q_{rad}. \tag{6.6}$$

Substituting [6.3] - [6.5] into [6.6] the boundary condition reduces to

$$-k\frac{\partial T}{\partial n} + q_{sup} = h(T - T_\infty) + \epsilon\sigma(T^4 - T_r^4). \tag{6.7}$$

Equation 6.7 can then be used to solve (6.2) for any type of surface enclosing the volume domain.

6.3 Temperature Simulations

6.3.1 Simulation Model

To demonstrate the effects of temperature on antenna performance, the ferrite microstrip patch antenna geometry in [55] was used to conduct the analysis. Figure 6.4 shows the geometry. The ferrite substrate underneath the patch has an effective permeability of 15 and the saturation magnetization equals 650 G.

To conduct the temperature analysis, the surface electric fields on the patch, at the resonant frequency, must be determined. These fields determine the dissipated power density of the conducting patch. The FE-BI method was used to calculate

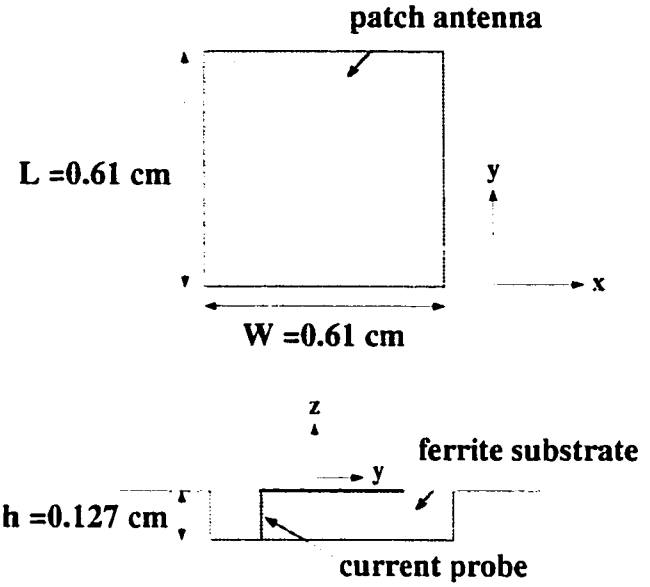

Figure 6.4: Ferrite microstrip patch geometry. W = L = 0.61 cm, h = 0.127 cm, ϵ_r = 15, $4\pi M_s$ = 650 G.

the surface electric field distribution. Figure 6.5 shows validation of the resonant frequencies computed in [55]. The values from [55] plotted in Figure 6.5 were produced using a cavity model.

A temperature increase in the ferrite substrate would correspondingly decrease the saturation magnetization, as mentioned in section 6.2. This would then shift the operating frequency of the antenna. Figure 6.6 shows how the resonance frequency of the patch in Figure 6.4 changes with decreasing magnetization for a fixed bias field. This effect would be undesirable for antenna applications where the radiating element is expected to operate at a given design frequency.

To determine the temperature distribution in the ferrite substrate, the ANSYS FEM software was used. The software employs a node-based formulation solving Equation 6.2 with user specified boundary conditions (discussed in section 6.2.3). Figure 6.7 shows a side view of the patch in Figure 6.4, with the appropriate boundary conditions. Initially, the patch and it's surroundings were assumed to be at room temperature ($20°C$). The volume domain (ferrite substrate) was enclosed by three

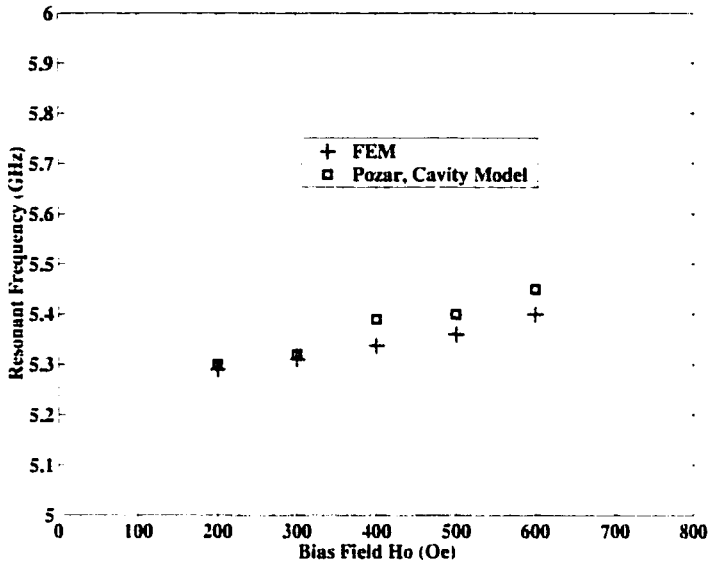

Figure 6.5: Validation of the resonant frequencies of the patch antenna in [56] as a function of the bias field H_o. $4\pi M_s = 650$ G.

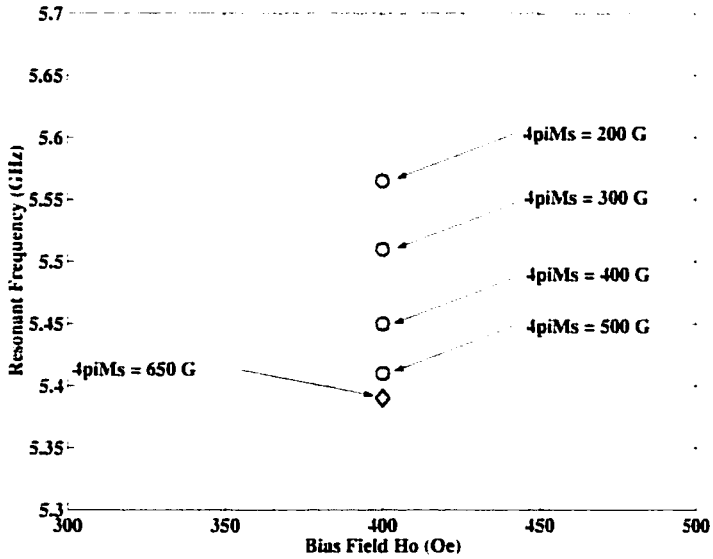

Figure 6.6: Resonant frequency of the patch antenna as a function of the saturation magnetization. $H_o = 400$ Oe.

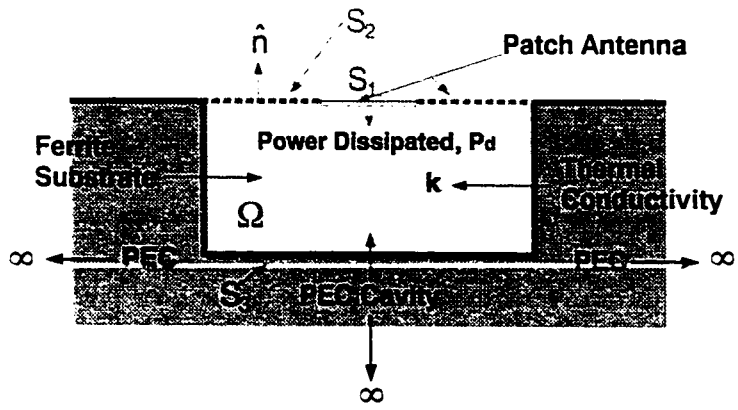

Boundary Conditions for S_i

$$S_1 : \hat{n} \cdot \vec{q} = \hat{n} \cdot (-k \nabla T) = k \cdot \frac{\partial T}{\partial n} = \frac{1}{2} \frac{|\vec{J}_s|^2}{\sigma \delta_s}$$

$$S_2 : \hat{n} \cdot \vec{q} = h (T_{bulk} - T_s)$$

$$S_3 : k_{PEC} \cdot \frac{\partial T_{PEC}}{\partial n} = h_c (T_{PEC} - T_{ferr}) = k_{ferr} \cdot \frac{\partial T_{ferr}}{\partial n}$$

Figure 6.7: Surface boundary conditions for the geometry of Fig 6.4

different types of boundaries which are denoted in Figure 6.7 as S_1, S_2 and S_3. Boundary S_1 has the following boundary condition [15]

$$q_n = q_{sup} = \frac{1}{2} \frac{|\mathbf{J}_s(\mathbf{E})|^2}{\sigma \delta_s} \tag{6.8}$$

where σ is the electrical conductivity of the metal patch, δ_s is the skin depth (see Figure 6.8), and $\mathbf{J}_s$ is the conductor surface current density. As denoted in (6.8), $\mathbf{J}_s$ is a function of the electric field (computed using the FE-BI method) on the surface of the patch.

For boundary S_2, the heat fluxes q_{sup} and q_{rad} in (6.6) are zero resulting in the following boundary condition for S_2

$$q_n = q_{conv} = h(T - T_\infty). \tag{6.9}$$

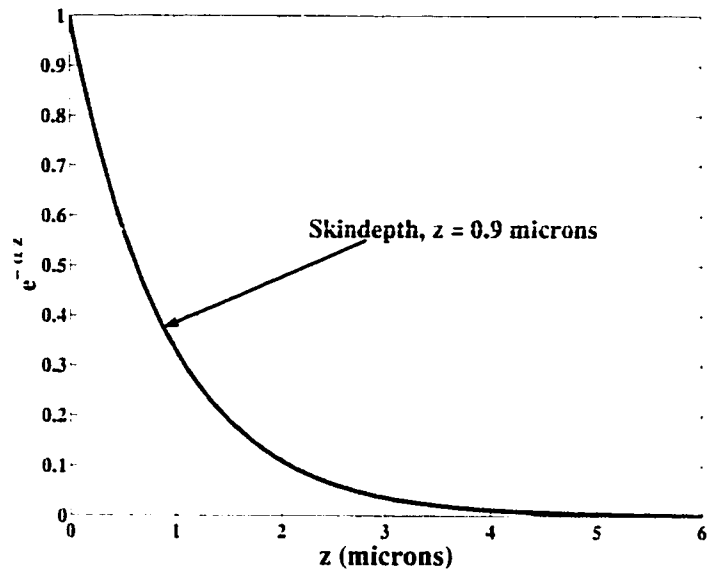

Figure 6.8: Exponential decay of the electric field within the PEC patch.

The temperature (T_∞) of the ambient air is assumed to be 20^oC, and the heat transfer coefficient, h, is assumed to be 5 $[\frac{W}{m^{2}.^oC}]$ [50].

Finally, the boundary condition on S_3 can be found by looking at the boundary condition between two solids (PEC wall and ferrite substrate), namely [50]

Heat conduction = Heat transfer = Heat conduction

through solid 1 across the gap through solid 2

or

$$-k_1 \frac{\partial T_1}{\partial n}|_i = h_c(T_1 - T_2)_i = -k_2 \frac{\partial T_2}{\partial n}|_i \tag{6.10}$$

where the subscript i denotes evaluation at the boundary, and h_c is defined as the thermal conductance $[\frac{W}{m^{2}.^oC}]$. For the special case of perfect thermal contact [50], $h_c \rightarrow \infty$. For the simulations performed in this dissertation, h_c is assumed to be 10,000 $[\frac{W}{m^{2}.^oC}]$.

Aluminum Doped G-610 Ferrite Garnet Material Characteristics				
Saturation Magnetization $4\pi M_s$(G)	Dielectric Constant ϵ_r	Curie Temperature T (°C)	Thermal Conductivity k ($\frac{W}{m^oC}$)	
680 ± 5%	14.5 ± 5%	185	5.4 (T= 95°C)	4.2 (T= 95°C)

Table 6.3: Material characteristics for an aluminum doped ferrite garnet.

6.3.2 Simulations

Table 6.3 lists the material parameters for an aluminum doped ferrite garnet (Trans Tech G-610). The material characteristics for this ferrite were used because the temperature properties of the substrate in [55] were not specified. The ferrite antenna in [55] was modeled using a saturation magnetization of 650 G and a dielectric constant of 15. These values are well within the tolerance specifications displayed in Table 6.3. The values listed in Table 6.3 for the thermal conductivity (k) are at temperatures much greater than the assumed room temperature of 20°C. However, looking at the values for k it is apparent that the thermal conductivity varies little with changes in temperature. Thus, for modeling purposes the thermal conductivity can be assumed to be 5.4 [$\frac{W}{m^oC}$] with a neglibile effect on the solution for the cavity temperature distribution.

As mentioned previously in section 6.3.1 the electric field distribution on the surface of the antenna element must be calculated in order to determine the dissipated power (see Equation 6.8). Figures 6.9 and 6.10 show the surface fields (computed using the FE-BI method) of the modeled antenna for various current values of the input probe feed. After computing $\mathbf{E}$, the magnetic field can be calculated from (2.14) and the surface current density is then given by

$$\mathbf{J}_s = \mathbf{n} \times \mathbf{H}. \tag{6.11}$$

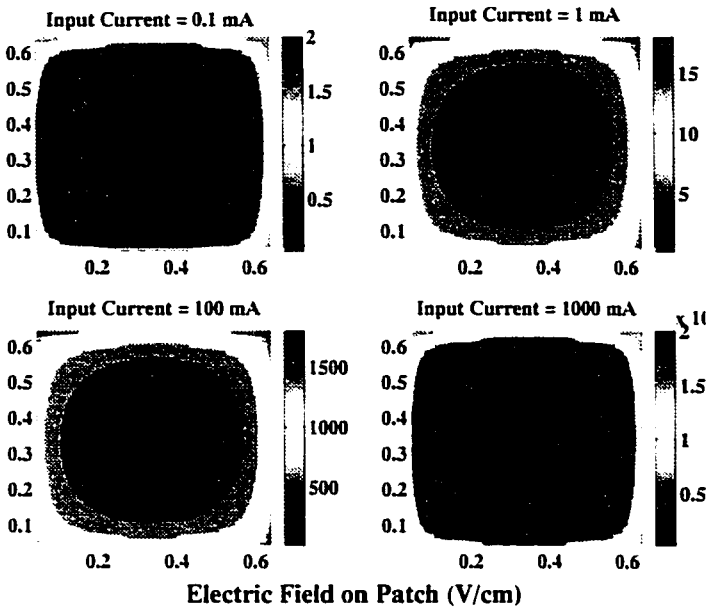

Figure 6.9: Microstrip patch antenna surface electric field distribution plotted for various input current excitation values (0.1 mA, 1 mA, 100 mA and 1 A).

$\mathbf{J}_s$ is then substituted into (6.8) to compute the dissipated power. The probe feed's contribution in (6.8) is neglected due to it's small size.

Figures 6.11 and 6.12 show the power density distribution computed from the surface electric fields (see Equation 6.8). These values were then used to find the temperature distribution within the ferrite substrate using the ANSYS FEM software (see section 6.3.1). The temperature distribution should only be affected for input current values above 0.5 A which is where the dissiapted power becomes significant (see Figure 6.13).

Figures 6.14 - 6.19 show the results of the temperature simulations for the various current probe excitations. For the input current values of 0.1 mA and 1 mA, the temperature gradient throughout the ferrite substrate is zero. Figures 6.14 and 6.15 show that the temperature distribution in the cavity remains unchanged which suggests that the antenna's resonant frequency does not change.

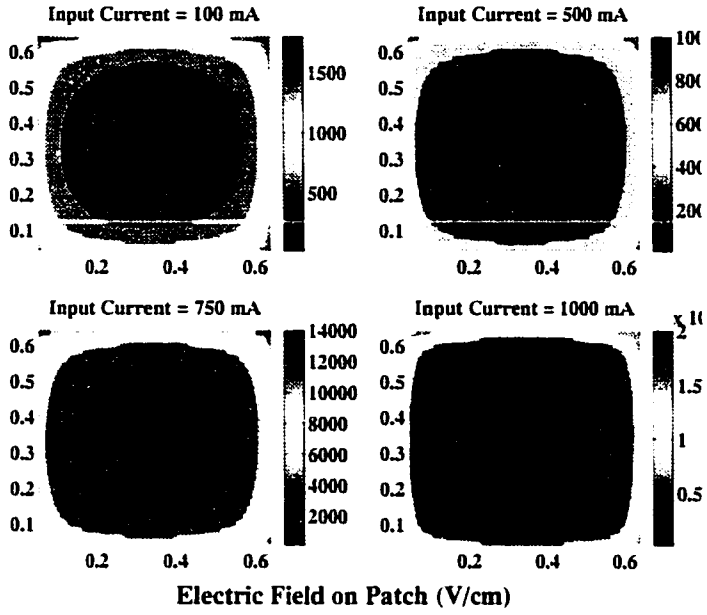

Figure 6.10: Microstrip patch antenna surface electric field distribution plotted for various input current excitation values (100 mA, 500 mA, 750 mA and 1 A).

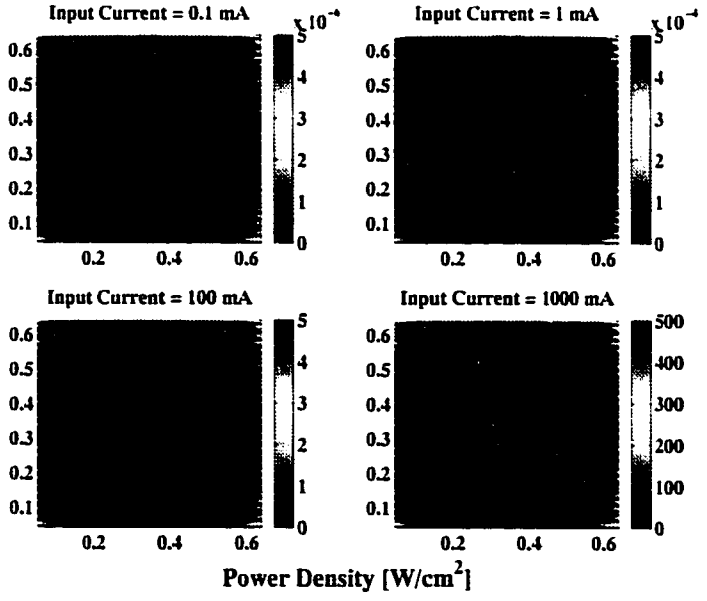

Figure 6.11: Power density generated from the conducting patch element for various input current excitation values (0.1 mA, 1 mA, 100 mA and 1 A).

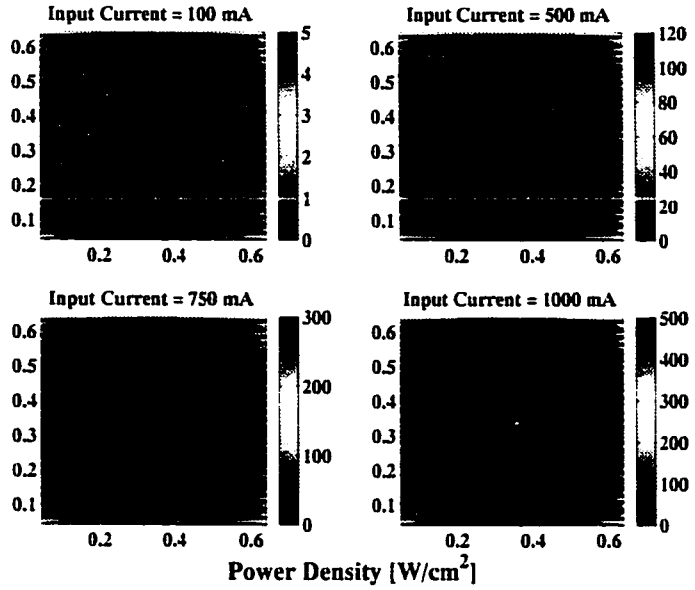

Figure 6.12: Power density generated from the conducting patch element for various input current excitation values (100 mA, 500 mA, 750 mA and 1 A).

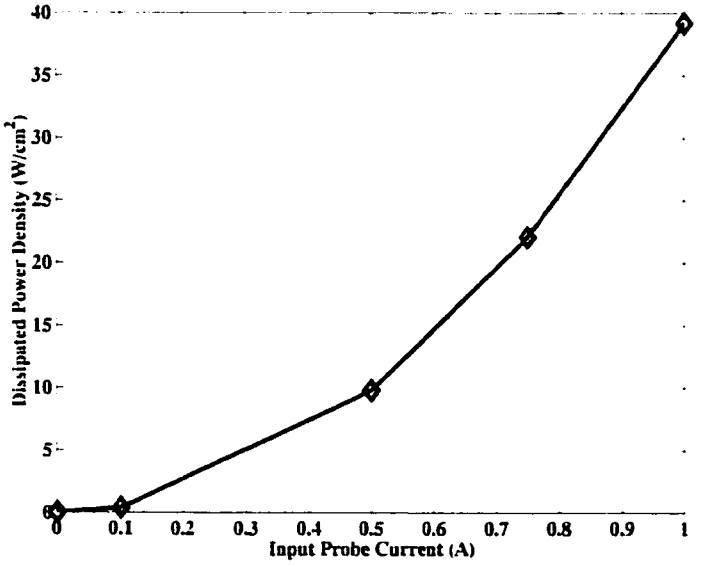

Figure 6.13: Average dissipated power density of the patch antenna as a function of the input probe current.

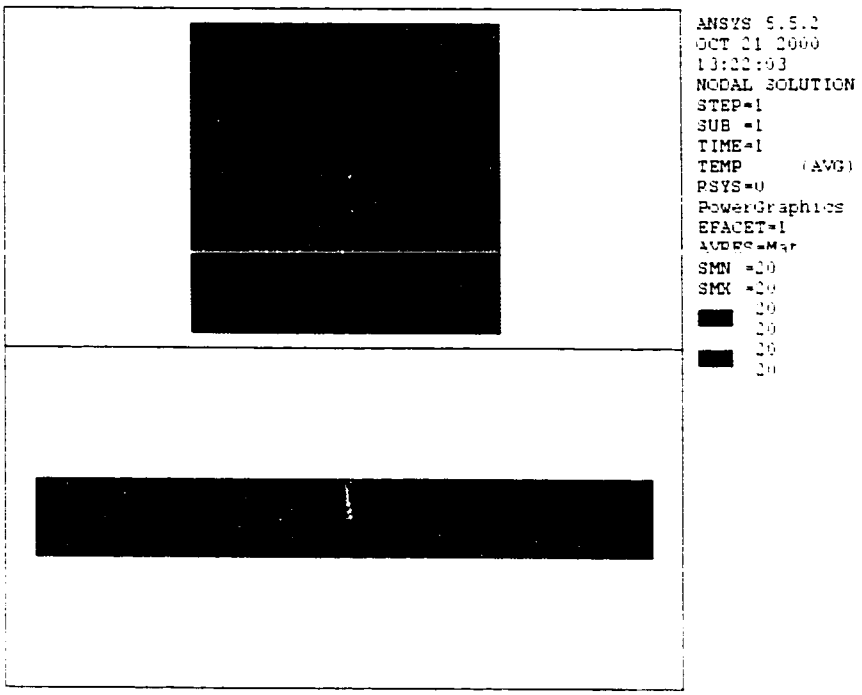

Figure 6.14: Temperature distribution of the ferrite substrate subjected to an input probe current of 0.1 mA.

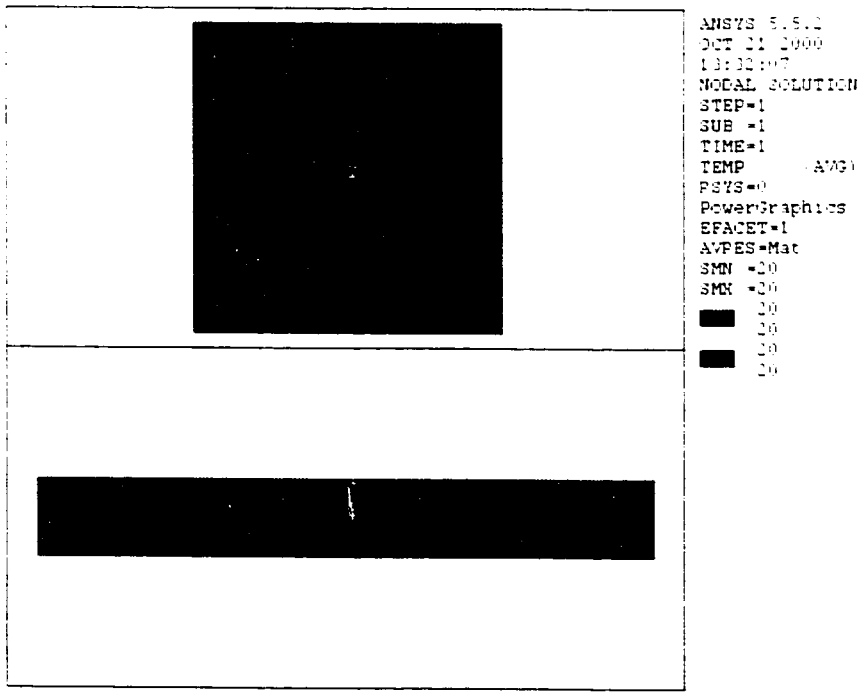

Figure 6.15: Temperature distribution of the ferrite substrate subjected to an input probe current of 1 mA.

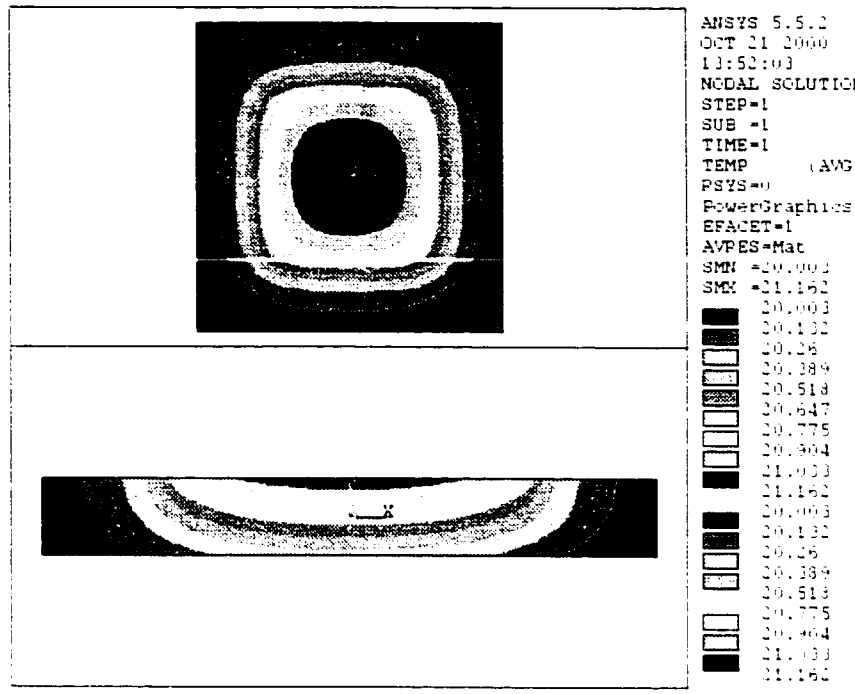

Figure 6.16: Temperature distribution of the ferrite substrate subjected to an input probe current of 100 mA.

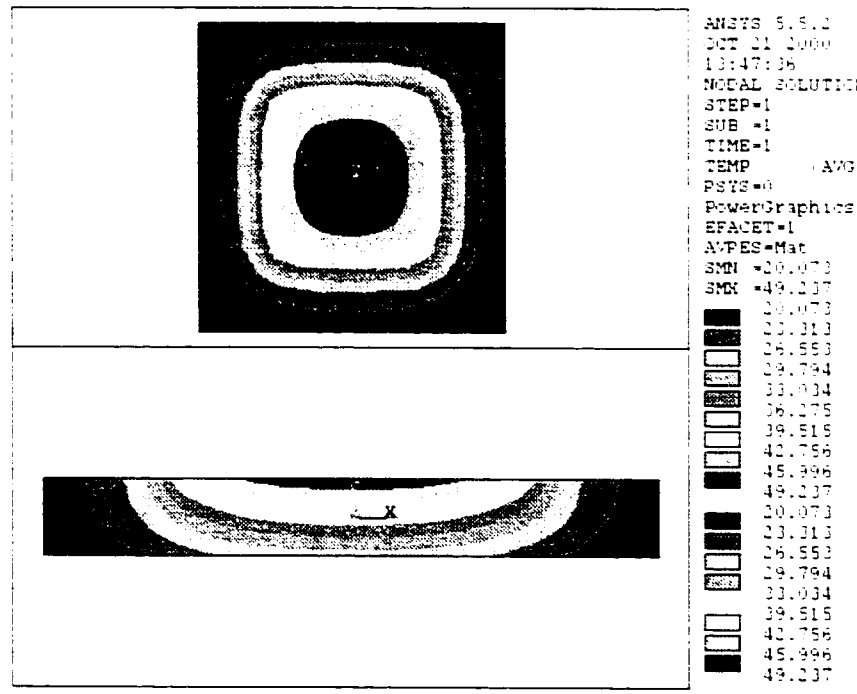

Figure 6.17: Temperature distribution of the ferrite substrate subjected to an input probe current of 500 mA.

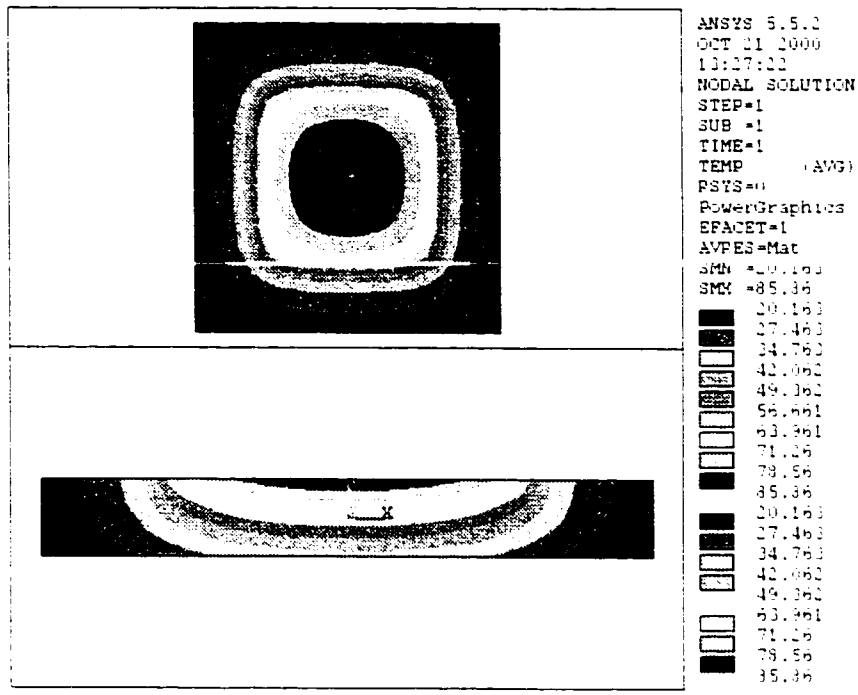

Figure 6.18: Temperature distribution of the ferrite substrate subjected to an input probe current of 750 mA.

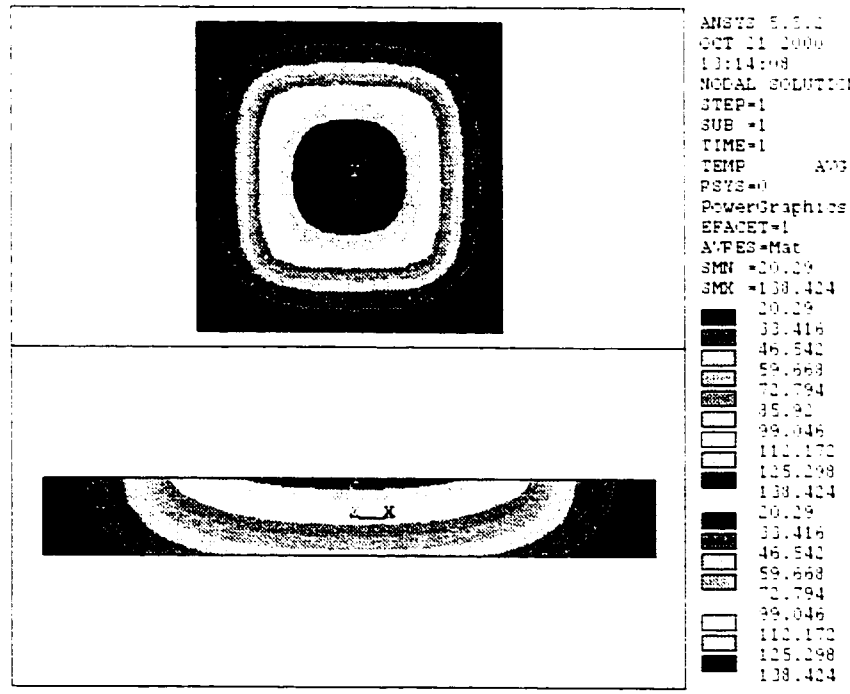

Figure 6.19: Temperature distribution of the ferrite substrate subjected to an input probe current of 1 A.

Increasing the input current to 100 mA produces a noticeable change in the temperature distribution shown in Figure 6.16. However, the temperature variation is extremely small. Figure 6.16 shows only a 1^o temperature increase from the initial temperature of 20^o C. Thus, the antenna's performance will still remain stable.

As the input probe current is increased from 0.5 A to 1 A, the temperature distribution of the ferrite substrate (see Figures 6.17 - 6.19) undergoes a noticeable change. The temperature underneath the patch increases which produces a nonuniform temperature distribution in the ferrite substrate. This temperature increase causes a change in the saturation magnetization since the saturation magnetization decreases with an increase in temperature (see Figure 6.1). This is disadvantageous because the antenna's resonant performance is seriously degraded, i.e. the nonuniform saturation magnetization will cause a change in the antenna's resonant frequency (see Figure 6.6).

6.4 Summary

In this chapter, the effect of temperature on ferrite antenna performance was analyzed. The microstrip patch in [56] was used in the simulation model. The surface electric fields on the patch element were computed to evaluate the power density within the ferrite substrate. The obtained power density was subsequently used in the ANSYS software package to solve for the temperature distribution within the ferrite substrate. It was shown that the dissipated power has an adverse effect on the ferrite substrate, causing it's temperature to increase. Specifically, the saturation magnetization is decreased and a nonuniform saturation magnetization distribution is observed. Thus, the resonant characteristics of the patch are also expected to change.

CHAPTER VII

CONCLUSION AND FUTURE WORK

7.1 Conclusion

In this dissertation, the FE-BI method was used to analyze microstrip patch antennas residing on ferromagnetic substrates. Preliminary validation results showed excellent agreement with MoM numerical simulations. Initially, both open cavities and a single microstrip patch were modeled. The numerical simulations demonstrate how ferromagnetic substrates improve bandwidth performance. Although these results were noteworthy, the current literature is replete with similar examples. The goal of the dissertation was to build upon these initial results and to delve into practical aspects involved with modeling ferromagnetic patch antennas. In addition, it was desired to extend the application of ferrites to microstrip array applications.

Convergence issues emerged using the FEM for ferrite antenna analysis. It was discovered that propagating modes within the ferrite substrates were linked to poor iterative solver convergence. The poor convergence was found to occur in frequency regions where the effective propagation constant was zero or near resonance. To overcome this difficulty, a more robust solver, utilizing the GMRES method, was

used for frequency points where this behavior occurred. This lead to well-behaved convergence simulation results.

After successfully overcoming convergence issues. associated with the FEM analysis of ferrite antennas, an experimental study was conducted on the effective propagation constant for microstrip structures. The purpose of this analysis was to verify the accuracy of the FEM for determining the propagation constant for ferrite substrates. This was necessary because a method was proposed for determining optimum bias field values for maximum beam steering using ferrite arrays. These bias field values are determined by the propagation constant.

MoM results for the propagation constant of an open-ended microstrip line were successfully validated using the FEM. Next. measurements were performed on a CPW TL with a ferrite substrate. The propagation constant was extracted from the S-parameters of the 2-port circuit and compared with numerical simulations. Poor results led to a static analysis of the actual magnetic field distribution internal to the ferrite substrate. The simulations conducted assumed a uniform bias field normal to the substrate. This proved to be an invalid assumption as the magnetic field was non-uniform and composed of components both normal and parallel to the ferrite substrate. The simulations were redone and this improved the comparison to the measurement data. This demonstrated the importance of considering the internal magnetic field distribution when modeling ferrite antennas.

Having established the FEM's capability to effectively model ferrite propagation constants. an example was considered to show the effects of ferromagnetic substrates on microstrip arrays. Using the ferrites as microstrip phase shifters. it was theoretically shown that the beam steering for arrays could be controlled by simply changing the applied bias field. This theoretical model highlighted a method proposed to determine optimum bias field values for maximum beam steer. It was shown that bias field values should be selected which correspond to maximum propagation con-

stant values. Theoretically, beam angles greater than 20 degrees were shown to be achievable.

Finally, temperature effects were considered in the modeling of ferrite microstrip antennas. A temperature study was conducted because the saturation magnetization is sensitive to temperature. Currents generated on the radiating conductive antenna element result in dissipated power. This power produces a heat flux which affects the temperature distribution in the ferrite substrate underneath the antenna. If the increase in temperature is too large, the antenna's performance will obviously degrade because the saturation magnetization decreases with temperature and becomes non-uniform. A patch element residing on a ferrite substrate was used to demonstrate this concept. The computed temperature distribution within the cavity illustrates that temperature plays a significant role in the performance of ferrite antennas.

7.2 Future Work

The work presented in this dissertation focuses on the numerical aspects of modeling ferrite microstrip antennas. Although the numerical aspects are important, it would be more advantageous to couple the theoretical work with simultaneous experimental measurements. The current literature contains many examples, both theoretical and experimental, demonstrating the application of ferrites to microstrip antennas. However, much of the data presented has not been validated. Hence, there exist few real benchmarks to validate simulation work using other methods such as the FEM. In the author's estimation it would be invaluable to build several simple antennas to compare with measurement data. It would also be extremely useful to produce several examples displaying parameters such as RCS and input impedance, that can be used as references by the scientific community.

The work in Chapter 4 attempts to bridge the gap between measurement and

theory. The propagation constant comparison served to show the effects of a non-uniform bias field on the phase constant internal to the ferrite substrate. The error present in the final results was due largely to experimental errors. The application of the copper tape on the ferrite substrate was done by hand which introduced error in the slot widths of the CPW. In addition, the ferrite substrate dimensions were similar to those of the biasing magnets which produced an extremely large magnetic fringing field effect. For future work, it would be advantageous to reproduce the results by improving the quality of the CPW slot widths, and using larger magnets with a smaller ferrite sample. The metal ground planes and conducting plane could be fabricated using a deposition process, which would definitely prove more accurate than using copper tape. These improvements would ensure that the measurement set-up was very close to the actual simulations resulting in a more accurate comparison.

In Chapter 5, the use of ferrites as microstrip phase shifters for antenna arrays was demonstrated. The results showed that theoretically scan angles greater than 20^{o} could be achieved. A significant contribution to this area of research would be to fabricate this type of antenna and to compare the measurements to simulation data. This would be an excellent way to couple the theoretical modeling to a practical measurement application. Measuring the scan performance of such an antenna array, would provide a way to verify whether any corrections were needed for the numerical model.

Finally, the temperature study contained in this dissertation would also benefit from experimental measurements. Future work would consist of measuring the resonant frequency of a single patch element as a function of the input power. As the input power is increased, the saturation magnetization will decrease, which should produce a change in the resonant frequency. Measurement data showing the amount of variance in the resonant frequency would highlight how much the performance of the antenna is degraded. This type of study would also be useful for analyzing

the ferrite microstrip phase shifters examined in Chapter 5. If there is a significant change in temperature along the ferrite microstrip line, the saturation magnetization would be affected which in turn would change the effective propagation constant along the line.

APPENDIX

APPENDIX A

Anisotropic Formulation

In the FEM formulation, the relevant integrals to be computed in the volume domain are

$$\mathbf{E}_{ij}^{e} = \int\int\int_{V_e} \nabla \times \mathbf{N}_i \cdot (\bar{\bar{\mu}}_r^{-1} \cdot \nabla \times \mathbf{N}_j) dV_e \tag{A.1}$$

$$\mathbf{F}_{ij}^{e} = \int\int\int_{V_e} \mathbf{N}_i \cdot (\bar{\bar{\epsilon}}_r \cdot \mathbf{N}_j) dV_e \tag{A.2}$$

where

$$\bar{\bar{\mu}}_r^{-1} = \begin{pmatrix} \tilde{\mu}_{xx} & \tilde{\mu}_{xy} & \tilde{\mu}_{xz} \\ \tilde{\mu}_{yx} & \tilde{\mu}_{yy} & \tilde{\mu}_{yz} \\ \tilde{\mu}_{zx} & \tilde{\mu}_{zy} & \tilde{\mu}_{zz} \end{pmatrix}. \tag{A.3}$$

$$\bar{\bar{\epsilon}}_r = \begin{pmatrix} \epsilon_{xx} & \epsilon_{xy} & \epsilon_{xz} \\ \epsilon_{yx} & \epsilon_{yy} & \epsilon_{yz} \\ \epsilon_{zx} & \epsilon_{zy} & \epsilon_{zz} \end{pmatrix}. \tag{A.4}$$

$$\mathbf{E}^e = \begin{pmatrix} \mathbf{E}_{xx} & \mathbf{E}_{xy} & \mathbf{E}_{xz} \\ \mathbf{E}_{yx} & \mathbf{E}_{yy} & \mathbf{E}_{yz} \\ \mathbf{E}_{zx} & \mathbf{E}_{zy} & \mathbf{E}_{zz} \end{pmatrix}, \tag{A.5}$$

and

$$\mathbf{F}^e = \begin{pmatrix} \mathbf{F}_{xx} & \mathbf{F}_{xy} & \mathbf{F}_{xz} \\ \mathbf{F}_{yx} & \mathbf{F}_{yy} & \mathbf{F}_{yz} \\ \mathbf{F}_{zx} & \mathbf{F}_{zy} & \mathbf{F}_{zz} \end{pmatrix}. \tag{A.6}$$

The values for the brick element matrices, in a general anisotropic medium are

$$\mathbf{K}_1 = \begin{pmatrix} 2 & -2 & 1 & -1 \\ -2 & 2 & -1 & 1 \\ 1 & -1 & 2 & -2 \\ -1 & 1 & -2 & 2 \end{pmatrix} \tag{A.7}$$

$$\mathbf{K}_2 = \begin{pmatrix} 2 & 1 & -2 & -1 \\ 1 & 2 & -1 & -2 \\ -2 & -1 & 2 & 1 \\ -1 & -2 & 1 & 2 \end{pmatrix} \tag{A.8}$$

$$\mathbf{K}_3 = \begin{pmatrix} -1 & -1 & 1 & 1 \\ 1 & 1 & -1 & -1 \\ -1 & -1 & 1 & 1 \\ 1 & 1 & -1 & -1 \end{pmatrix} \tag{A.9}$$

$$\mathbf{K}_4 = \begin{pmatrix} 1 & -1 & 1 & -1 \\ -1 & 1 & -1 & 1 \\ 1 & -1 & 1 & -1 \\ -1 & 1 & -1 & 1 \end{pmatrix} \tag{A.10}$$

$$\mathbf{K}_5 = \begin{pmatrix} 2 & 1 & -2 & -1 \\ -2 & -1 & 2 & 1 \\ 1 & 2 & -1 & -2 \\ -1 & -2 & 1 & 2 \end{pmatrix} \tag{A.11}$$

$$\mathbf{K}_6 = \begin{pmatrix} 1 & 1 & -1 & -1 \\ 1 & 1 & -1 & -1 \\ -1 & -1 & 1 & 1 \\ -1 & -1 & 1 & 1 \end{pmatrix} \tag{A.12}$$

$$\mathbf{E}_{xx} = \frac{l_x l_z \tilde{\mu}_{zz}}{6l_y}\mathbf{K}_1 + \frac{l_x l_y \tilde{\mu}_{yy}}{6l_z}\mathbf{K}_2 + \frac{l_x \tilde{\mu}_{zy}}{4}\mathbf{K}_3 + \frac{l_x \tilde{\mu}_{yz}}{4}\mathbf{K}_3^T \tag{A.13}$$

$$\mathbf{E}_{yy} = \frac{l_x l_y \tilde{\mu}_{xx}}{6l_z}\mathbf{K}_1 + \frac{l_y l_z \tilde{\mu}_{zz}}{6l_x}\mathbf{K}_2 + \frac{l_y \tilde{\mu}_{xz}}{4}\mathbf{K}_3 + \frac{l_y \tilde{\mu}_{zx}}{4}\mathbf{K}_3^T \tag{A.14}$$

$$\mathbf{E}_{zz} = \frac{l_y l_z \tilde{\mu}_{yy}}{6l_x}\mathbf{K}_1 + \frac{l_x l_z \tilde{\mu}_{xx}}{6l_y}\mathbf{K}_2 + \frac{l_z \tilde{\mu}_{yx}}{4}\mathbf{K}_3 + \frac{l_z \tilde{\mu}_{xy}}{4}\mathbf{K}_3^T \tag{A.15}$$

$$\mathbf{E}_{xy} = \frac{-l_z \tilde{\mu}_{zz}}{6}\mathbf{K}_5 + \frac{l_x \tilde{\mu}_{zx}}{4}\mathbf{K}_4 + \frac{l_y \tilde{\mu}_{yz}}{4}\mathbf{K}_6 + \frac{l_x l_y \tilde{\mu}_{yx}}{4l_z}\mathbf{K}_3^T \tag{A.16}$$

$$\mathbf{E}_{xz} = \frac{-l_y \tilde{\mu}_{yy}}{6}\mathbf{K}_5^T + \frac{l_x l_z \tilde{\mu}_{zx}}{4l_y}\mathbf{K}_3 + \frac{l_z \tilde{\mu}_{zy}}{4}\mathbf{K}_4 + \frac{l_x \tilde{\mu}_{yx}}{4}\mathbf{K}_6 \tag{A.17}$$

$$\mathbf{E}_{yz} = \frac{-l_x \tilde{\mu}_{xx}}{6}\mathbf{K}_5 + \frac{l_y l_z \tilde{\mu}_{zy}}{4l_x}\mathbf{K}_3 + \frac{l_y \tilde{\mu}_{xy}}{4}\mathbf{K}_4 + \frac{l_z \tilde{\mu}_{zx}}{4}\mathbf{K}_6 \tag{A.18}$$

$$\mathbf{F}_{ij} = \frac{l_x l_y l_z \epsilon_{xy}}{36} \begin{pmatrix} 4 & 2 & 2 & 1 \\ 2 & 4 & 1 & 2 \\ 2 & 1 & 4 & 2 \\ 1 & 2 & 2 & 4 \end{pmatrix} ; i = j, i = x, y, z \tag{A.19}$$

$$\mathbf{L}_1 = \begin{pmatrix} 2 & 1 & 2 & 1 \\ 2 & 1 & 2 & 1 \\ 1 & 2 & 1 & 2 \\ 1 & 2 & 1 & 2 \end{pmatrix} \tag{A.20}$$

$$\mathbf{F}_{xy} = \frac{l_x l_y l_z \epsilon_{xy}}{24} \mathbf{L}_1 \tag{A.21}$$

$$\mathbf{F}_{yx} = \frac{l_x l_y l_z \epsilon_{yx}}{24} \mathbf{L}_1^T \tag{A.22}$$

$$\mathbf{F}_{xz} = \frac{l_x l_y l_z \epsilon_{xz}}{24} \mathbf{L}_1^T \tag{A.23}$$

$$\mathbf{F}_{zx} = \frac{l_x l_y l_z \epsilon_{zx}}{24} \mathbf{L}_1 \tag{A.24}$$

$$\mathbf{F}_{yz} = \frac{l_x l_y l_z \epsilon_{yz}}{24} \mathbf{L}_1 \tag{A.25}$$

$$\mathbf{F}_{zy} = \frac{l_x l_y l_z \epsilon_{zy}}{24} \mathbf{L}_1^T \tag{A.26}$$

BIBLIOGRAPHY

BIBLIOGRAPHY

[1] N. G. Alexópoulos, "Integrated-circuit structures on anisotropic substrates", *IEEE Transactions on Microwave Theory and Techniques*, vol. 33, pp. 847–881, 1985.

[2] K. Araki, T. Koyama, and Y. Naito, "Reflection problems in a ferrite stripline", *IEEE Transactions on Microwave Theory and Techniques*, vol. 24, pp. 491–498, 1976.

[3] I. Bady, "Temperature stability of ferrite substrates in microwave integrated circuits", *IEEE Transactions on Magnetics*, vol. 7, pp. 276–280, 1971.

[4] C. A. Balanis, *Advanced engineering electromagnetics*, John Wiley and Sons, U.S.A., 1989.

[5] J. Batchelor and R. Langley, "Beam scanning using microstrip line on biased ferrite", *Electronics Letters*, vol. 33, pp. 645, 1997.

[6] K. J. Binns, P. J. Lawrenson, and C. W. Trowbridge, *The analytical and numerical solution of electric and magnetic fields*, John Wiley and Sons, West Sussex, England, 1992.

[7] D. M. Bolle, "The edge guided mode on ferrite loaded stripline", *in MTT-S International Microwave Symposium Digest*, pp. 257–259, 1976.

[8] C. R. Boyd, Jr., "A dual-mode latching reciprocal ferrite phase shifter", *IEEE Transactions on Microwave Theory and Techniques*, vol. 18, pp. 1119–1124, 1970.

[9] F. Brailsford, *Physical principles of magnetism*, D. Van Nostrand Company L.T.D., Princeton, N.J. 1966.

[10] A. D. Brown, L. C. Kempel, and J. L. Volakis, "Design method for antenna arrays employing ferrite microstrip phase shifters", Submitted for publicaton.

[11] A. D. Brown, J. L. Volakis, L. C. Kempel, and Y. Botros, "Patch antennas on ferromagnetic substrates", *IEEE Transactions on Antennas and Propagation*, vol. 47, pp. 26–32, 1999.

[12] G. J. Buck, "Ferrite microstrip phase shifters with transverse and longitudinal magnetization", *IEEE Transactions on Microwave Theory and Techniques*, vol. 18, pp. 1170–1173, 1970.

[13] N. Buris, T. Funk, and R. Silverstein, "Dipole arrays printed on ferrite substrates", *IEEE Transactions on Antennas and Propagation*, vol. 41, pp. 165–175, 1993.

[14] K. J. Button, "Microwave ferrite devices: The first ten years", *IEEE Transactions on Microwave Theory and Techniques*, vol. 32, pp. 1088–1096, 1984.

[15] R. E. Collin, *Antennas and Radiowave propagation*, McGraw-Hill Book Company, U.S.A., 1985.

[16] R. W. Damon and J. R. Eshbach, "Magnetostatic modes of a ferromagnetic slab", *Journal of Applied Physics*, vol. 31, pp. 104s–105s, 1960.

[17] R. W. Damon and H. Van De Vaart, "Propagation of magnetostatic spin waves at microwave frequencies in a normally-magnetized disk", *Journal of Applied Physics*, vol. 36, pp. 3453–3459, 1965.

[18] N. Das and J. S. Chatterjee, "Quarterwave microstrip antenna on a ferrimgnetic substrate", *Electronics Letters*, vol. 1981, pp. 441–442, 17.

[19] N. Das and S. K. Chowdhury, "Microstrip rectangular resonators on ferrimagnetic substrates", *Electronics Letters*, vol. 16, pp. 817–818, 1980.

[20] N. Das and S. K. Chowdhury, "Rectangular microstrip antenna on a ferrite substrate", *IEEE Transactions on Antennas and Propagation*, vol. 30, pp. 499–502, 1982.

[21] El-B. El-Sharawy and C. J. Koza, "Dual-ferrite slot line for broadband, high-nonreciprocity phase shifters", *IEEE Transactions on Microwave Theory and Techniques*, vol. 39, pp. 2204–2210, 1991.

[22] C. E. Fay, "Ferrite switches in coaxial or strip transmission line", *IEEE Transactions on Microwave Theory and Techniques*, vol. 10, pp. 455–458, 1962.

[23] T. J. Gerson and J. S. Nadan, "Surface electromagnetic modes of a ferrite slab", *IEEE Transactions on Microwave Theory and Techniques*, vol. 22, pp. 757–763, 1974.

[24] K. C. Gupta, R. Garg, I. Bahl, and P. Bhartia, *Microstrip lines and slotlines*, Artech House, Inc., Norwood, MA, 1996.

[25] A. Henderson and J. R. James, "Magnetized microstrip antenna with pattern control", *Electronics Letters*, vol. 24, pp. 45–47, 1988.

[26] K. H. Hering, "A novel design of an x-band high-power ferrite phase shifter", *IEEE Transactions on Microwave Theory and Techniques*, vol. 20, pp. 284–286, 1972.

[27] M. E. Hines, "Ferrite phase shifters and multi-port circulators in microstrip and stripline", *in Proceedings of the IEEE, G-MTT International Microwave Symposium*, pp. 108–109, Washington, D.C., USA, 1971.

[28] M. E. Hines, "Reciprocal and nonreciprocal modes of propagation in ferrite stripline and microstrip devices", *IEEE Transactions on Microwave Theory and Techniques*, vol. 19, pp. 442–451, 1971.

[29] P. Holst and M. Lemke, "Ferrite substrates for microwave integrated systems", *IEEE Transactions on Magnetics*, vol. 5, pp. 478–480, 1969.

[30] W. E. Hord, "Design considerations for rotary-field ferrite phase shifters", *Microwave Journal*, vol. 31, pp. 105–115, 1988.

[31] W. E. Hord, F. J. Rosenbaum, and C. R. Boyd, Jr., "Theory of the suppressed-rotation reciprocal ferrite phase shifter", *IEEE Transactions on Microwave Theory and Techniques*, vol. 16, pp. 902–910, 1968.

[32] H. How, T. Fang, D. Guan, and C. Vittoria, "Magnetic steerable ferrite patch antenna array", *IEEE Transactions on Magnetics*, vol. 30, pp. 4551–4553, 1994.

[33] H. How, T. Fang, W. Liu, C. Vittoria, M. H. Champion, and H. Southall, "Antenna array of circular patches on ferrite substrate", *IEEE Transactions on Magnetics*, vol. 33, pp. 735–738, 1997.

[34] H. How, T. Fang, and C. Vittoria, "Intrinsic modes of radiation in ferrite patch antennas", *IEEE Transactions on Microwave Theory and Techniques*, vol. 42, pp. 988–994, 1994.

[35] H. How and C. Vittoria, "Radiation frequencies of ferrite patch antennas", *Electronics Letters*, vol. 28, pp. 1405–1406, 1992.

[36] H. How and C. Vittoria, "Radiation modes in circular patch antennas", *IEEE Transactions on Microwave Theory and Techniques*, vol. 42, pp. 1939–1944, 1994.

[37] I. Ikushima and M. Maeda, "A temperature-stabilized broad-band lumped-element circulator", *IEEE Transactions on Microwave Theory and Techniques*, vol. 22, pp. 1220–1225, 1974.

[38] W. J. Ince and E. Stern, "Nonreciprocal remanence phase shifters in rectangular waveguide", *IEEE Transactions on Microwave Theory and Techniques*, vol. 15, pp. 87–95, 1967.

[39] J. Jin and J. L. Volakis, "A hybrid finite element method for scattering and radiation by microstrip patch antennas and arrays residing in a cavity". *IEEE Transactions on Antennas and Propagation*, vol. 39, pp. 1598–1604, 1991.

[40] M. L. Kales, "Modes in wave guides containing ferrites". *Journal of Applied Physics*, vol. 24, pp. 604–608, 1953.

[41] D. M. Kokotoff, *Full wave analysis of a ferrite-tuned cavity-backed slot antenna*, PhD thesis, Arizona State University, 1995.

[42] B. Lee and F. J. Harackiewicz, "The RCS of a microstrip antenna on an in-plane biased ferrite substrate". *IEEE Transactions on Antennas and Propagation*, vol. 44, pp. 208–211, 1996.

[43] H. Maheri, M. Tsutsumi, and N. Kumagai, "Experimental studies of magntically scannable leaky-wave antennas having a corrugated ferrite slab/dielectric layer structure". *IEEE Transactions on Antennas and Propagation*, vol. 36, pp. 911 917, 1988.

[44] J. Mazur, P. Kutysz, and A. Ćwikla, "Coupled-mode analysis of ferrite microstrip lines". *IEEE Microwave Guided Wave Letters*, vol. 9, pp. 300 302, 1999.

[45] J. E. Mercereau and R. P. Feynman, "Physical conditions for ferromagnetic resonance". *Physical Review*, vol. 104, p. 6, 1956.

[46] R. K. Mishra, S. S. Pattnaik, and N. Das, "Tuning of microstrip antenna on ferrite substrate". *IEEE Transactions on Antennas and Propagation*, vol. 41, pp. 230–233, 1993.

[47] M. C. Mohr and S. Monaghan, "Circularly-polarized phase shifter for use in phased array antennas". *IEEE Transactions on Microwave Theory and Techniques*, vol. 14, pp. 672–683, 1966.

[48] Y. Naito and Y. Yamanaka, "New nonreciprocal devices in a coplanar waveguide". *in MTT-S International Microwave Symposium Digest*, pp. 235–237, 1980.

[49] N. Okamoto and S. Ikeda, "An experimental study of electronic scanning by an antenna loaded with a circular array of ferrite rods". *IEEE Transactions on Antennas and Propagation*, vol. 27, pp. 426–430, 1979.

[50] M. Necati Özişik, *Heat Conduction*, John Wiley & Sons, Inc., 1993.

[51] J. K. Parks, B. R. Savage, L. J. Lavedan, Jr., and J. Brown, Jr., "A miniaturized c-band digital latching phase shifter", *IEEE Transactions on Microwave Theory and Techniques*, vol. 14, pp. 688–694, 1966.

[52] A. C. Polycarpou and C. A. Balanis, "Scan performance optimization of phased arrays using magnetized ferrites", *in IEEE Antennas and Propagation Society International Symposium*, 1999.

[53] A. C. Polycarpou, M. R. Lyons, and C. A. Balanis, "Finite element analysis of mmic waveguide structures with anistoropic substrates", *IEEE Transactions on Microwave Theory and Techniques*, vol. 44, pp. 1650–1663, 1996.

[54] D. M. Pozar, "Radar cross-section of microstrip antenna on normally biased ferrite", *Electronics Letters*, vol. 24, pp. 1079–1080, 1989.

[55] D. M. Pozar, "Radar cross-section of microstrip antenna on normally biased ferrite substrate", *Electronics Letters*, vol. 25, pp. 1079–1080, 1989.

[56] D. M. Pozar, "Radiation and scattering characteristics of microstrip antennas on normally biased ferrite substrates", *IEEE Transactions on Antennas and Propagation*, vol. 9, pp. 1084–1092, 1992.

[57] D. M. Pozar, "RCS reduction for a microstrip antenna using a normally biased ferrrite substrate", *IEEE Microwave Guided Wave Letters*, vol. 2, pp. 196–198, 1992.

[58] D. M. Pozar, *Microwave engineering*, Addison Wesley Publishing Company, Reading, MA, 1996.

[59] D. M. Pozar and V. Sanchez, "Magnetic tuning of a microstrip antenna on a ferrite substrate", *Electronics Letters*, vol. 24, pp. 729–731, 1988.

[60] P. J. Rainville and F. J. Harackiewiz, "Magnetic tuning of a microstrip patch antenna fabricated on a ferrite film", *IEEE Microwave Guided Wave Letters*, vol. 2, pp. 483–485, 1992.

[61] G. P. Rodrigue, J. L. Allen, L. J. Lavedan, and D. R. Taft, "Operating dynamics and performance limitations of ferrite digital phase shifters", *IEEE Transactions on Microwave Theory and Techniques*, vol. 15, pp. 709–713, 1967.

[62] J. S. Roy, P. Vaudon, A. Reineix, F. Jecko, and B. Jecko, "Circularly polarized far fields of an axially magnetized circular ferrite microstrip antenna", *Microwave Optical Technical Letters*, vol. 5, pp. 228–230, 1992.

[63] R. Ruppin, "Electromagnetic modes of a ferromagnetic slab", *Journal of Applied Physics*, vol. 62, pp. 11–15, 1987.

[64] Y. Saad, *Iterative Methods for Sparse Linear Systems*, PWS Publishing Company, Boston, 1996.

[65] E. Schlömann, "Theoretical analysis of twin-slab phase shifters in rectangular waveguide", *IEEE Transactions on Microwave Theory and Techniques*, vol. 14, pp. 15–23, 1966.

[66] J. Schuster and R. Luebbers, Private communication, August 1996.

[67] R. A. Stern, R. W. Babbitt, and J. Borowick, "A mm-wave homogeneous ferrite phase scan antenna", *Microwave Journal*, vol. 30, pp. 101-108, 1992.

[68] Steven N. Stitzer, "Modeling a stripline ferrite phase shifter", *in Proceedings of the 1997 IEEE MTT-S International Microwave Symposium*, pp. 1117-1120, Denver, CO, USA, 1997.

[69] L. Sun, H. How, C. Vittoria, and M. Champion, "Steerable linear dipole antenna using ferrite phase shifters", *IEEE Transactions on Magnetics*, vol. 33, pp. 3436-3438, 1997.

[70] L. C. Thomas, *Fundamentals of heat transfer*, Prentice-Hall, Inc., Englewood Cliffs, NJ, 1980.

[71] K. K. Tsang and R. J. Langley, "Design of circular patch antennas on ferrite substrates", *IEEE Transactions on Antennas and Propagation*, vol. 145, pp. 49-55, 1998.

[72] F. T. Ulaby, *Fundamentals of applied electromagnetics*, Prentice-Hall, Inc., Upper Saddle River, NJ, 1999.

[73] H. Unz, "Propagation in arbitrarily magnetized ferrites between two conducting parallel planes", *IEEE Transactions on Microwave Theory and Techniques*, vol. 11, pp. 204-210, 1963.

[74] J. T. Vaughn, P. R. Cox, G. P. Rodrigue, and G. R. Harrison, "Ferrite phase shifters using stress-insensitive garnet materials", *IEEE Transactions on Microwave Theory and Techniques*, vol. 43, pp. 1017-1022, 1995.

[75] J. L. Volakis, T. Özdemir, and J. Gong, "Hybrid finite element methodologies for antennas and scattering", *IEEE Transactions on Antennas and Propagation*, vol. 45, pp. 493-507, 1994.

[76] L. R. Walker, "Magnetostatic modes in ferromagnetic resonance", *Physical Review*, vol. 105, pp. 390-399, 1957.

[77] L. R. Walker, "Ferromagnetic resonance: Line structures", *Journal of Applied Physics*, vol. 29, pp. 318-323, 1958.

[78] T. F. Wall, *Applied magnetism*, Ernest Benn Limited, London, England, 1927.

[79] L. R. Whicker and C. R. Boyd, Jr., "New reciprocal phaser for use at millimeter wavelengths", *IEEE Transactions on Microwave Theory and Techniques*, vol. 19, pp. 944-945, 1971.

[80] H. Yang. "Microstrip open-end discontinuity on a nonreciprocal ferrite substrate", *IEEE Transactions on Microwave Theory and Techniques*, vol. 42, pp. 2423–2428, 1994.

[81] H. Yang, "A note on the mode characteristics of a ferrite slab", *IEEE Transactions on Microwave Theory and Techniques*, vol. 43, pp. 235–238, 1995.

[82] H. Yang, "Characteristics of switchable ferrite microstrip antennas", *IEEE Transactions on Antennas and Propagation*, vol. 44, pp. 1127–1132, 1996.

[83] H. Yang and J. A. Castaneda, "Infinite phased arrays of microstrip antennas on generalized anisotropic substrates", *Electromagnetics*, vol. 11, pp. 107–124, 1991.

[84] H. Yang and J. A. Castaneda, "Multifunctional and low RCS nonreciprocal microstrip antennas", *Electromagnetics*, vol. 12, pp. 17–31, 1992.

[85] H. Yang, J. A. Castaneda, and N. G. Alexópoulos, "Surface wave modes of printed circuits on ferrite substrates", *IEEE Transactions on Microwave Theory and Techniques*, vol. 40, pp. 613–621, 1992.

[86] H. Yang, J.A. Castaneda, and N.G. Alexopoulos, "The RCS of a microstrip patch on an arbitrarily biased ferrite substrate", *IEEE Transactions on Antennas and Propagation*, vol. 41, pp. 1610–1614, 1993.

[87] X. Yansheng, "Theory and design of high average power, fast switching microwave ferrite phase shifters", *Microwave Journal*, vol. 28, pp. 203–206, 1985.